QATAR UNIVERSITY

COLLEGE OF ENGINEERING

TURBULENCE MODELING AND VALIDATION TO PREDICT VELOCITY PROFILES IN CLOSE-COUPLED FIVE-GORE ELBOWS

BY

MOHAMMED KARBON

A Dissertation Submitted to

the College of Engineering

in Partial Fulfillment of the Requirements for the Degree of

Doctorate of Philosophy in Mechanical Engineering

January 2021

COMMITTEE PAGE

The members of the Committee approve the Dissertation of
Mohammed Karbon defended on Tuesday, 01/12/2020.

Prof. Ahmad Sleiti
Thesis/Dissertation Supervisor

Prof. Faris Tarlochan
Committee Member

Prof. Samer Ahmed
Committee Member

Prof. Mohamed Al-Khawaja
Committee Member

Prof. Riyadh Al-Raoush
Committee Member

Approved:

Khalid Kamal Naji, Dean, College of Engineering

ABSTRACT

KARBON, MOHAMMED, A, Doctorate : January : 2021, Doctorate of Philosophy in Mechanical Engineering

Title: Turbuelence Modeling and Valication to Predict Velocity Profiles in Close-Coupled Five-Gore Elbows

Supervisor of Dissertation: Prof. Ahmad K Sleiti.

This research work aims to validate advanced turbulence modeling techniques used to predict complex flows in close-coupled five-gore elbows and similar complex geometries using data from 2016 ASHRAE RP-1682 (Study to Identify CFD Models for Use in Determining HVAC Duct Fitting Loss Coefficients). The study in question conducted experimental measurements of friction factor, pressure loss coefficient, and detailed velocity profiles in two close-coupled five-gore elbows.

Using this data, this research will test the validity of specific CFD models in the case of turbulent flow in a Z-shape duct. The models, namely Reynolds Stress Model, Large Eddy Simulation, ζ-f Model and Wall-Modeled Large Eddy Simulation (WMLES) are analyzed, validated and compared using experimental data from ASHRAE RP-1682 [1], [2] and [3]. The effect of separation distance (L_{int}/D) is also investigated; to assess and identify the capabilities and limitations of each turbulence model in predicting such complex flow; and to probe the influence of the numerical grid size and quality on the accuracy of the CFD predictions. The study is comprehensively discussing the framework of the current LES model with an eddy viscosity subgrid-scale model.

The dissertation focused on the issues encountered by RSM in properly capturing flow behavior dominated by flow separations. The LES simulation has shown some limitations in the flow separation and re-attachment regions. This dissertation

finds that the turbulent kinetic energy production in ζ equation of ζ-f model is reproduced much more easily and accurately than with other models. Mean velocity gradient as well as local turbulent stress terms are also much easier to resolve properly. The ζ-f model was found to be both more efficient in terms of computational power and better able to predict the mean flow velocity profile results than the RSM model, despite both models being coupled steady-state RANS models. ζ-f model also performed better in the numerical resolution of flow separation and re-attachment regions compared to the RSM model. WMLES model is employed to investigate the SGS model impact on the small eddies dissipated from the large eddies. Moreover, WMLES model produces much better results than the LES model with much less computational time, however the SGS viscosity give further undesired damping effect to the flow energy.

DEDICATION

I dedicate my dissertation work to my family. A special feeling of gratitude to my loving parents, to my wife and our kids, Shaikha and Abdulla.

ACKNOWLEDGMENTS

I would like to thank my supervisor. Without his encouragement, patience, care, and advice, I would not have completed this thesis. Other members of the PhD thesis committee have given their time and knowledge to improve the thesis. I thank them for their comments and support. I must acknowledge my wife and kids. Without their support I would not complete my thesis.

TABLE OF CONTENTS

LIST OF TABLES

LIST OF FIGURES

LIST OF NOMENCLATURE

Symbols

C_P	Specific heat capacity [J/kg ·K]
C	Constant in the k−ε turbulence model
L	Characteristic length [m]
K	Turbulent kinetic energy [J/kg · s]
D	Pipe diameter [inch]
f_f	Friction coefficient
m	Mass [kg]
P	Pressure [Pa]
P_r	Prandtl number Pr = μcp/λ
t	Time [s]
u^τ	Friction velocity [m/s]
u^+	Non-dimensional velocity distribution
$\bar{v}_i'$	Components of Fluctuating velocity [m/s]
$\bar{v}_i$	Components of Mean velocity [m/s]
x_i	Coordinate in i direction [m]
y	Wall distance [m]
y^+	Non-dimensional wall distance
z	Axial coordinate [m]
ℓ_m	Mixing length of the gas
V_m	Molecular velocity

V_t	Turbulence velocity scale
N, S, E , W, SW, SE, NW, NE	Main and surrounding grid point locations
Str	Strouhal number
U, u, U1	u-velocity component
V, v, V1	v-velocity component
Z, z, Z1	z-velocity component
R_e	Reynolds Number
D_e	Dean Number

Greek symbols

ρ	Fluid density [kg/m^3]
ε	Dissipation rate of Turbulent Kinetic Energy [J/(kg.s)]
μ	Dynamic Viscosity [Pa-s]
v	Kinematic Viscosity [m2/s]
ζ-f	Zeta-f
τ	Stress tensor [N]
σ^2	Variance [s]
κ	Constant in wall law
τ_w	Normal stress at the wall [N]

Subscripts

ij, k	Cartesian tensor notation components where i, j, k= 1,2,3
f	Fluid
g	Gas/gravity [m/s^2]
in	Inlet
k	Kinetic energy [Joule]
n	Normal
out	Outlet
r	Radial
S	Surface
T	Turbulent
W	Wall

Abbreviations

ASM	Algebraic stress model
CFD	Computational fluid dynamics
DNS	Direct numerical simulation
EASM	Explicit algebraic stress model
LDV	Laser Doppler velocimetry
LES	Large eddy simulation
LISF	Laser Inter-ferrometer skin friction
MLH	Mixing length hypothesis
NLEVM	Nonlinear eddy viscosity turbulence model

PSL	Parabolic sub-layer
RANS	Reynolds-averaged Navier-Stokes
RNG	Renormalization group
RSM/RSTM	Reynolds stress transport model
SST	Shear stress transport
WMLES	Wall-modeled large-eddy simulation

CHAPTER 1: INTRODUCTION

1.1 Background

Since 1988 experimental work such as ASHRAE: RP-551 [4], RP-690 [5], RP-1319 [6], RP-1488 [6], RP-1606 [7] contributed to the creation of the duct fitting database [8]. The research in the database is freely available to the public. Until RP-1493 [9] was published, Direct Numerical Simulations (DNS) to predict duct flow, as compared to empirical tests, were not as studied in the literature. RP-1493 focused on validating Computational Fluid Dynamics (CFD) and its ability to estimate pressure loss coefficients. Direct numerical methods promised to cut costs of instruments and equipment setups essential for experimental pressure loss coefficient measurements. Unfortunately, RP-1493 found that numerical results predictions at that time failed to achieve 15% accuracy. There are few studies that showed similar results, including A. K. Sleiti et al. [10], Liu et al. [11], Manning et al. [12], and Gutovic et al. [13].

The review of the literature published by well-known researchers around the world reveals that there are limited number of papers that study flow turbulence in Z-shaped duct flows. Moreover, the studies available to the public are inadequate in their treatment of turbulent or transient flow in Z-shaped ducts. In [1], [3], Salehi et al. investigated the turbulent flow in different duct shapes (e.g., Z and U) and presented numerical and experimental results for both ducts. Their research concluded that turbulence modeling approaches used to estimate the accuracy of the turbulence flow showed inconsistent or incorrect trends. A. K. Sleiti et al. published another paper on the Z-shaped duct [2]. They contrasted the computed profiles of velocity to LES and RSM anticipation when it comes to the investigation of separation distance impact. RSM modeling anticipated the velocity tendencies precisely (under 15% error). Large-

eddy simulation was not able to anticipate the velocity tendency and magnitude.

The challenge and opportunity of correctly predicting the Z-shaped duct remain open, and therefore, this thesis is to document and report how to address this issue with the state-of-the-art CFD methodology.

Rutten et al. [14] analyzed turbulent flows numerically in a couple of 90° bends with 2 and 3 as their ratios of curvature, employing large-eddy simulation. Djebedjian et al. [15] investigated 2D and 3D U-bend ducts with mild and strong curvatures using Realizable k-ε (RKE), standard k-ε, shear-stress transport (SST) k-ω, and renormalization group (RNG) k-ε, along with RSM. These studies determined that, all models except the standard k-ε model over-predicted the reattachment. The results obtained using the RSM and the RNG k-ε models were satisfactory at the recirculation regions. However, the computational time they required was on the higher side. Several scientists employed LES, RANS, and DNS models to scrutinize the flow features in ducts with curvature in their shapes. However, less attention has been given to the studies related to Z-shaped ducts at varying separation distances.

Turbulent flow existing in Z-shaped ducts is complex which means it requires comprehensive scrutiny and investigation. Experimental research [1] revealed that the flow in Z-shaped ducts has a strong separation distance function, which means that further is required in order to better understand the complex behavior of turbulence. This dissertation examines turbulence modeling in Z-shaped ducts using wall-modeled large-Eddy simulation (WMLES), RSM, LES, and ζ-f model.

The importance of ducts for large sectors of engineering and technology cannot be overstated. Ducts are crucial elements of contamination control systems, gas cleaning processes, air ventilation systems and aerosol sampling and filtration. Ducts are an integral part of heating, ventilation, air conditioning and in transportation of

water, gases, and oils. In the recent decade, the study of ducts has become the center of research in the design of the aircraft engine, to make it more efficient and with fewer emissions. The understanding of ducts provides an opportunity to make solar energy more efficient.

In these industries, the sound understanding of ducts, the laminar and turbulent flow which they produce, as well as of particle deposition is crucial for obtaining results. That is why some of the ducts which find the most common industrial use, such as the S-shaped, Z shaped, V-ribbed triangular-shaped, horizontal and vertical ducts are extensively studied in the recent literature [16]. Computational fluid dynamics (CFD) is vital instrument in the study and the design of efficient duct applications. It can be used in simulations of particle distribution in horizontal duct flow [17], to analyze the impact of gas-particle flows [18] and in the design of S-shaped ducts [19]. These operations enable the production of more efficient duct applications, which enable greater productivity and efficiency of the entire system.

In the recent decade, extensive research has been made by scientists to design effective aircraft systems for maximum efficiency and fewer emissions. Some researchers proposed to split the entire engine into smaller parts and then redesign each part independently [20]. However, the drawback of that approach was the risk of sub-optimal design when different parts are designed in isolation [20]. Hence, the design of the intermediate compressor duct system became the center of study. Cited as its advantage is the relatively bulk fluid flow over large radial offset in small spacing without the separation of the [21]. There have been very few studies that reported on the applications of S-shaped ducts in the behavior of various kind of fluids. Britchford et al [22] performed several experiments via CFD calculations on clean annular flow in S-shaped ducts. The main goal of their research was the study of flow physics and

behavior. As an inlet boundary condition, they applied a precisely developed duct flow system for the said type of duct. Bailey et al [23] proposed that the pressure gradient that develops at inner duct casing can be lowered if realistic inlet boundary conditions are used in the design the boundary layer. Hence, the risk of separation is decreased which allows a shorter duct.

A study on S-shaped compressor transition duct design presented an optimization method which involved using uniform design of the duct in combination with response surface methodology as well as a genetic algorithm [24]. This approach demonstrated that this optimization can be used in the design of turbofan engines. The simulation and designing of S-shaped duct diffuser for aircraft with the help ANSYS fluent simulation software, a key resource in CFD [25]. The paper studied baseline clean duct configuration and the aerodynamic interface plane (AIP). The results showed that the installation of AIP rake legs installed inside the S-duct has a very slight effect on the airflow and thus, the performance of the duct was enhanced. The C-ducts are also widely used in the aircraft industry. In combustors, ventilation ducts and wind tunnels and in the internal cooling systems of gas turbines. The flow through the straight ducts is relatively easy and there is less pressure drop as compared to the flow-through curved and bend ducts [26].

The duct and piping systems with many cutting and wide-angled shapes are used in HVAC systems, installed heat exchangers and in the transportation of water, gases, and oils.

The Z-shaped ducts are a vital part of nearly every air-conditioning and ventilation system. However, the literature on turbulent flow in the Z-shaped ducts is relatively scarce. The studies which examined it as well as those which examined turbulent flow in U-shaped ducts, both experimentally and numerically, showed that

the RSM models were best to calculate the fluid flows and pressure loses at the elbows and bends.

Multiple researchers conducted studies on both static and dynamic flow in duct geometries with various bens, curvatures, angles. A study explored the flow of turbulent and laminar at 90 degrees bend and a 3.7 ratio of curvature using the experimental method [27]. The effects of curvature ratio were studied by [28] where experimental analysis was conducted on water flow in elbows at different curvature ratios. The experiment suggested that as the curvature ratio increased, the boundary layer separation was observed [29]. CFD was also used in the optimization of annular S-shaped ducts by identifying design factors which contribute to optimal performance [30]. The study revealed that single-objective optimization for exit flow uniformity and energy loss minimization is not possible, so a multi-objective solution was presented. The final design was able to reduce the pressure drop by 15.6% and radial exit velocity to 34.2% when compared with baseline design. Another study optimized S-shaped ducts using computational design [31]. A free-form-deformation technique was used to manage the geometry of the ducts, while a steady state CFD simulation was used to analyze the flow. The result was a 14% drop in pressure and an improvement in flow smoothness by 71%, a significant improvement compared to conventional techniques.

1.2 Problem Statement

The research on turbulent flow through curved ducts still leaves many questions to be answered, particularly in non-conventional duct shapes such as the Z shape. The physics of the phenomena in question are not yet clearly understood. To understand the turbulence behavior systematically, significant research work is required. A comprehensive study on turbulent flow in non-conventional ducts could greatly

enhance the available knowledge of this important field of study. Rigorous validation of numerical simulation methods is crucial for their improvement and, in time, wider application in industry. The cost-saving potential of valid simulations is tremendous. To that end, a wide range of design parameters need to be studied. This thesis addresses these problems. This research will study and compare how different numerical models predict the various turbulence flows in Z-shaped ducts. Below are some of the main problems found and reported in a literature review for the following turbulence models:

- Reynolds stress model: The model is based on steady-state RANS relations, which assumes steady-state turbulent flow [32] and minimum temporal effect. The performance of the RSM model is adequate within the boundary layer. However, it shows excessive diffusion in separated regions [33].
- Large-eddy simulation (LES) and wall-modeled LES models: These models experience robustness issues in predicting flow separation in the reattachment regions [32].
- ζ-f model: This model requires a UDF code integration for the applied geometry, which is not an easy task to do if the proposed research work has more than one geometry to be analyzed.

1.3 Methodology

In this dissertation, turbulence modelling issues related to Z-shaped ducts are studied and analyzed using RSM, LES, ζ-f model, and WMLES. It is widely recognized that the exactness of results obtained by direct numerical simulation for turbulent flow via curved ducts rests on the accurate estimation of characteristic transition of boundary-layer. In the RSM, the turbulence redistribution is modeled closer to the boundary wall by considering more flow physics, which is also important during the

transition process.

Conversely, for computing the flow field, the numerical stability along with robustness of ζ-f models is better than the classical turbulence model. The novel eddy-viscosity model is formulated by making changes in the elliptical relaxation method to solve the equation of steady-state transport. In the standard $k-\varepsilon$ model, turbulent kinetic energy k is implemented, whereas in ζ-f models velocity scales ratio, zeta (ζ)) is used to assess eddy viscosity. ζ is defined by $\overline{v^2}/k$ where $\overline{v^2}$ represents the "wall-normal" velocity scale. The f term in ζ-f models represent an elliptic function, generally solved by the elliptic equation. It is used to parameterize an effect on boundary layer walls, named anisotropic wall effects. $\overline{v^2}$ also denotes the velocity variation common to the streamlines. The novel concept was introduced to better utilize the scaling for appropriate representation of turbulent transports' damping characteristics.

1.4 Thesis Scope

The principal objective of the present study is to perform qualitative and quantitative comparison of different turbulence models to identify the model best suited for Z-shaped duct flow patterns. This thesis includes studying and analyzing a detailed velocity profile predicted from several turbulence models and subsequently validated with the use of available experimental data. The code development involved in setting up the methodology of performing the simulation is documented and presented in this thesis. The thesis scope also includes a detailed methodology presentation on how to construct a suitable mesh for the Z-shaped duct application and identify numerical schemes for implementation.

1.5 Novelty and Contributions of the Research

The current thesis aims at researching the turbulence modeling methods for predicting the airflow pattern of the Z-shaped ducting application. The current state of knowledge of implementing a turbulence model to capture wall-bounded flow physics such as ducting application is not well established and mostly fails to achieve satisfactory accuracy. The author will conduct a series of turbulence models, namely RSM, LES, ζ-f, and WMLES models, to address the difference in accuracy and computing efficiency. The results documented here will lay important support to the current knowledge and expand research in this area.

The present thesis offers a detailed analysis and validation of the numerical approach in the Z-shaped duct airflow pattern assessment. The motivation for carrying out such a study is well summarized by A. K. Sleiti et al. [10]. In particular, the current two-equation and LES models do not sufficiently address the accuracy of the Z-shaped duct. This thesis discusses in detail and lays out the best-practice LES setup to improve accuracy prediction and explore other alternatives focused on the Z-shaped duct. This thesis contributes to the following:

1. Mesh requirement for modeling Z-shaped duct
2. Implementation of the Reynolds stress model (RSM) and its numerical schemes to the Z-shaped duct
3. Implementation of large-eddy simulation (LES) and corresponding numerical schemes to the Z-shaped duct
4. Development of custom user-defined function (UDF) script for ζ-f turbulence model to the Z-shaped duct
5. Implementation of wall-modeled large-eddy simulation (WMLES) to the Z-shaped duct

CHAPTER 2: LITERATURE REVIEW

As industrial applications for the duct and pipe systems are manifold, studies on laminar flow are abundant in the existing literature. However, less-attention is given to the more complex turbulent flow, as well as to non-conventional duct shapes such as the Z shape.

The methods employed by researchers for determining the pressure loss coefficient include various two-equation methods and the Reynolds stress model. The two-equation methods include the standard $k-\omega$, $k-\varepsilon$, RNG $k-\varepsilon$, realizable $k-\varepsilon$, and SST $k-\omega$ models [34], [35]. Several studies conclude that trends predicted by two-equation models are consistently inaccurate, whereas RSM, when used with enhanced wall treatment, predicted the loss coefficients of elbow correctly, with error below 15%.

The literature studies various duct geometries with curvatures. Weske [36] examined the distribution of velocity at the openings of elbow ducts of various cross-sectional shapes used in aircraft. These ducts were round, square, elliptical, and rectangular, with Reynolds number ranging from 0.2 to 0.6×10^6. His research found that if the ratio of bend curvature radius to pipe diameter is lesser than 1.5, local flow separation happens downstream the pipe bend, and flow becomes unsteady. Al-Rafai et al. [37] also conducted a laser Doppler anemometry (LDA) experiment and simulation to study the contribution of the curvature ratio on airflow turbulence in a circular pipe at Reynolds number of 34,000. The numerical modeling was performed using commercial software PHOENICS. They simulated two bend versions through the standard k-ε model. The data leads to a conclusion that with the smaller bend version, the secondary flow appears closer to the bend-pipe wall, with radial orientation of the

bend curvature. Such secondary flow is also more prevalent. Their numerical results correlate to the experiment and show that the secondary flow consists of two counter-rotating vortices. It is believed that this happens because of the imbalance present between the gradient of pressure and the centrifugal force closer to the 90° bend curvature location.

Several studies have investigated the 90° bend duct with different curvature ratios. In [38], Taylor et al. conducted an experiment to investigate the laminar and turbulent in the 90° bend duct. The values of boundary layers at the inlet have showed higher values of secondary velocity. While comparing the model with fully developed inlet flow, they found that, for complete flow development, the boundary layer thickness is important. Sudo et al. [39]–[41] worked on square-sectioned 90° bend ducts with curvature ratios of 3.7 and 4. The results on both velocities (i.e., mean and fluctuating), along with Re stresses in the pipe cross-section, were obtained by revolving a probe using the hot-wire technique. The results showed that the primary and secondary velocity flowed along the Re stress distributions. The results showed that due to small curvature ratio values, boundary layer separation was not present at the bend. To understand the significance of the curvature ratio for boundary layer separation, Ono et al. [42] examined the flow of water through two elbows with ratios of curvature (δ) of 2 and 3, respectively. The elbows in question were of different length, with Reynolds number (Re) of 1.8×10^5 and 5.4×10^5, respectively. Moreover, PIV (fast particle image velocimetry) was employed to determine the field velocity. Similarly, Tan et al. [43] conducted an independent experiment with a different curvature ratio. In their study, a novel four-vortex structure was used. The results showed that increasing curvature ratio results in boundary layer separation. Tunstall and Harvey [44] discovered a secondary flow pattern different from the

classical twin vortex pattern at Reynolds number of $4x10^4$. The secondary flow pattern was dominant, and the circulation axis was either in clockwise or anti-clockwise orientation. The new flow pattern was unsteady, and it changed directions at low-frequency time scales. The method is explained with turbulent flow produced in the upstream flow and the asymmetry of the inner wall separation. In [45], [46], Hellstrom et al. studied the behavior of a flow field within an elbow. The curvature ratio was kept at $\delta=2$ and the Reynolds number between 2×10^4 and $1.15x10^5$. The researchers used the POD (proper orthogonal decomposition) method to analyze the data and observed that the highly energetic structure of flow was a swirl switching structure instead of well-known Dean motion. The swirl switching structure was a bimodal cell with a random direction of rotation.

Tanaka [54] worked to develop a comprehensive understanding of vibration and pressure drop in bend pipes. The work involved a numerical study of pipes with elbows of different curvature radii and diameters as well as pipes of two different lengths. These elbow pipe structures were numerically studied at different turbulent flow conditions based on different Reynolds numbers. Simulations showed that the turbulent flow induces unsteady flow inside the short elbow pipe. These same results were also obtained when the experimental setup was tested for the same turbulent flow conditions. In Tanaka's [54] work, the formation of flow separation as well as the secondary flow development were observed in long elbows. These phenomena were shown to be highly influenced by the curvature radius of the elbow and its upstream velocity profiles. This flow separation and the secondary flow development were also observed in short elbow pipes. However, the flow pattern in the post-critical region of short elbow pipe was not mostly dependent on the Reynolds number of the flow, but rather on the interaction between eddy motion and unsteady secondary flow.

Kim [55] studied, both experimentally and numerically, the turbulent flow within a 90-degree-bend pipe as shown in Figure 1, with the hopes of determining the best turbulent flow model for the fluid. The mesh of the pipe cross-section used is an unstructured quadrilateral cell with 152,150 individual hexahedral cells at high Re values and 562,080 cells for the low Re values as in Figure 2. The value of Y+ non-dimensional distance to the wall of the pipe, both using friction velocity calculations for the near wall were within the range of 20 to 50 for a wall function and is less than 1 without wall function. Figure 3 demonstrates the streamwise velocity profiles near to the pipe elbow of the numerical results of Sudo et al. for the standard k-ε model. These models were selected based on the experimental data available. To select the best turbulent model, a quantitative assessment model was used. According to the results of that study, RNG k-Ɛ turbulence model provides the best predictions for estimating both the primary and the secondary stream-wise velocity as well as the swirl velocity profiles. Kim [55] used the RNG k-Ɛ model to predict the flow dependency on Reynolds number after pipe elbow section. Results of experimental as well as numerical simulations show that a strong relationship exists between Reynolds numbers at values of 50,000 to 200,000 and the stream-wise velocity profile. When swirling intensity, which was defined by Kim [55] as the area average tangential velocity, was observed for the same Reynolds number and at the same experimental conditions. Results showed that the swirl intensity is not strongly predicted by the Reynolds number. This work shows that after the elbow section of the pipe, the swirl velocity depends highly on the radius of curvature of the pipe bend; the swirl disappears faster as the curvature radius

increases.

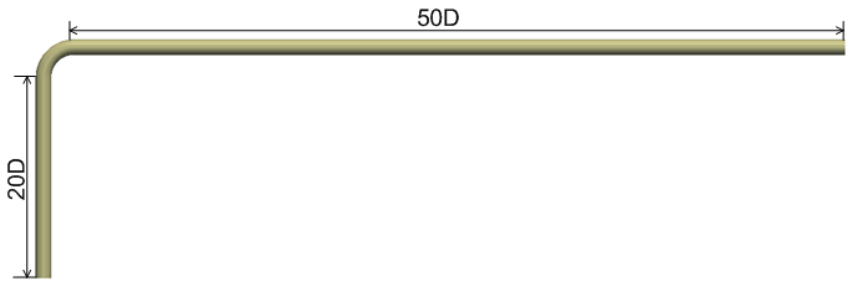

Figure 1. Computational geometry used in the simulation of flow in pipe with a 90˚ bend

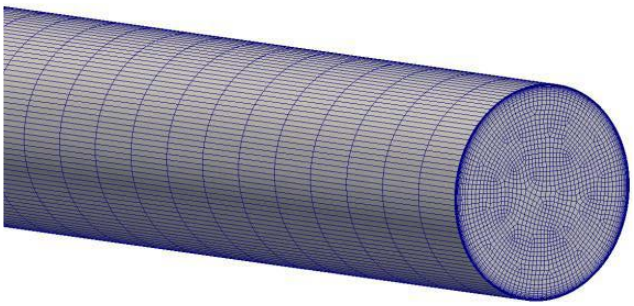

Figure 2. Computational mesh near pipe exit studied by Kim [55]

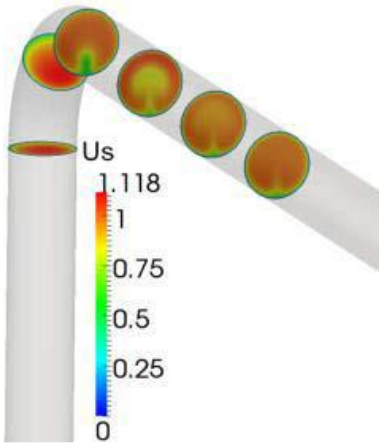

Figure 3. Streamwise velocity profiles results studied by Sudo et al. [40]

Rohrig [56] conducted a research which used numerical computation to analyze turbulent flow within a pipe with a 90° elbow. In this research a detailed numerical

study was done to compare the RANS (Reynolds-averaged Navier-Stokes) model and the wall-resolved eddy simulation model LES as tools for predicting turbulent flow of fluid inside a bend pipe. The computational grid and its cross-section are presented in Figure 4. While simulating the turbulent flow using the RANS equation, the researcher applied both the near-wall second-moment closure model, and the basic k-Ɛ turbulence model for low Reynolds numbers. The study demonstrated that wall-resolved eddy simulation model LES provides much better results than the RANS model, but these better approximations come at the cost of more computational time. Work by Rohrig [56] shows that it is possible to capture the location of secondary vortices and accurately predict flow velocity at the elbow. The strong pressure gradient causes the acceleration and deceleration of flow, which further affects the underlying turbulence.

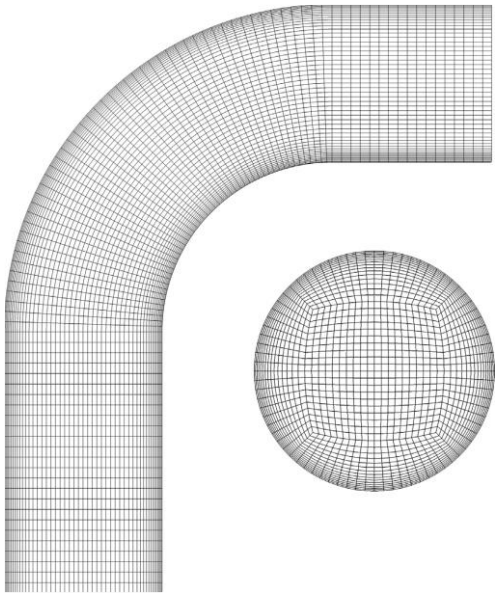

Figure 4. Two-dimensional slices of the computational grid for the geometry in the symmetry plane of the pipe bend and its cross-section by Rohrig [56]

Carlsson [57] studied turbulent flow in a 90°-bend pipe, aiming to uncover the origin of the swirl switching phenomena. A numerical model was set up to simulate the fluid flow inside the bend pipe, with LES as the basic model. Results showed that two different swirl switching phenomena occur at the pipe elbow section. One is called low-

frequency switching, and the other is called high-frequency switching. Both phenomena have their own origin. Simulations demonstrated that the high-frequency swirl switching could be highly influenced by the sharp bends which are intrinsic to the pipe bend. Low-frequency swirl switching was found to depend more on the upstream pipe bend length. It was also showed to be more powerful when the pipe curvature radius increases. This increase in strength continues all the way to a sharpest bend, at which point high-frequency swirl switching has more influence than the low-frequency switching. Carlsson [57] concludes that the high frequency in swirl switching may be caused by the strong backflow of fluid, which is generated at the pipe bend and is extended out of the pipe. He therefore recommended that the pipe length beyond the bend should be studied to find its effect on the high-frequency swirl switching phenomena.

In a numerical study, Wang [58] employed a large-eddy simulation to calculate and model the instant flow field in the right-angle elbow pipe in HTR-PM. The properties of the instant turbulent flow region under the control of boundary layer separation as well as secondary flow have been analyzed by evaluating the instant pressure details at different measurement points, as well as the velocity magnitude field at the cross-sectional elbow area. LES and RANS methods as well as simulations were used to analyze the complex behavior of flow in a 90° elbow to acquire details on turbulence. Results showed that the instant flow field was globally asymmetrical. The Dean Vortex structure and magnitude along with the small size eddies changed with time and caused flow field asymmetry. Counter-rotational forces and small and large eddies occurred in the area adjacent to the intrados. Flow patterns were disrupted by turbulent upstream distortion and the interplay of secondary flow with boundary layer separation. The comparatively smaller speed as well as pressure gradients in the fluid

next to the extrados lead to the homogeneous flow patterns on the outer semicircle at cross-sections.

Dutta's [59] studied flow separation and reattachment at different Reynolds stress numbers by computational modeling in the case of the 90° pipe bend. For this end, the researcher used the k-ε turbulence model. In the same experiment Dutta also collected experimental data for velocity profile including flow fluctuations on separation and reattachment points for varying Reynolds numbers in the central symmetry plane at different locations of the bend. A structured mesh in three dimensions was implemented consisting of hexahedron elements validated by a grid independence study shown in Figure 5. Similar mesh topology is constructed and will be used for this dissertation research.

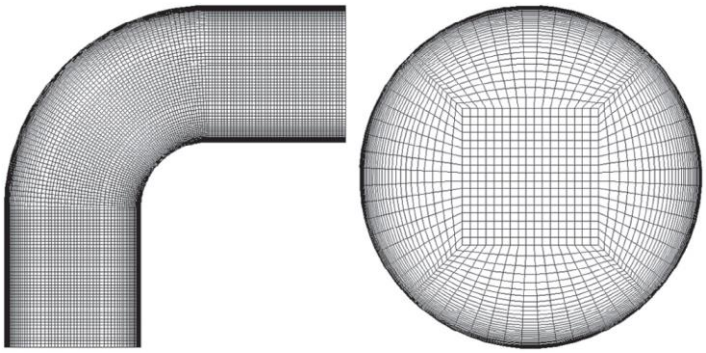

Figure 5. Computational grid of 90deg round pipe studied by Dutta [59]

The authors reported that the mean axial velocity profiles normalized with the air speed inlet at the inner core area show some deviation when compared to experimental data, and this is preliminary due to the pressure change. Simulations showed primary and secondary flow phenomena in distinct areas of the pipe bend, which illustrates the separation region as well as the velocity field. The numerical study demonstrated that the boundary layer separation with a small curvature ratio can indeed be easily observed at the bend. Velocity vector distribution explains the secondary

motion, evidently generated by the fluid movement from the bend's internal to external wall, resulting in the separation of the flow. The results also demonstrated that, when the Reynolds number is increased, the fully developed velocity profile at the region of the inner pipe core recovers by deceleration. Therefore, it was hypothesized that pipe curvature effects reduce in magnitude when Reynolds number increases. The study showed that the separation point travels upstream while the reattachment point moves more downstream when Reynolds number increases. Flow separation produced in the region of bend at the inner core was due to the formation of the low-velocity area. The peak value of velocity and its location was observed to be the same, while the peak value was measured away from the wall surface for only maximum Reynolds numbers. Three flow motions were observed at the downstream of the bend, including complexity, unsteadiness, and coherent flow nature.

Baramili [60] studied flow-induced vibration in elbowed piping systems using experimental methods. A turbulent duct flow environment was created using a closed water loop system with a transparent elbow attached. Data of flow dynamics was recorded using particle image velocimetry. Pressure on wall sections was recorded and calculated using the partial least squares regression (PLSR) method. POD was calculated discretely for specific pipe sections. Results showed that the POD technique turned seemingly random pipe turbulences into coherent structures as the fluid (water in this study) passed through the elbow joints. The characteristics of the main flow frameworks were related to fluctuations in wall pressure. Nevertheless, this connection was only established in the study zone and with significant time intervals. Nonetheless, a relationship was established among the patterns of wall pressure and the key flow systems using PLSR. Various time delays have found to be very useful in enhancing the quality of estimations. A velocity field prediction yielded a positive result as the

complexities of larger systems were replicated accurately.

Wang [61] investigated the unsteady fluid motion downstream in the 90° bend by way of Direct Numerical Simulation. An inflow turbulent condition was created using the recycling technique. Wang combined a long straight pipe in the downstream of the bend with a fixed Reynolds number and bend curvature. The diameter of the pipe was fixed. Numerous techniques were used to record low oscillations of downstream values, along with their frequency. Researchers believed that single-point velocity and stagnation point movement were not reliable for determining the frequency of swirl-switching. The fluctuations of the longitudinal pressure against the wall of the pipe and a half-sided mass flow rate were used as an indicator of the unpredictable downstream flow movements of the bend. The swirl-switching phenomenon was modeled using DNS. The value of the Reynolds number was set as 5300, and the bend curvature as 0.4. The unsteady oscillation of dean vortices was examined from the data inferred from the DNS bend pipe. The stagnation points are seen to be difficult to locate, so the exact condition relies on the range of the measurements. PSD and time series study of velocity variations along the symmetry axis clearly demonstrate that there are several dominant frequencies in the stream, different in specific flow regions. The experiment demonstrated that the oscillations of the force are amplified by the bend. Horizontal force oscillation and mass flow rate oscillation were shown to be interrelated. It was also observed that incorporated flow measures demonstrated more steadiness than single-point measurements. The whole analysis illustrates the significance of understanding global frequency determination procedures and partially addresses some of the data divergences in the publications. Table 1 summarizes the recent literature on turbulence modelling of curved ducts.

Table 1. Summarized Literature on Turbulence Modelling of Curved Ducts

Reference	R_e	$\delta = Rc/D$	Model
Rutten et al. (2005) [14]	2×10^4, 1×10^4, 2.7×10^4	$1, 3$	LES exclusive of SGS modeling
Tanaka et al. (2012) [47]	5×10^2, 5×10^4, 5×10^6	$1, 2$	LES including Smagorinsky SGS
Kim et al. (2014) [48]	5.08×10^4, 1.0×10^5, 2.03×10^5	3	RANS (k-ε and k-ω models)
Rohrig et al. (2015) [49]	1.4×10^4, 3.4×10^4	1.58	RSM along with LES Smagorinsky SGS, and RANS model
Carlsson et al. (2015) [50]	3.4×10^4,	1.56	LES with no SGS modeling
Wang et al. (2016) [51]	4.4×10^4	1.5	RANS and LES
Dutta et al. (2016) [52]	1×10^5, 1×10^6	1	$k - \varepsilon$ model
Baramili et al. (2018) [53]	5.6×10^5	1.50	$k - \varepsilon$ model
Wang et al. (2018) [54]	5.3×10^3	1.25	Direct numerical simulation

Tanaka [55] tested the performance of the LES technique with the standard Smagorinsky model for elbow geometries with different curvature ratios elbow geometries at Reynolds numbers from 500 up to 1.47×10^7. LES was able to simulate unsteady flow characteristics in the small elbow. The large-scale eddy motion was computed using the pressure fluctuation generation mechanism.

Liu et al. [56] showed the latest applications of LES. In their study, the interaction of cavitating flow over a hydrofoil was examined by aid of LES with a modified cavitation model. Moreover, they introduced a model for predicting pressure fluctuation that showed effective results. The mean average velocities obtained by

experiment and predicted by LES were quite similar, and overall experimental results were consistent with numerical results.

Saito [57] addressed the effect of wall surface roughness and high Re within the LES framework. A wall model corrected for roughness is implemented, where the developed information is transferred to the outer LES with the help of stretched vortex SGS model. LES is used to understand the flow dynamics of the channel over smooth as well as rough regimes. Numerical results confirmed experimental observations of logarithmic behavior.

As discussed earlier, the study of turbulent flow is difficult and requires a comprehensive and thorough analysis. In [3], it is explained that separation distance is strongly associated with turbulent flow. Hence, new pertinent literature is required to understand turbulence behavior. For this specific purpose, in this study, certain turbulence modelling concerns are discussed using different numerical modeling approaches.

CHAPTER 3: TURBULENCE MODELING APPROACH AND GOVERNING EQUATIONS

3.1 Governing Equations

Fluid dynamics seeks primarily to determine fluid motion properties such as the velocity field in each domain. The basic fluid dynamic equations that govern such motion can be obtained from both momentum and continuity equations.

3.2 Continuity Equation

The continuity equation can be written using the Einstein notation as follows:

$$\frac{\partial \rho}{\partial t} + \frac{\partial (\rho u_i)}{\partial x_i} = 0 \quad (1)$$

Where $u_i$is fluid velocity component in Cartesian axis x_i

The above equation is derived from the fact that the fluid mass is always conserved in a fluid system regardless of the system geometry or flow direction. The equation assumes there is no external body force. For incompressible flow, fluid density is assumed constant (ρ = constant) and independent from space and time; therefore, the equation reduces to:

$$\frac{\partial u_i}{\partial x_i} = 0 \quad (2)$$

3.3 Momentum Equation

The law of conservation of momentum states, in brief, that the momentum of an isolated system is constant. The momentum equation can be described using index notation as:

$$\frac{\partial(\rho u_i)}{\partial t} + \frac{\partial(\rho u_i u_j)}{\partial x_j} + \frac{\partial P}{\partial x_i} - \frac{\partial \tau_{ij}}{\partial x_j} = 0 \quad (3)$$

Where t is time, P is pressure and $\tau_{ij}$is Reynolds stress. Reynolds stress is defined as the transport of *i*-component momentum of fluid in *j* direction or vice versa.

The above equations are in Cartesian coordinates, and together they form the famous Navier-Stokes (NS) equations, which form the basics of fluid mechanics. Using the numerical method, it is possible to solve this PDE (partial differential equation) formulation of the Navier-Stokes equations.

3.4 Turbulence Models

Turbulent flow is accompanied by an unsteady eddy flow motion with wide-ranging scales structures superimposed on a slow time-varying or steady mean flow. Compared to laminar conditions, these eddies are responsible for much higher rates of mass and momentum transport in the fluid. At a high Reynolds number (*Re*), eddy scales can show a particularly high range. Typically, the ratio between the finest scale and the largest scale can be in the order of $\sqrt{Re}$ based on velocity gradients. The finest eddies have the highest energy dissipation rate. That is why it is challenging to compute turbulent flow numerically. A practical numerical methodology to compute turbulent flow must resolve all flow structures within this range. At a moderate Reynolds number, the flow can feasibly be resolved at the finer scales. However, very high Reynolds numbers still pose challenges to today's largest supercomputers. The experimental setup faces a similar challenge, as extremely small measurement volumes are required, as well as the ability to measure over large fluid zones relative to the overall flow-field domain.

In 1895, Osborne Reynolds [58] introduced the notion of decomposition of each variable included in the flow, to obtain an average as well as a fluctuating component. By averaging the governing equations, novel equations are reformulated with a distinct mean flow part that can relate to the corresponding part of the fluctuating motion.

$$Q(x,y,z,t) = \bar{Q}(x,y,z,t) + Q'(x,y,z,t) \tag{4}$$

Where Q is flow variable, $Q'$is fluctuating part and $\bar{Q}$ is mean part defined by

$$\bar{Q} = \frac{1}{N}\sum_{n=1}^{N} Q_n \tag{5}$$

The quantity N represents the total flow, realizations based on the number of times of ensemble.

An ensemble averaged NS equation is reformulated as follows by substituting Reynolds decomposition (4) into (2) and (3):

$$\frac{\partial \bar{U}_j}{\partial x_j} = 0$$

$$\frac{\partial(\bar{U}_i)}{\partial t} + \frac{\partial(\bar{U}_i\bar{U}_j)}{\partial x_j} = -\frac{1}{\rho}\frac{\partial \bar{P}}{\partial x_i} + \left(\frac{\mu}{\rho}\right)\frac{\partial^2 \bar{U}_i}{\partial x_j \partial x_j} - \frac{\partial \overline{U_i' U_j'}}{\partial x_j} \tag{6}$$

Where $\frac{\partial}{\partial t}$ is called the local derivation with respect to time, ρ is fluid density, $P$is fluid pressure, μ is fluid viscosity coefficient, the mean velocities $\bar{U}_i$ are determined by ensemble averaging. U_i' denotes the turbulence fluctuating part of the velocity.

For incompressible flow, the convective term is the only nonlinear term in the governing equation. Also, the only term which involves flow variable fluctuations is the Reynolds stress term. The Reynolds stress term is an effective turbulent stress term, described by the following equation:

$$\tau_{ij}|_{turbulent} = \rho\overline{U_i' U_j'} \tag{7}$$

The components τ_{ij} of the Reynolds stress tensor are defined in equation (7) and it needs correlation. This approach does not require resolving the entire unsteady flow motion. It is generally considered difficult to solve Reynolds stress as an equation as it is constituted by a set of unknown. The key to turbulence modeling is in finding numerical formulations that can be applied to link the Reynolds stress with the mean flow. In other words, it is a mathematical problem to find an enclosure solution for equation (7).

Generally speaking, if the flow is in free shear flow condition, the laminar stress term in equation (7), $\left(\frac{\mu}{\rho}\right)\frac{\partial^2 \bar{U}_i}{\partial x_j \partial x_j}$ can be treated in simple form by neglecting the viscous term in the momentum equation altogether. However, this simplification is inapplicable for wall-bounded flow conditions. In a wall-bounded flow situation, the Reynolds stress in equation (7) is dominantly found clear of the wall. Approaching the wall region, local flow velocity variations are gradually damped to zero. Moreover, viscous stress term is generally considered responsible for wall-bound friction.

There are different types of turbulence models. In this section, the following models are discussed: LES, RSM, $\zeta - f$ model (two-equation model), and WMLES. All these four numerical models have their unique advantages as well as disadvantages. In practice, LES is found to be useful for resolving large-scale unsteady flow motions. RSM is found useful for steady-state flow conditions. Steady flow implies no large-scale motion. The Reynolds stress term is modeled using the RSM approach. Like RSM, the two-equation model also treats the flow motion as steady-state. As opposed to RSM, the Reynolds stress term is largely based on Boussinesq eddy viscosity. The turbulence viscosity is modeled with the two-equation model.

3.5 Boussinesq Eddy Viscosity Model

As mentioned previously, for wall-bounded flow application, the closure problem requires a numerical solution by solving the Reynolds stress equation. The first numerical formulation was suggested by J. Boussinesq in 1877 [59] using the concept of eddy viscosity. The formulation later became known as the Boussinesq model. The model relates Reynolds stress to the mean flow. Based on Boussinesq assumption [59], the viscous stress tensor can be expressed by the following formulation:

$$\tau_{ij}|_{turbulent} = \mu\left[\left(\frac{\partial U_j}{\partial x_i} + \frac{\partial U_i}{\partial x_j}\right) - \frac{2}{3}\delta_{ij}\frac{\partial U_k}{\partial x_k}\right] \tag{8}$$

Where δ_{ij} represents Kronecker delta, defined as 1, if $i = j$ and 0 otherwise.

Equation (8) can be related to the Reynolds stress equation by the following.

$$-\rho\overline{U_i' U_j'} = \mu_t\left[\left(\frac{\partial U_j}{\partial x_i} + \frac{\partial U_i}{\partial x_j}\right) - \frac{2}{3}\delta_{ij}\frac{\partial U_k}{\partial x_k}\right] - \frac{2}{3}\rho\delta_{ij}k \tag{9}$$

Where turbulent kinetic energy k is defined as:

$$k = \frac{1}{2}\left(\overline{U_i'^2} + \overline{U_j'^2} + \overline{U_k'^2}\right) \tag{10}$$

In the momentum equation (3), viscosity is replaced by effective viscosity using the Boussinesq hypothesis:

$$\mu_{eff} = \mu + \mu_t \tag{11}$$

Where μ is the physical or molecular viscosity and μ_t is the turbulent viscosity due to turbulence mixing enhancement. The μ_t viscosity property assumes that turbulent structures exhibit isotropic characteristics. This also implies that the turbulence viscosity has no direction but only a value at a point-wise location. μ_t value is also required by another model.

3.6 Prandtl's Mixing Length Hypothesis

Using the kinetic theory of gases, Prandtl [60] used the equation (11) to model the molecular and turbulence viscosity. Prandtl mixing length hypothesis describes the corresponding viscosity using the following analogy:

$$\mu = \frac{1}{3}\rho \ell_f V_m \tag{12}$$

$$\mu_t = \rho \ell_m V_t \tag{13}$$

Where ℓ_f is the mean free path of the gas, ℓ_m is the mixing length of the gas, $V_m$is molecule velocity and V_t is the turbulence velocity scale.

For internal pipe flow application, Prandtl's model assumes that turbulence viscosity can be modeled using equation (13), $\mu_t \sim \rho \ell_m V_t$. The turbulence fluctuations in the pipe are assumed to be relatively weak compared to mean velocity, say $0.01 \leq \frac{V_t}{U} \leq 0.15$. It is observed that the mixing length of the gas can be related to the flow length scale in the pipe or the distance from the pipe wall. In experiment, it is found that turbulence flow mixing length (ℓ_m) in round pipe is proportional to $\frac{D}{4}$. Therefore, based on Prandtl's model, it is possible to make a good estimation of turbulence viscosity, $\mu_t = \rho(0.1U)(0.25D)$. Furthermore, the effective turbulence flow Reynolds number can be estimated with the following:

$$Re_{eff} = \frac{\rho UD}{\mu_t} = \frac{\rho UD}{0.025\rho UD} = 40$$

The effective Reynolds number is useful in identifying augmentation due to turbulence, which is not accounted for when using standard Reynolds numbers.

3.7 Direct Numerical Simulation (DNS)

To simulate turbulent flow, one of the most precise methods available is DNS. In DNS, the numerical grid considered needs to be fine enough to resolve even the smallest eddies. However, due to its high computational cost, the use of DNS is uneconomical for most engineering problems. For that reason, the RANS method is more widely used. The RANS method, while requiring less computational resources is unable to predict several complex flows, such as separation of flow, stagnation point flow, and curvature effects. The LES method, introduced by Smagorinsky [61], is capable of resolving large-scale vortices. It also parameterizes small-scale ones, which makes it more accurate than the RANS model. Computational expenses associated with LES generally fall between those of RANS and DNS. LES may not require meshes as fine as those present in DNS, but the grid must be better than that used for RANS computations. Hanjalic et al. [62] and Popovac and Hanjalic [63] presented a RANS model called $\zeta - f$ model, which is an important part of this study. The model by Hanjalic et al. is developed by using elliptic relaxation, discovered by Durbin. The purpose of the model is to solve transport equations for velocity scale ratios. It presents a comprehensive treatment of the wall-bounded conditions, which is used in RANS computation of heat transfer and turbulent flow. The computations with coarse and fine meshes are consistent with the experimental data. Therefore, this method is best suited for complex domain computations in industrial flow. In the following subsections, an overview of the turbulence modeling approaches implemented in this work is given.

3.8 $\zeta - f$ Model

The $\zeta - f$ model yields promising outcomes for several flows, particularly for separated flow. It is consisting of four transport equations, one for each of $k, \varepsilon, \zeta \; and \; f$

parameters (14)–(17).

$$\frac{\partial \rho k}{\partial t} + \frac{\partial (\rho u_j k)}{\partial x_j} = P - \rho \epsilon + \frac{\partial}{\partial x_j}\left[\left(\mu + \frac{\mu_t}{\sigma_k}\right)\frac{\partial k}{\partial x_j}\right] \tag{14}$$

$$\frac{\partial \rho \varepsilon}{\partial t} + \frac{\partial (\rho u_j \varepsilon)}{\partial x_j} = \frac{C_{\varepsilon 1} P - C_{\varepsilon 2} \rho \varepsilon}{T} + \frac{\partial}{\partial x_j}\left[\left(\mu + \frac{\mu_t}{\sigma_\varepsilon}\right)\frac{\partial \varepsilon}{\partial x_j}\right] \tag{15}$$

$$\frac{\partial \rho \zeta}{\partial t} + \frac{\partial (\rho u_j \zeta)}{\partial x_j} = \rho f - \frac{\zeta}{k} P + \frac{\partial}{\partial x_j}\left[\left(\mu + \frac{\mu_t}{\sigma_\zeta}\right)\frac{\partial \zeta}{\partial x_j}\right] \tag{16}$$

$$L^2 \nabla^2 f - f = L^2 \frac{\partial}{\partial x}\left(\frac{\partial f}{\partial x_j}\right) - f = \frac{1}{T}\left(C_1 - 1 + C_{2'}\frac{P}{\rho \epsilon}\right)\left(\zeta - \frac{2}{3}\right) \tag{17}$$

Where k is turbulent kinetic energy, ε is turbulent dissipation, ζ is normalized wall normal velocity scale, f is elliptical function, P is turbulent kinetic energy production, T is Kolmogorov time scale, C_1, $C_{2'}$, $C_{\varepsilon 1}$, $C_{\varepsilon 2}$ are closure coefficients

The biggest advantage of $\zeta - f$ model is that the turbulent kinetic energy production term, P can be accurately computed from velocity gradient and turbulent stress (τ_{ij}) as defined by the following equation.

$$P = \tau_{ij} \frac{\partial u_i}{\partial x_j} \tag{18}$$

$$\tau_{ij} = \mu_t \left(2S_{ij} - \frac{2}{3}\frac{\partial u_k}{\partial x_k}\delta_{ij}\right) - \frac{2}{3}\rho k \delta_{ij} \tag{19}$$

$$S_{ij} = \frac{1}{2}\left(\frac{\partial u_i}{\partial x_j} + \frac{\partial u_j}{\partial x_i}\right) \tag{20}$$

where $S_{ij}$is strain-rate tensor

Turbulent eddy viscosity (μ_t) is computed by imposing Kolmogorov time scale and length scale as the lower bounds from Durbin realizability constraints [64]. The following equations (21)-(23) are used.

$$\mu_t = \rho C_\mu \zeta k T \tag{21}$$

$$T = max\left[min\left(\frac{k}{\varepsilon}, \frac{0.6}{\sqrt{6}C_\mu|S|\zeta}\right), C_T\left(\frac{v}{\varepsilon}\right)^{1/2}\right] \tag{22}$$

$$L = C_L max\left[min\left(\frac{k^{3/2}}{\varepsilon}, \frac{k^{1/2}}{\sqrt{6}C_\mu|S|\zeta}\right), C_\mu\left(\frac{v^3}{\varepsilon}\right)^{1/4}\right] \tag{23}$$

Where L is Kolmogorov length scale, v is kinematic viscosity, C_μ, C_T, C_L are closure coefficients. The closure coefficients are given by the following:

$$\begin{gathered} C_\mu = 0.22, \sigma_k = 1.0, \sigma_\varepsilon = 1.3, \sigma_\zeta = 1.2 \\ C_1 = 1.4, C_2' = 0.65, C_T = 6, C_L = 0.36 \\ C_{\varepsilon 1} = 1.4[1 + (0.012/\zeta)], C_{\varepsilon 2} = 1.9, C_\eta = 85 \end{gathered} \tag{24}$$

Originally, the $\zeta - f$ was based on the model suggested by Durbin [64], known as $v^2 - f$ model. Durbin's models are based on the notion of elliptic relaxation that facilitates the solution of transport equations.

The current work uses a newly formulated ζ equation presented in (25).

$$\frac{D\zeta}{Dt} = f - \frac{\zeta}{k}P + \frac{\partial}{\partial x_k}\left[\left(v + \frac{v_t}{\sigma_\zeta}\right)\frac{\partial \zeta}{\partial x_k}\right] + X \tag{25}$$

$$X = \frac{2}{k}\left(v + \frac{v_t}{\sigma_\zeta}\right)\frac{\partial \zeta}{\partial x_k}\frac{\partial k}{\partial x_k} \tag{26}$$

Where $\frac{D}{Dt}$ is material derivative, X is cross diffusion term, σ_ζ is closure coefficient.

The actual implementation will omit cross diffusion term, X above since it is insignificance. Compared to the $v^2 - f$ model, the $\zeta - f$ model yields better results as ζ can be computed more efficiently. The term P in equation (25) stands for turbulent kinetic energy production and it is easy to accurately reproduce. Similarly, terms such as velocity gradient and turbulent stress are resolved more accurately in the $\zeta - f$ model. Due to these advantages, the $\zeta - f$ model provides benefits of robustness and improved efficiency in terms of computational expenses, which is the primary objective of this study.

3.9 Large-Eddy Simulation Model (LES)

The LES model is the preferred method for modeling flow at a high Reynolds number and complex geometry for projects in which DNS simulation costs are prohibitive [65]. The first LES technique was proposed by Deardorff [66] in 1970. The flow-field is filtered so the large or resolved-scale field becomes the local average of the global field. Filtered velocity can be expressed as:

$$\overline{u_i}(x) = \int G(x, x')u_i(x')dx' \tag{27}$$

Where bar symbol denotes the filtered field, prime symbol denotes the sub-filtered field, *G* is filtering function or convolutional kernel introduced by Leonard.

In LES, sub-grid-scale (SGS) stress tensor τ_{ij} can be acquired by the filtering process, which is defined in equation (28).

$$\tau_{ij} = \rho\overline{u_i u_j} - \rho\overline{u_i}\,\overline{u_j} \tag{28}$$

The appropriate modelling of SGS stress relies on certain critical assumptions. For this reason Smagorinsky [61] suggested using Boussinesq's hypothesis given in equation (29):

$$\tau_{ij}^s - \frac{1}{3}\tau_{kk}^s\delta_{ij} = \mu_t\left(\frac{\partial U_j}{\partial x_i} + \frac{\partial U_i}{\partial x_j}\right) = 2\mu_t\overline{S_{ij}} \tag{29}$$

Where μ_t represents the SGS eddy viscosity, τ_{kk}^s is the isotropic section in the SGS stresses, $\overline{S_{ij}}$ represents the strain rate tensor in resolved scales, L_s represents the mixing-length for SGS, C_s represents the Smagorinsky constant while Δ represents the local grid scale.

$$\mu_t = \rho L_s^2|\bar{S}| \tag{30}$$

$$\Delta = (\Delta x\, \Delta y\, \Delta z)^{\frac{1}{3}}$$

It should be noted that τ_{kk}^{s} needs to be included in the filtered static pressure. Smagorinsky borrowed the concept of the "mixing-length model" from the RANS model and used it to determine eddy viscosity.

The Smagorinsky model has some significant shortcomings. Firstly, the C_s value is flow-dependent, and several values are reported in the literature, ranging from $C_S = 0.065$ (Moin and Kim, 1982 [67]) to $C_S = 0.250$ (Jones and Wille, 1996 [68]). The value is therefore not actually a constant, as it is treated by the model. Moreover, this model is very dissipative and is not suitable for processes like boundary layer transition. A novel model, now known as the dynamic Smagorinsky-Lilly Model tackles those concerns by calculating the C_s using resolved eddies of the flow [69]. By computing the model coefficient dynamically, the new model could overcome the drawback of existing sub-grid scale stress models. Lilly [70] further improved the dynamic Smagorinsky model by using the least-squares technique. This technique enables the reduction of resolve stress assumption difference, which makes the model more suitable for practical applications.

Similarly, by considering the influence of rotation rate tensor of resolve eddies along with strain rate tensor, Nicoud and Ducros (1999) presented another sub-grid scale model [71]. The model calculates the eddy viscosity using the formula shown in (31).

$$\mu_t = \rho \Delta_s^2 \frac{(S_{ij}^d S_{ij}^d)^{3/2}}{(\bar{S}_{ij}\bar{S}_{ij})^{5/2} + (S_{ij}^d S_{ij}^d)^{5/4}} \tag{31}$$

$$\Delta_s = C_w V^{1/3}, C_w = 0.325 \tag{32}$$

$$\bar{g}_{ij} = \frac{\partial \overline{u}_\iota}{\partial x_j}$$

$$\bar{g}_{ij}^2 = \bar{g}_{ik}\bar{g}_{kj}$$

$$\bar{S}_{ij} = \frac{1}{2}\left(\frac{\partial \bar{u}_i}{\partial x_j} + \frac{\partial \bar{u}_j}{\partial x_i}\right)$$

Where S_{ij}^d is symmetric part of the squared velocity gradient tensor, $\delta_{ij}$is Kronecker symbol, C_w is WALE constant, V in the model represents computational cell volume.

The model accurately predicts near-wall behavior of eddies (i.e., asymptotic in nature), which is why it was named wall-adapting local eddy-viscosity (WALE) model. Precise representation of flow the near-wall region helps in determining wall-bounded turbulent flow.

3.10 Wall-Modeled LES Model

Although the LES decreases the computational grid concerning the DNS method, a literature survey shows that it still requires a very fine mesh to simulate conventional turbulent flows. The following equation shows the ratio of computational cells number for LES and DNS:

$$\frac{N_{LES}}{N_{DNS}} \approx \left(\frac{0.4}{Re_\tau^{1/4}}\right) \tag{33}$$

Where N_{LES} represents number of grids in LES model and N_{DNS} is number of grids required for DNS, Re_τ is Reynolds number based on wall shear stress.

Table 2 compares the required computational grid for the DNS and the LES for a channel flow with a characteristic length of H. As can be seen, for practical flows with Reynolds number of at the order of 10^5, LES requires 10^8 computational cells, which still is very high. To circumvent the limitations of LES Reynolds number scaling, Shur et al. [72] introduced the wall-modeled LES (WMLES) approach which is classified in the hybrid RANS-LES category. WMLES simulates the main flow with

LES while employing the RANS approach in the buffer layer (log-law layer). Table 3 represents the computational cell number ratio for LES and WMLES approaches. The table shows that WMLES decreases the mesh cells and, consequently, the computational cost of simulation. [73]

Table 2. Computational Grid Comparison for DNS and LES

Re_H	Re_τ	N_{DNS}	N_{LES}
12,300	360	6.7E6	6.1E5
30,800	800	4.0E7	3.0E6
61,600	1,450	1.5E8	1.0E7
230,000	4,650	2.1E9	1.0E8

Table 3. Computational Grid Comparison for LES and WMLES

Re_τ	N_{LES}	N_{WMLES}	$\frac{N_{LES}}{N_{WMLES}}$
500	5.0E5	5.0E5	1
1E3	1.8E6	5.0E5	1E1
1E4	1.8E8	5.0E5	4E2
1E5	1.8E10	5.0E5	4E4

3.11 Reynolds Stress Model (RSM)

RSM is useful in modeling flow with non-isotropic characteristics. In a mathematical framework, it states:

$$\tau_{ij}|_{turbulent} \neq \mu\left[\left(\frac{\partial U_j}{\partial x_i}+\frac{\partial U_i}{\partial x_j}\right)-\frac{2}{3}\delta_{ij}\frac{\partial U_k}{\partial x_k}\right] \tag{34}$$

The non-isotropic flow characteristics appear in flow through square and non-circular channels, or channels with curved cross-sections. They also occur in complex flow with a strong rotational effect. The transport equation for the model was developed by Chou (1945) [74] and it goes as follows:

$$\frac{\partial}{\partial t}\left(\rho \cdot \overline{U_i' U_j'}\right) + \frac{\partial}{\partial x_i}\left(\rho \cdot U_i \cdot \overline{U_i' U_j'}\right) \tag{35}$$

$$= D_{ij} - \rho \cdot \left[\overline{U_i' U_k'} \frac{\partial U_j}{\partial x_k} + \overline{U_j' U_k'} \cdot \frac{\partial U_i}{\partial x_k}\right] + \Phi_{ij} - \varepsilon_{ij}$$

Where Φ_{ij} is pressure strain term, D_{ij} is turbulent diffusion term ε_{ij} is dissipation term.

The first term at the left of the equation represents the unsteady part. The term following it represents convection. First term on the right denotes diffusion, whereas the other terms are in the order as follows: production, redistribution, and dissipation. The above equation can be interpreted as the rate at which Reynolds stress changes together with the transmission of Reynolds stress by convection equals the transmission of Reynolds stress by diffusion plus the rate at which the Reynolds stress is produced plus the transmission of Reynolds stress due to the interaction of turbulent pressure-strain plus the transport of Reynolds stress (due to rotation) plus the rate at which the Reynolds stress dissipates. To solve this PDE, pressure strain terms need to be modelled in association with the dissipation term, as these terms are open and require closure models. On the other hand, the production term is closed and can be directly evaluated without explicit modeling. The disadvantage of RSM is its computational expense due to seven extra PDE that need to be solved. The production term in equation (35) can be written as $-\rho \cdot \left[\overline{U_i' U_k'} \frac{\partial U_j}{\partial x_k} + \overline{U_j' U_k'} \cdot \frac{\partial U_i}{\partial x_k}\right]$ represents the mean velocity gradient motion which acts opposite to the Reynolds stress. This term considers the kinetic energy transfer from mean flow to the fluctuation's velocity components. It is responsible for sustaining the energy transfer from large to small-scale eddies in turbulent flow. This is the only term in the RSM transport equation that is closed and can be evaluated directly, without a model. Table 4 compares the models used in this research in terms of their advantages, and their disadvantages.

Table 4. Performance Comparision of the Turbuelnce Models

Model	Advantages	Disadvantages
RSM	Exceptional modeling of complex flow phenomena, acceptable cost	Low performance in predicting flow separations and re-circulating flows
LES	Acceptable performance	Higher cost and requires more time than other models
ζ-f	Exceptional performance, low cost	Requires modeling for each application use
WMLES	Fair performance, low cost	Cannot predict transition to turbulent flow as they assume developed turbulence

CHAPTER 4: MODELING OF FLOW PHENOMENA IN Z-SHAPED AND HIGHLY CURVED DUCTS

Turbulent flow in a Z-shaped ducts is not exhaustively studied in the literature. Flow in curved ducts is characterized by particularly complex behavior. Turbulence in flow through the duct can be dramatically affected by streamline curvature. For example, the flow field is destabilized by a concave curvature, leading to greater intensity of turbulence as well as its scale. Convex curvature, on the other hand, leads to a more stable flow field, a lessening of turbulence mixing, lower Reynolds shear stress as well as less kinetic energy [75]. Even in simpler curved ducts, such as the elbow draft tube which only has one elbow, very complex flow is present. It is a flow that is a result of the combined effects of flow and curvature, swirling flow and adverse pressure gradient diffuser flow [76]. The internal fluid flow field in a highly curved wall-bounded pipe such as the Z-shaped duct is further complicated by the presence of a centrifugal force at both upstream and downstream turning radius sections. Highly curved wall shape changes the flow field inside the duct in several ways. These effects include; (1) viscous effect due to no-slip boundary condition; (2) blocking effect due to wall suppression in normal direction; (3) effect of shearing mechanism on turbulent production; (4) surface roughness effect; and (5) effect of wall reflection due to redistribution of stress components [1], [77], [78], [79], [80], [81].

4.1 Viscous effect due to no-slip boundary condition

The no-slip boundary condition, or the no velocity offset boundary condition is present when the speed of fluid touching the wall is the same as the velocity of the boundary. This means that the velocity of the fluid in contact with the solid boundary

tends to zero, due to surface friction. The hypothetical distance in the boundary layer where velocity reaches zero relative to the velocity of the boundary is called the slip length. The slip length dependents only on the fluid characteristics and the solid boundary, as well as their interactions, and can therefore be determined experimentally, at least in theory. One of the earliest approaches to estimate the slip boundary condition was proposed by Pearson and Petrie, which made slip velocity a function of wall shear stress, using empirical data. Newer research proposed a polymer network model to account for the dynamic slip velocity [82].

4.2 Blocking effect due to wall suppression in normal direction

Blocking effects of the wall are a result of its non-slippery and impermeable characteristics, which cause fluctuations of parallel velocity as well as a suppression of perpendicular velocity fluctuations. Blocking effects on intersecting walls cause pressures in the surfaces near the elbow increase relative to that near the regions where the wall is orientated in one direction. The higher pressure directs fluids above the wall away from the elbow bend. Stemming from the wall blocking effect, stagnation points of flow, known as splats, can form. These stagnation points are formed as an effect of the fluid impinging the wall. Research shows that these splats may cause problems for wall-bound large eddy simulation predictions. These splats can also have an effect on turbulence intensities [83].

4.3 Modeling Wall-Surface Roughness Effects

The surface coarseness has an important effect on the flow for highly curved ducts due to the mass transfer on the walls and induced drag resistance. In this study, the wall is treated as smooth. The wall shear stress is modeled such that it progresses

along the fluid flow through a viscous sub-layer. The configuration of velocity fluctuations in the viscous sub-layer is like the one described in Couette flow condition, where $U = u_\tau^2 y/v$. The thickness of the sublayer is expressed as $\delta_{lam} = Cvu_\tau^2$, where the constant, *C* is the velocity value just before it becomes nonlinear. A. K. Sleiti [84] reported that $K_S^+ = \rho K_S u^*/\mu$, where K_S is the physical roughness height. Moreover, he observed that K_S^+ falls under three different regimes as follows; hydro-dynamically smooth with $K_S^+ \leq 2.25$, for transitional the K_S^+ is between 2.25 and 90 i.e. $(2.25 < K_S^+ \leq 90)$, and for completely rough when $(K_S^+ > 90)$ [84]. The FLUENT solver computes the function of the dimensionless roughness height ΔB for each regime using the formulas proposed by Cebeci and Bradshaw [85] and it is shown in equation 36 below. In hydraulically smooth walls the viscous sublayer is fully established, while in transitional roughness regime the roughness elements are a bit thicker than viscous sublayer so it disturbs it, however, in the fully rough flows the sublayer is destroyed and viscous effects are insignificant. [86]

$$\frac{u_p u^*}{\frac{\tau}{\rho}} = \frac{1}{k}\ln\left(E\frac{\rho u^* y_p}{\mu}\right) - \Delta B \tag{36}$$

$$u^* = C_\mu^{\frac{1}{4}} k^{\frac{1}{2}} \tag{37}$$

$$\Delta B = \frac{1}{k} ln f_r \tag{38}$$

Where u_p is friction velocity, $u^*$is non-dimensional velocity, τ is wall shear stress, y_p is wall coordinate or distance to the wall, *B* is intercept or addictive constant in log-law, C_μ is, f_r is roughness function that determines the intercept shift depends on roughness effect, *k* is Von Karman constant.

4.4 Near-Wall Treatment

In this work, enhanced near-wall treatment method was implemented in the model. This method is useful for resolving the near-wall viscosity affected region. This region also includes a viscous sub-layer. That approach is sometimes called the “Low-Reynolds Modeling”. That is because most computational studies of near-wall turbulence were based on Direct Numerical Simulation (DNS), which constrains the range of Reynolds numbers significantly. In fact, most simulations treated near-wall turbulence in simple flows (planar channels) and at low Reynolds numbers. Compared to the standard wall function, near-wall treatment shows improved shear stress results near the grid refinement wall region in the wall-normal direction even at y+ < 10 [1]. A study done by A. K. Sleiti [84] demonstrated the effectiveness of the standard wall function. The performance of enhanced near-wall treatment with the use of a joined two-layer model of wall functions is summarized as follows.

Using standard wall function in the near-wall treatment method gives advantages of saving computational resources and is thus economical. However, it was reported that it is not recommended for low-Re flow in a small gap and not recommended for acute pressure gradients heading toward boundary layer separations or for turbulent flow that exhibits strong body forces [84]. The combined two-layer model is used accompanied by enhancing the near-wall treatment approach, where the ε and the μ are specified using the initial two layers. Here, μ represents the turbulent viscosity. The recommended near-wall mesh consideration is $y^+ = 1$. Nevertheless, $y^+ < 4 - 5$ is acceptable and can be adopted. A minimum of 10 cells is essential inside the near-wall region influenced by the viscosity (Re_y<200) [84].

4.5 Secondary Flow Effects

Flow of fluids passing through a curved duct is different at a fundamental level from flow through a straight passage. The cause for this distinction lies in secondary flow which is generated by centrifugal forces which occur in flow through a curved duct. These centrifugal forces create a lateral pressure gradient which causes the creation of secondary counter-rotating vortices [87]. In general, the secondary flow effects can be classified into two types. The first type is generated by the inviscid effect. The second type is generated by Reynolds stress. The inviscid effect causes secondary flow when the span-wise pressure gradient appears during mean flow. Reynolds stress type secondary flow is induced by turbulence, near the duct turning corner [1]. These two categories of steady secondary currents in fluid flows are identified by Prandtl [88]. Since secondary flows are under the influence of the gradients of Reynolds stresses, it is impossible to capture them using an isotropic eddy-viscosity model [84].

4.6 Effects of Curvature

Flow in highly curved ducts with turning radiuses on a higher side leads to a linear pressure gradient. Near the duct centerline, the fluid with high momentum tends to drift outwards. The reverse flow is developed along the wall, due to momentum balance. The curved shape of the duct, via the centrifugal forces, creates a pair of vortices counter-rotating in relation to each other. At certain conditions, more pairs of vortices can appear concave wall in the duct. These additional vortices are commonly known as the Dean vortices. These vortices cause instability in the hydrodynamic configuration of the flow system, at the base secondary flow. The number of these ancillary Dean vortices falls under the influence by the shape of the ducts, that is their aspect ratio [87].

The Dean number parameter measures the curvature effect corresponding to fluid viscosity [1]. $De = Re(D_h/R)^{1/2}$ where R is the curvature radius and D_h is the pipe diameter. The Dean number provides insight of flow stability. According to Rayleigh's criteria, when critical the Dean number is exceeded, the flow is considered unstable. In the case of the bend pipe the inner side (convex) is stable, and the outer side (concave) is unstable. Since flow stability is affected by fluid viscosity, it is important to include this effect in the turbulence modeling [84].

4.7 Effects of Separation Distance

Lateral separation distance between upstream and downstream turning corners in the Z-shaped duct influences duct flow in a way to induce restriction in the vertical pipe. The restriction is influenced by downstream turning corner distance. A study was made in this research to determine the effects of separation distances on turbulence model. In LES model, separation distance did impact how accurately LES can predict the flow in close-coupled five-gore elbows in a Z-shape configuration. LES predicted flow velocity profiles more accurately at a separation distance of ten than at a smaller separation distance of two [89], as shown in Figure 6 and Figure 7.

	EW	NS
L/D=2	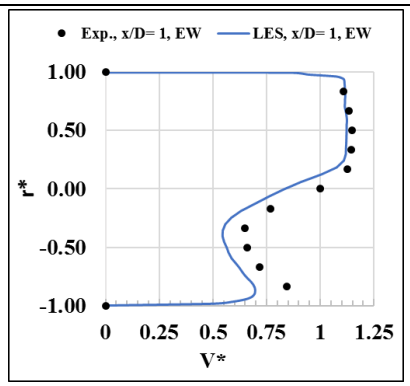	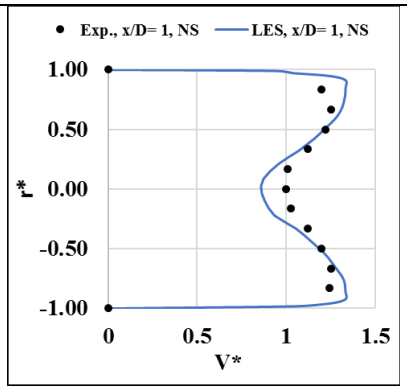

Figure 6. Mean flow velocity profiles at x/D = 1 for L/D = 2

	EW	NS
L/D=10	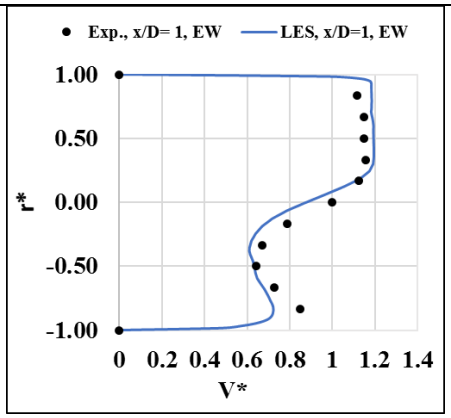	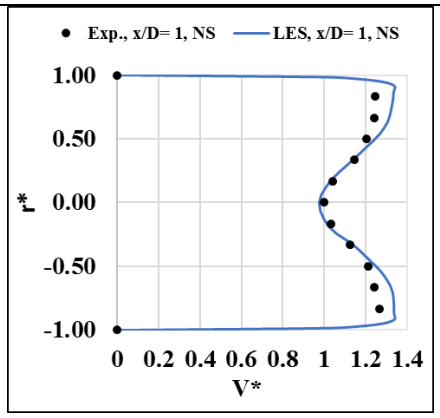

Figure 7. Mean flow velocity profiles at x/D = 1 for L/D = 10

4.8 Rotational Effects

The rotational effects generate centrifugal (f_i^{ce}) and Coriolis forces (f_i^{co}) [84] that are expressed in the following equations:

$$f_i^{ce} = -\rho\varepsilon_{klm}\Omega_j\Omega_l x_m \tag{39}$$

$$f_i^{co} = -2\rho\varepsilon_{ijk}\Omega_j U_k \tag{40}$$

Where Ω_j is angular velocity vector, ε is tensor

Pallares and Davidson [90], investigated the relationship between the Prandtl secondary current flow and Reynolds stresses induced flows (the 2nd kind) using the

LES model. They found that the increase in the rotational numbers leads to the dissipation of the vortices near the corners. They have also found that the cross-stream secondary motions are influenced by the Coriolis force [84]. Research showed that the RSM model allows for better prediction than the isotropic two-equation models. Researchers suggested that that the RSM can perform well when the effects of both the rotation, the streamline curvature and the anisotropy on flow dynamics need to be considered, without requiring any explicit modeling. RSM performed well even at high rotational numbers (up to 1.29) and high-density ratios (up to 0.4) [91]. The study also found that high levels of rotation cause linear increases in four-side-average Nusselt number area. Another study found that centripetal forces that are associated with the rotation directly influence both the mean motion and the turbulent fluctuations in the flow. These forces operate as to induce a secondary motion and influence the turbulence by modifying the pressure strain [92].

4.9 Reynolds stress model for Z-shaped ducts

The RSM is a result of a calculation of individual Reynolds stresses which are used to resolve the Reynolds-averaged momentum equation. RSM does not use the eddy viscosity approximation. Instead, it solves the Reynolds stress tensor equations directly, which allows it to have potential to predict complex flows with evident anisotropic effects. The downside to RSM is that solving the equations is complex, and requires relatively more computational power and time and can result in problems in convergence. Another limitation of the RSM is that several variables needed for its resolution are unknown, and therefore need to be estimated to resolve the model, which can generate errors.

In another study [93] Reynolds stress model was used to predict the turbulent

flows in ducts with strong convex and concave curvature. The author indicated that the turbulence complexity generated in these ducts would require a model which capabilities are above the standard eddy viscosity models. Reynolds stress model fits that criteria, and once incorporated in a Navier-Stokes procedure, it gave satisfactory results [87]. The model predicted the relevant phenomena in the 180° duct, including the sharp increase of turbulence at the region near the concave wall, the significant diminishment of turbulence at the convex wall region as well as the downstream separation of the convex wall which follows [93].

The findings show that Reynolds stress model has the required capabilities for modeling turbulent flow through complex curvatures, such as z-shaped duct, well. However, its cost limits its use in practical applications.

4.10 Large eddy simulation model for Z-shaped ducts

Large eddy simulation model decomposes the variables included in flow phenomena into, on the one hand, a large-scale component and on a small-scale component on the other. The decomposition is achieved by a filtering operation. This is so that only the large eddies, which strongly depend on flow characteristics, need to be resolved using numerical methods. To model the fine scale turbulence, a subgrid scale model is used. Large eddy simulation model demonstrated good accuracy and stability in curved ducts. Several studies showed that the numerical results obtained by large eddy simulations were in good agreement with experimental data available, making large eddy simulation a suitable method for predicting complex flow, such as that in curved ducts [94]. The performance of large eddy simulation was tested both against flow field data, as well as against the effects of the inclination angle, which has important implications for industrial applications. Researchers also investigated the

performance of large eddy simulations in highly curved ducts (180° bend), and compared the different components of the method [95]. These conditions require special consideration in developing the proper large eddy simulation, so that the complex flow modeling can accurately reflect real experimental data. They concluded that, to accurately model the flow in a curved duct, real inflow and outflow boundary conditions have to be used [95]. It is difficult to achieve real inflow and outflow boundary conditions since unsteady flows in vortices need to pass the boundary with little disturbance and reflection. The large eddy simulation also requires that a time dependent velocity field, with all three velocity components, is accurately specified, which can be a cause of errors. All these findings show that large eddy simulations are an appropriate, but not best tool for modeling turbulent flow through complex curvatures, such as the z-shaped duct.

4.11 ζ-f model for Z-shaped ducts

ζ-f model has been derived from the Reynolds stress transport model by Hanjalić and his associates. It is a modified $\overline{v^2} - f$ model which does not suffer from a need of multiple iterations for convergence. It depends on the turbulence kinetic energy production, which can be reproduced more easily than the dissipation used for $\overline{v^2} - f$ model. It also uses a "cross diffusion" term which is used to accurately represent and model near-boundary conditions. It has a better numerical stability than the V2F model and does not require an intermittency function. The ζ-f model has an advantage in computational time and cost when compared to the Reynolds stress model, while its results are similar to those of the RSM. [96].

The ζ-f model can predict complex transitional flows present in the Z-shaped ducts, and its lower cost and computational time make it a promising model for

industrial application.

4.12 Wall-modeled Large Eddy Simulations model for Z-shaped ducts

Recently, numerous wall modeling approaches have been implemented to make modeling for industrial applications practical. Most of these models are various developments of the wall-stress model. In this approach, inner boundary section is not directly computed. Instead, it is replaced by an equal momentum exchange. The equal momentum exchange with the wall is achieved with the use of a boundary condition. An empirical wall model is then implemented to estimate wall friction using flow information transferred downstream from the wall. That way wall friction does not need to be examined or computed directly. Afterwards, the obtained data on wall friction is used as an input in the WMLES model, as a Neuman boundary condition with fluctuating velocity near the wall region, but never penetrate it [97]. There are several WMLES models in the literature, as the model can be changed depending on the complexity of required calculations in each setup. This gives it flexibility which is critical for industrial use. However, in flows through complex curvatures, such as the Z-shaped duct, the advantages are less evident, since the complexity of the turbulent flow is more difficult to represent. Research has found that the WMLES model can accurately predict transient velocity profile of turbulent flow, but exhibits some errors when approximating friction magnitude and friction angle when using the initially established streamwise direction [97]. The model needs to be improved further to allow for reliable use in the modeling of complex flow.

4.13 RSM, LES, ζ-f and WMLES models in Z-shaped ducts

The following will be an overview of various models used in this study and an

analysis of their relative advantages and disadvantages in relation to predicting turbulent flow phenomena in a Z-shaped duct. All models show promising results, and RSM and ζ-f being exceptionally promising and showing substantially more accurate results. However, while the implementation of Reynolds stress model is relatively expensive and with high cost of computation and required time, ζ-f can achieve similar results at significantly lower cost. That makes ζ-f model promising for industrial applications.

CHAPTER 5: NUMERICAL APPROACH AND BOUNDARY CONDITIONS

5.1 Discretization

The Navier-Stokes partial differential equation is numerically resolved with the help of the control volume technique, mainly implemented for integrating governing equations applied to individual control scheme. The software used for this purpose is commercial software called Ansys [98].

5.2 Second-order Upwind Schemes

ANSYS Fluent stores the flow variable at the cell centers numerically. However, the convection terms in the governing equation require the face values of the cell. Therefore, the upwind scheme is implemented. The upwind scheme determines the face value from upstream of the cell (or “upwind”) comparable to the trend of normal velocity. The upwind arrangement is one of the most stable and simplest discretization schemes. The drawback of such a scheme is that it is found to be more dissipative depending on the flow of physics. The second-order upwind arrangement is more accurate than the first-order arrangement.

5.3 Momentum Equation Discretization

To discretize the momentum equation, x, y, and z spaces are used. Co-located schemes are used by the software ANSYS Fluent. These schemes store pressure and velocity at the cell centers. In Fluent, the momentum equation is numerically solved based on velocity and pressure discretization.

5.4 Pressure Interpolated Scheme

When discretizing the momentum equation, face pressure values are determined using the pressure interpolated scheme. The momentum equation coefficients are used to achieve the interpolation. This scheme works well for smooth gradients between cell centers. However, the interpolation fails when the neighbor control volumes have large gradients. A cell velocity overshoot or undershoot occurs because of this interpolation discrepancy.

5.5 Continuity Equation Discretization

With the help of Fluent software, equations of continuity and momentum are resolved sequentially by means of a segregated solver. An algorithm called SIMPLE (Semi-Implicit Method for Pressure-Linked Equation) is implemented to solve the continuity equation by introducing pressure.

5.6 Pressure-Velocity Coupling Approach

Another approach used to predict incompressible flow. To enforce the mass conservation, a SIMPLE algorithm is applied so it can determine the pressure field by computing both velocity and pressure corrections iteratively. Other pressure-velocity algorithms include SIMPLE (SIMPLE-Consistent) and PISO (Pressure-Implicit with Splitting of Operators).

5.7 Multigrid Method

To solve for the pressure variable, it is essential to use the Multigrid Method when conducting matrix operations. In Fluent, both algebraic type multigrid (AMG)

and full-approximation storage (FAS) type multigrid are available. The global (low frequency) error is found to be reduced by using the Multigrid method with sequentially coarsening meshes.

5.8 Experimental Data and Setup

This study uses data from A. K. Sleiti and Salehi et al. (2017) [1] to validate results obtained from numerical methods. To study the pressure losses and velocity profiles related to round five-gore elbows, the experimental setup given in **Error! Reference source not found.** is implemented. ASHRAE provides a standard to measure the pressure loss along with the present volumetric flow rate. The measurements on the ductwork and fittings are done to be consistent with the ASHRAE standard 120-2008. After measuring pressure loss through elbows, several tests specifically devised for assessing the friction factor in remaining pipes were conducted. To ensure uniform inlet flow, the entrance of the ductwork was connected to a bell mouth. For the elbows, a fixed turning radii value (i.e., 1.5) was used. Upstream and downstream duct lengths were 1.2 m each. The intermediate length for closed couple elbows was changed from $0\ m\ to\ 3.05\ m$. The intermediate length was measured starting from exit up to the entrance plane of the upstream and downstream, respectively.

To provide the air flow through the test equipment, a 30 hp fan was used. The details of measured values at the test was used to estimate the volume flow rate. A multiple-nozzle chamber was employed, and for pressure loss measurement, a liquid-filled micro-manometer with the accuracy of ±0.025 mm was used. It was also used to measure the nozzle pressure at the test section. Electric manometers with the measuring accuracy of ±0.025 mm was used to quantify the upstream as well as downstream static

gage pressure. The flow rate was controlled with the use of a VFD. A mercury thermometer with a precision of ±0.6°C (1°F) was placed in the nozzle chamber, to measure air temperature. Similarly, ambient air temperature for dry and wet bulb was measured with a psychrometer. To measure ambient pressures, a Fortin-type barometer was used. For each test apparatus, eight test points were obtained, and all were evenly spaced over the test range.

Velocity profile measurements for Z-shaped ducts with intermediate section lengths and apparatus arrangement on the 305 mm diameter equipment were taken using a five-hole probe. For the first elbow, on the upstream, a traverse plane was placed, and another was placed at the downstream of the second elbow. Both planes were placed exactly at one duct diameter, upstream or downstream. At several locations in the straight sections, thorough velocity profile measurements were done. The locations of these profiles are given in Table 5 with their corresponding intermediate lengths. x/D. Initially, the placement of a five-hole probe was done at the centerline; afterward, it was changed with respect to radial increments of $25.4\ mm$ as Figure 9 (b) shows. The placement of sensing tip of the five-hole probe on the duct centerline was done with an accuracy of $\pm 1.25\ mm$. Air velocities in each implemented transverse were determined in two equally perpendicular planes that separated the cross-sectional area of the duct into further parts (i.e., four quadrants).

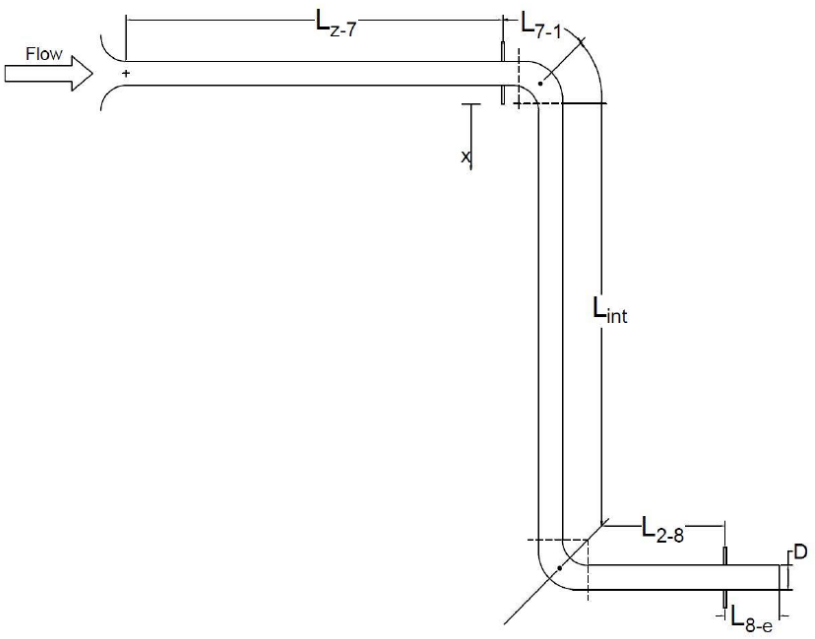

Figure 8. Experimental Set-up of Measuring Pressure Loss for Close-Coupled Elbow Z-Configuration [1]

5.9 Computational Domain and Boundary Conditions

Figure 9 shows a Z-shaped duct with a diameter equal to 304.8 mm. The geometry of the given Z-shaped duct consisted of three parts. The first part is a pipe inlet with a 15D horizontal section, a vertical section with separation distance, and a pipe outlet with a 10D horizontal section. For the vertical section, the gap between two elbows was investigated using a different methodology, using five instances of L/D value (i.e., L/D = 2, 4, 6, 8, and 10). L represents the separation distance length, and D represents the pipe diameter. For the boundary condition at pipe inlet, the value was an experimental Reynolds number (Re) and was tuned to velocity inlet wit $\mathrm{Re} = 3.5 \times 10^5$. The outlet boundary condition was posited as a pressure outlet. To develop the flow completely inside the duct, its entrance was extended. It was assumed that the walls of the duct were at the non-slip condition. To develop the computational grid where the cell type is hexahedral, a commercial software called ANSYS Fluent was

used. From Figure 10, in bending geometry, the mesh was further refined by 30%. Similarly, to keep y^+ as low as possible, the mesh was also refined, particularly at the near-wall region.

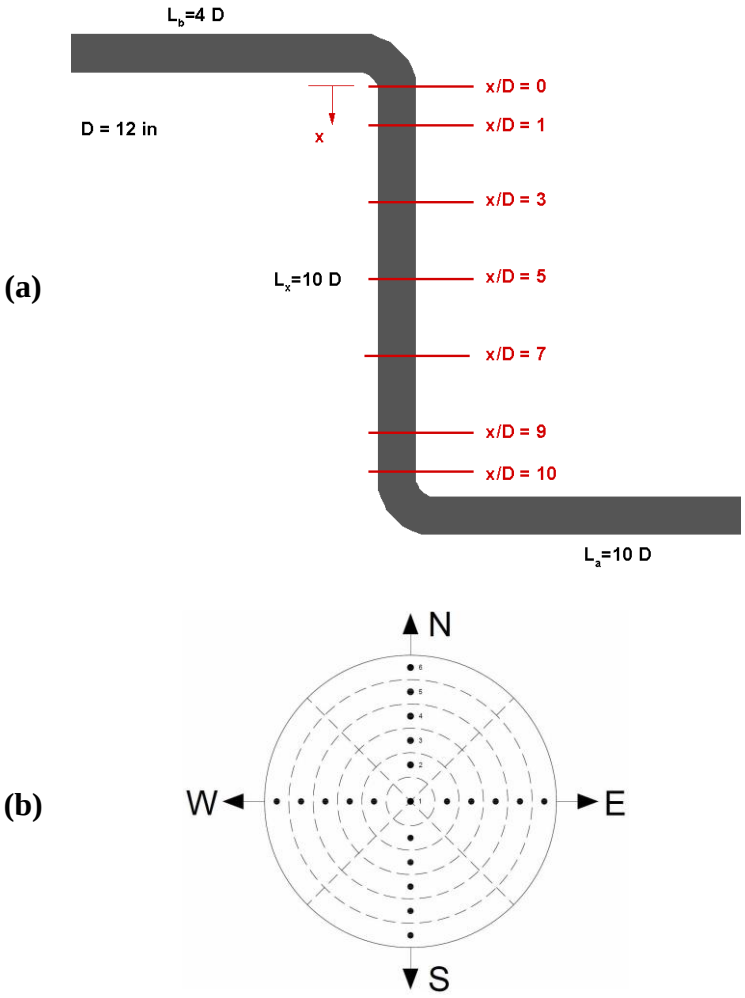

Figure 9. Computational domain of curved ducts.

Table 5. Intermediate Length and Measurement Location for Velocity Profile Test Section

Intermediate Length of the Section (L_{int}/D)	Location for Measurement (x/D)
4.36	1
6.40	1,3
8.36	1,3,5
10.42	1,3,5,7
12.40	1,3,5,7,9

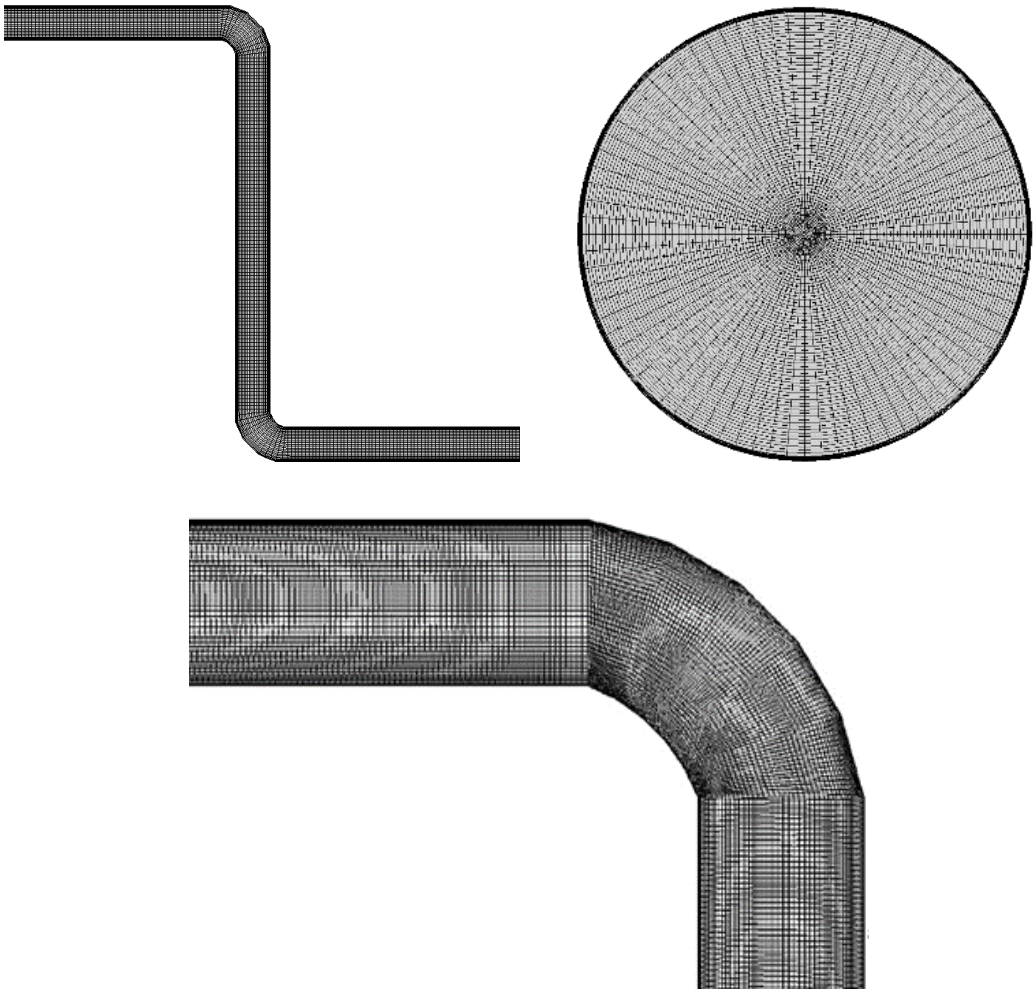

Figure 10. Computational grid of curved ducts.

5.10 Turbulence Modeling Considerations

The simulation of the Z-shaped duct in this study employs four turbulence models: $\zeta - f$ model, RSM, LES, and WMLES. Detailed approach for the turbulence models explained below. These turbulent models are essential for this research as flow swirling behavior due to vortices generation are highly dependent on the modeling framework in the turbulence model itself.

5.10.1 Numerical approach for the $\boldsymbol{\zeta - f}$ model

The ζ-f model is not included in FLUENT ANSYS by default and the UDF script code was applied for the Z-shaped geometry. The C_μ is similar to $\overline{v^2} - f$ model given in [64], [99]. Based on Durbin's realizability constraints, the parameter values are suggested for numerical stability.

To interface the novel turbulence model with the Fluent solver, a UDF script was written and is available in Appendix B. The developed ζ-f model in this research is never examined for the applications of Z-shaped duct configurations. Equations (16) to (23) represent the function of transport equations that include k, ε, $v^2$and f are explained in the UDF script. The Modified Fluent flow variables are modified and defined using DEFINE_ADJUST macro. The macro was executed at every iteration before solving the transport equation.

The source term for every equation is reorganized and defined in the DEFINE_SOURCE function as Table 6. The diffusion coefficient for each UDS is also reorganized and defined in the DEFINE_DIFFUSIVITY function as

Table 7. Diffusion Coefficient of UDSs for the ζ-f Model

k equation	ε equation	ζ equation	f equation
$\mu + \frac{\mu_t}{\sigma_k}$	$\mu + \frac{\mu_t}{\sigma_\epsilon}$	$\mu + \frac{\mu_t}{\sigma_\varsigma}$	1

Table 8. Flux Terms of UDSs for the ζ-f Model

k equation	ε equation	ζ equation	f equation
ρu_j	ρu_j	ρu_j	0

. The flux terms are defined in **Error! Reference source not found.**.

The DEFINE_ADJUST function is a general function to define any other

parameters that have no predefined function in the Fluent. In the present UDF, the time scale *T*, length scale *L*, turbulent viscosity ν_t, strain rate *S*, and user-defined memories (UDMs) are defined in the DEFINE_ADJUST function.

Table 6. Source Terms of UDSs for the ζ-f Model

k equation	ε equation	ζ equation	f equation
$P - \rho\varepsilon$	$\frac{C_{\varepsilon 1} - C_{\varepsilon 2}\rho\varepsilon}{T}$	$\rho f - \frac{\zeta}{k}P$	$-\frac{1}{L^2}\left[f + \frac{1}{T}\left(C_1 - 1 + C_2\frac{P}{\rho\varepsilon}\right)\left(\varsigma - \frac{2}{3}\right)\right]$

Table 7. Diffusion Coefficient of UDSs for the ζ-f Model

k equation	ε equation	ζ equation	f equation
$\mu + \frac{\mu_t}{\sigma_k}$	$\mu + \frac{\mu_t}{\sigma_\epsilon}$	$\mu + \frac{\mu_t}{\sigma_\varsigma}$	1

Table 8. Flux Terms of UDSs for the ζ-f Model

k equation	ε equation	ζ equation	f equation
ρu_j	ρu_j	ρu_j	0

In addition, the following constants are used for this research study.

Table 9. Constants

C_μ	C_{s1}	C_{s2}	c_1	C_2	σ_k	σ_ε	C_ξ	C_ζ	C_L	C_η
0.22	1.4(1+0.012/ζ)	1.9	0.4	0.65	1	1.3	1.2	6.0	0.36	85

5.10.2 Numerical approach for the Reynolds Stress Model

In this section, linear pressure strain model is selected along with the curvature correction and enhanced-wall treatment. Due to the increase in the velocity, kinetic energy is produced that affects the concave wall. The wall functions need to be used to simulate flows approaching the boundary layer region. To reach the required near-wall

region y^+, a different method can be used where near-wall mesh can be further refined. The configuration of every turbulence model is specified in terms of y^+ values. To approximate the velocity profile shapes following equations are used, where y^+ is near-wall region and u_τ is friction velocity.

$$y^+ = \frac{\rho_w u_\tau y}{\mu_w} \tag{41}$$

$$u_\tau = \sqrt{\frac{\tau_w}{\rho_w}} \tag{42}$$

5.10.3 Numerical approach for the Large-Eddy Simulation and Wall Modeled Large-Eddy Simulation models

In this study, to perform the CFD simulations, ANSYS fluent solver was used. The spatial domain was discretized using the finite volume (FVM) method. The discrete counterparts of the pressure equation and momentum equation were done with the help of the standard scheme and with accurate schemes of the second order, respectively. Furthermore, a second-order accurate arrangement was also employed for temporal discretization. To ensure convergence, residuals of the momentum equation were moderated to$< 10^{-4}$, scalar values were restricted to$< 10^{-6}$, and the time-step with the value of 10^{-5} sec was employed for advancing the LES solution.

This study also employed the dynamic Smagorinsky-Lilly sub-grid scale model. At the beginning of the simulation, the number of iterations per time step (Δt) used was exactly 100, which was then gradually reduced to 15 iterations per Δt. The reason for the gradual decrease was to converge the solution at each Δt because of NS

equations. To ensure the numerical solutions is converged, mass flow conservation is monitored by using total mass flow measured at inlet and outlet surfaces.

5.11 Mesh Independent Study

In this section, numerical results obtained by varying the resolution of the mesh to the computational domain are given. The reason for using various mesh resolutions was to ensure the accurate resolution of flow inside the pipe and to sufficiently capture the physics associated with the fluid flow. The near-wall y+ is a non-dimensional criterion to determine whether the flow is resolved well near inside the boundary layer region for the wall-bounded flow. The y+ value was identified as the critical parameter for inflation meshing requirements, as y+ values would determine whether the first cell lies inside the laminar sub-layer or logarithm region.

The optimal mesh resolution is critical as it is used in multiple simulations. Therefore, an independent mesh analysis was used for achieving a rougher converged mesh, to save computational time. If a finer mesh utilized for this purpose, the results would have been like those with the rougher converged mesh. However, that procedure would have been more computationally demanding and more time consuming. The optimal mesh resolution depends on the evaluation of earlier numerical results of rough converged mesh. The final optimal mesh obtained from this process must be suitable to resolve the physics of the flow. Figure 11 shows that in the bending geometry, the mesh is 30% more refined than the bulk mesh region. To keep the value of y^+minimum, the mesh is also refined at the near-wall region.

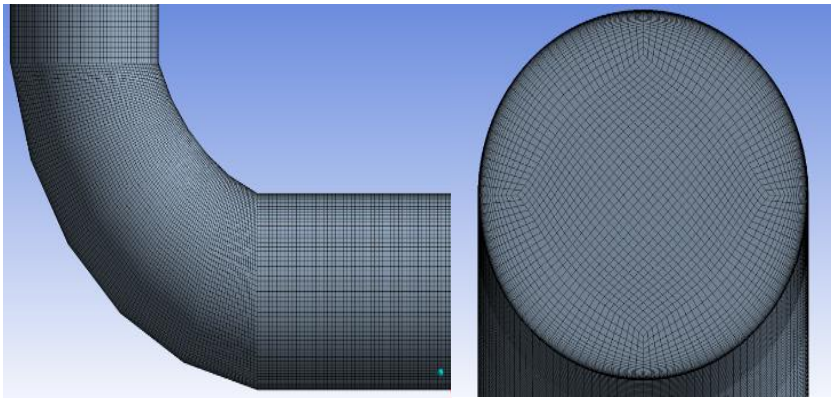

Figure 11. Mesh resolutions for duct wall

5.11.1 Mesh refinement study for LES and WMLES

The convergence analysis of mesh is important, because resolved variables are filtered, which means that the filter is changing for each mesh. Fine mesh together with precise time steps are important for the proper resolution of the eddies using LES. Moreover, the fraction of k directly resolved is determined by mesh resolution. The peak of k is usually observed at the integral length scale l_0. Therefore, resolving this scale in all directions is important for determining an eddy with a certain length scale $\Delta = {}^{l}/_{2}$. This study aims to resolve 80% of k, which means that eddies with a larger size than half the size of l_0 need to be resolved. For this purpose, 5-cells were located across l_0 and contours with the ratio $10/\Delta$ were plotted. To identify the regions that are not so well resolved, the upper values of $10/\Delta$ were removed. In addition, the regions closer to the elbow that are under-resolved were re-meshed.

To resolve the smaller eddies in LES, the wall-normal as well as wall-parallel spacing was reduced. By reducing the spacing, the grid points density increases in all

directions while moving toward the wall. For this reason, LES wall functions were considered here, and the mesh resolution at near wall was taken as 10. SGS WALE model was implemented to achieve accurate levels of SGS viscosity.

5.11.2 Mesh refinement study for Reynolds stress and ζ-f models

For all cases, the range of y+ lie between 0.6 and 1. At section $x/D = 5$, the results of turbulent kinetic energy (k) were examined at the duct centerline $x/D = 0$. Table 10 demonstrates the results of the examined turbulent kinetic energy (k) for different grid sizes. Here, the medium mesh was adopted instead of the fine mesh because the acceptable tolerance for turbulent kinetic energy (k) falls in the (±2%) range, and because the number of individual cells in the medium mesh was smaller than 2.1×10^6, hence, it requires less computational time.

Table 10. Results for Independent Mesh Analysis

Mesh	The approximate number of cells ($\times 10^6$)	TKE (k) $(m/s)^2$
Coarse	1.4	2.281
Medium	2.1	3.695
Fine	4.2	3.715

CHAPTER 6: RESULTS AND DISCUSSIONS

6.1 ζ-f and RSM Model Results for Turbulence Modeling

In this section, the validation of LES prediction is presented and evaluated against the experimental data. The distribution of mean flow velocity is given in Figure 12 to Figure 16. To represent the normalized mean flow, for each section, the local mean velocity is normalized at the centre. The locations are represented by normalized radial locations, with 0 representing the centre of the section and 1 representing the inner wall of the duct. For each profile, at each section, the ES (East-West) and NS (North-South) direction lines are used. As mentioned in earlier sections, in a Z-shaped duct, five cross-sections are used for numerical analysis: x/D=1, 3, 5, 7, and 9.

Section x/D=1 corresponds to the section after the first elbow. According to fluid mechanics principles, when the flow makes its first turn, because of local flow separation, the distribution of flow velocity is highly non-uniform. For this reason, the flow pattern is asymmetric in the EW direction. Outward (negative) radial locations showed higher velocity whereas inner (positive) radial location showed lower velocities. The velocity of mean flow decreases because of flow separation and increases because of flow reattachment.

Figure 12 shows the outcomes of the velocity profiles compared to experiment. Figure 12 (a) shows the profile in the EW direction and Figure 12 (b) shows the profile in the NS direction. In this section at x/D=1, both the velocity profiles behave differently can be explained by the presence of Dean vortices. The Dean vortices push the flow from East towards the West or outer radial wall leads to asymmetrical velocity profile about r/D=0 location. This phenomenon is originated from flow experiencing large centrifugal force when turning around the elbow. Such Dean vortices is essentially a pair of counter-rotating vortices and therefore each individual secondary vortex show

symmetrical pattern in N-S direction.

Both Figure 12 (a) and (b) have shown ζ-f model predicts better than RSM. Figure 12 (a) shows that the RSM predicted values were slightly under-predicted in the flow separation region at r/D near 0 to 1. For example the velocity ratio is around 0.6 at r/D=0.5 location based on experimental measurement whereas the RSM predicted flow velocity ratio is 0.4 at the same location. It is expected the swirling dominates in this flow separation region and the RSM failed to accurately capture the turbulent length scale and eddy viscosity. For the reattachment region from r/D=-1 to 2, both RSM and ζ-f predictions are found to be in good agreement with experiment. Figure 12 (b) shows that the results for NS direction velocity profiles from both ζ-f and RSM models were consistent with experimental data.

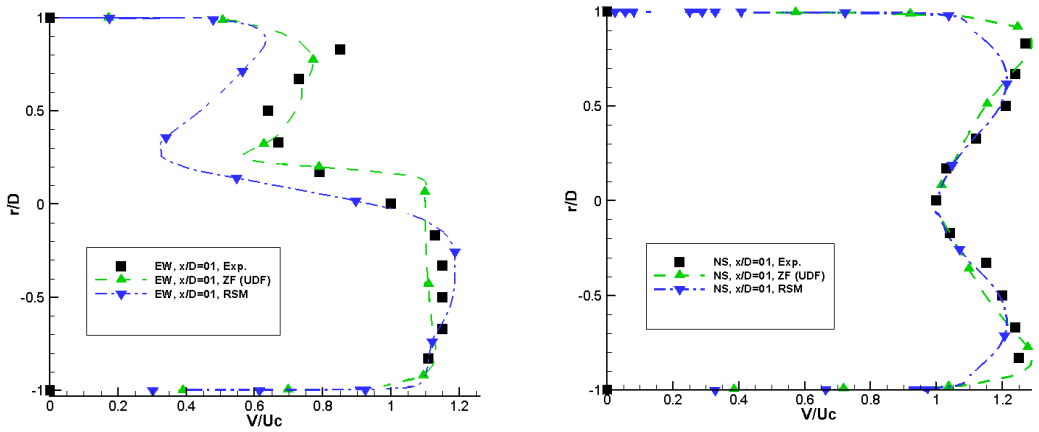

(a) (b)

Figure 12. Velocity profiles (normalized) for RSM and ζ-f models at section x/D=1: (a) E-W (East-West) orientation (b) N-S (North-South) orientation

In the straight pipe section, the flow is in transition from a non-uniform to a uniform pattern. The duct sections discussed are analyzed for different locations x/D=3, 5, and 7 on the straight pipe.

Normalized velocity profiles at section x/D=3 are given in Figure 13. Figure 13 (a) shows the E-W results predicted by ζ-f model are consistent with experimental data.

RSM results are better in the inboard wall and over-predicts at the outboard wall. For example, at r/D=-0.7, experimental velocity ratio is 1.37 whereas RSM predicts 1.45 at the location. Figure 13 (b) shows the velocity profiles in N-S direction predicted by ζ-f model are in better agreement to experiment compared to RSM model.

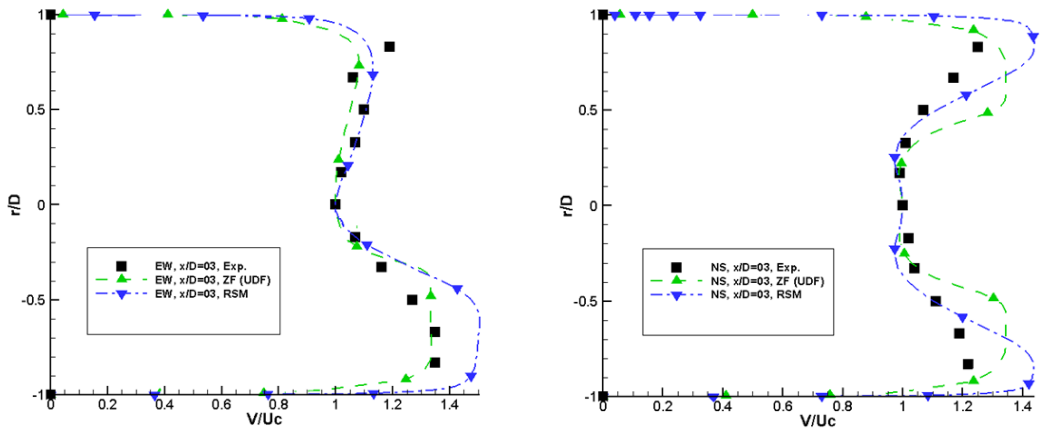

(a) (b)

Figure 13. Velocity profiles (normalized) for RSM and ζ-f models at section x/D=3: (a) E-W (East-West) orientation (b) N-S (North-South) orientation

Normalized velocity profiles for both directions at section x/D=5 are shown in Figure 14. That is: $EW\ (z)$ and $NS\ (y)$. The figure shows that the flow physics captured by ζ-f and RSM is satisfactory.

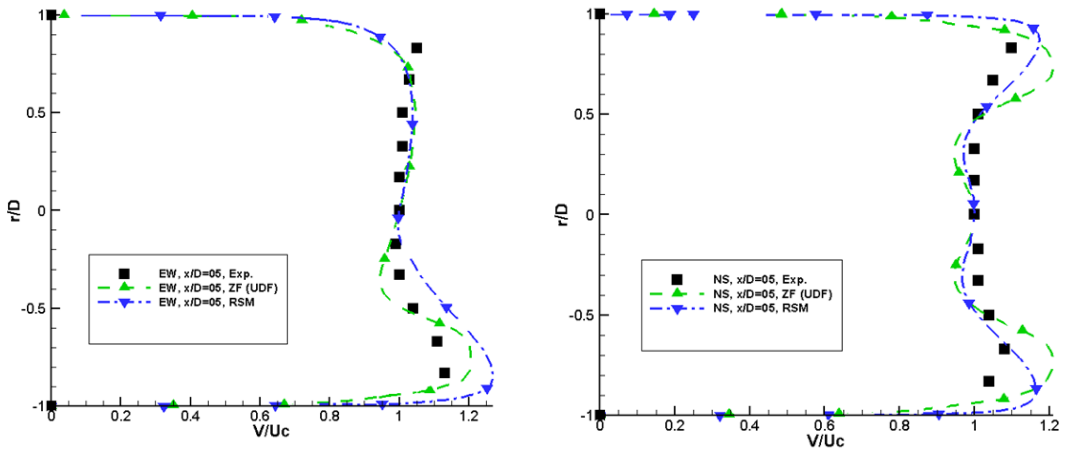

(a) (b)

Figure 14. Velocity profiles (normalized) for RSM and ζ-f models at section. $^{x}/_{D} = 5$: (a) E-W (East-West) orientation (b) N-S (North-South) orientation

Downstream in the straight pipe section, velocity profiles become highly uniform. This can be attributed to the fully turbulent flow development. The results related to section x/D=7 are presented in Figure 15. Figure 15 (a) shows that at an inner radial location, the prediction of both turbulent models is closer to experimental results. However, that is not the case for outer radial location, where the ζ-f model slightly under-predicted the local flow velocity while RSM slightly over-predicted the profiles at the same location. Figure 15 (b) shows that ζ-f model consistently over-predicted velocity profiles while RSM results are inconsistent manner indicating some over-preditions and some under-predictions.

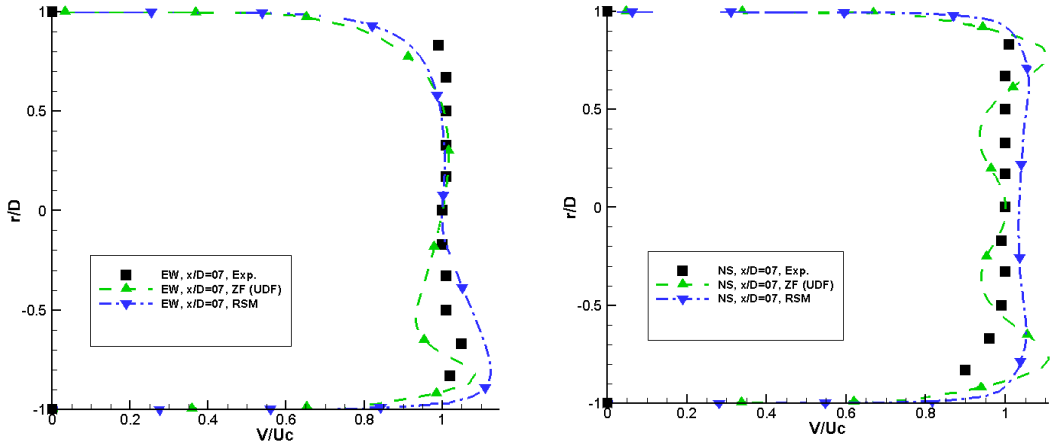

(a) (b)

Figure 15. Velocity profiles (normalized) for RSM and ζ-f models at section. $^{x}/_{D} = 7$: (a) E-W (East-West) orientation (b) N-S (North-South) orientation

Figure 16 shows outcomes for normalized mean flow velocity profiles for section x/D=9. Here, for outer radial location (r/D=-0.2 to 0.99), the RSM results constantly over-predicted in both EW and NS directions, whereas the ζ-f model results are relatively more accurate. The over-predicted results can be attributed to the mathematical errors that occurred during resolving upstream flow structures.

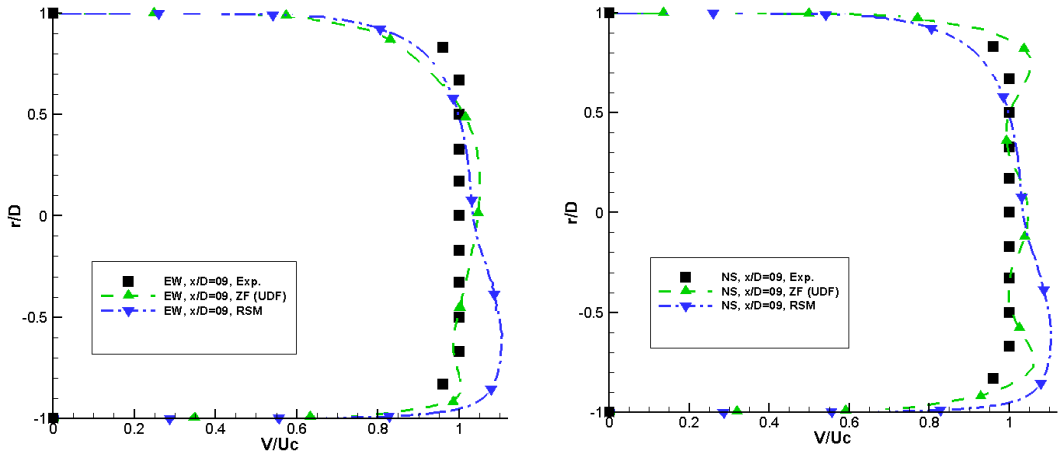

(a) (b)

Figure 16. Mean x velocity results of the experiment and studied turbulence models (i.e., ζ-f and RSM) at $^{x}/_{D} = 9$: (a) E-W (East-West) orientation (b) N-S (North-South) orientation

The mean velocity contours are at different x/D fluid planes are created as shown in Figure 17. The velocity vectors are added to demonstrate the flow directivity. At x/D=0, adverse pressure gradients are clearly seen to form near the wall leads to local flow circulation bubble as indicated in blue. Further downstream near after first elbow bend at x/D=1, Dean vortices are formed as results of deflection of high-speed upstream flow experience centrifugal force. The Dean vortices is a pair of counter-rotating vortices behaves in unstable manner as shown in Figure 17. The ζ-f model is able to capture the swirling of such Dean vortices structures. The size of Dean vortices can be identified from the contour at x/D=3 as it shows the vortices are diminishing with velocity recovery. At x/D=5, the vortices are disappeared, and velocity vector becomes weak in radial direction as flow is now dominated by axial component indicating flow is moving downstream along the pipe. These uniform patterns sustain until flow reaches fluid plane at x/D=10. At x/D=10, flow experiences adverse pressure gradients near the pipe wall. It is expecting that such adverse pressure is responsible for inducing flow separation and swirling near second elbow.

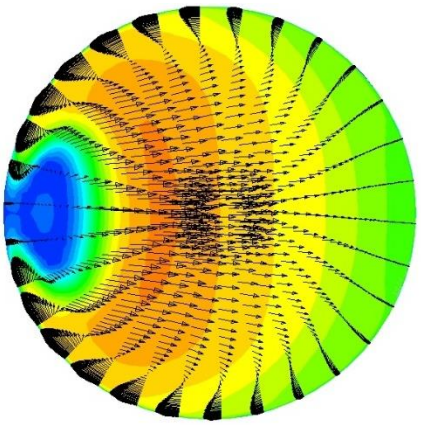

x/D=0

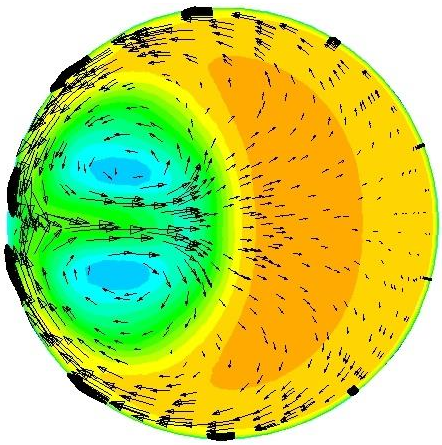

x/D=1

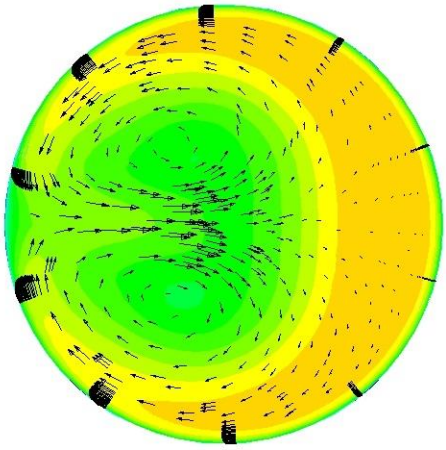

x/D=3

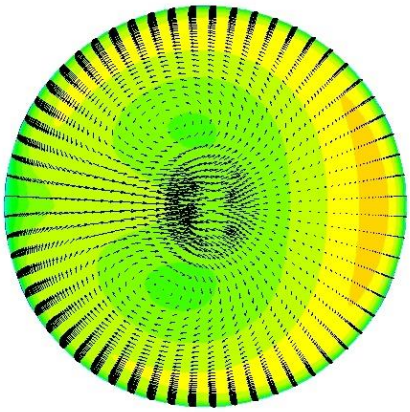

x/D=5

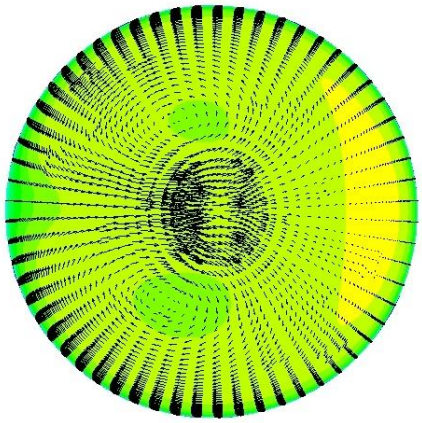

x/D=7

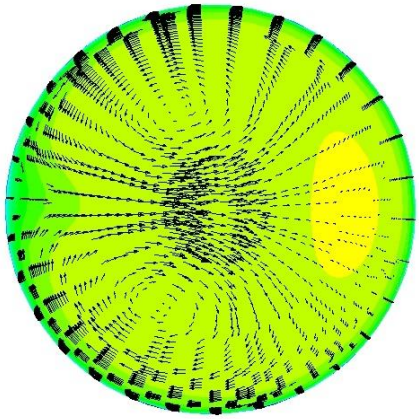

x/D=9

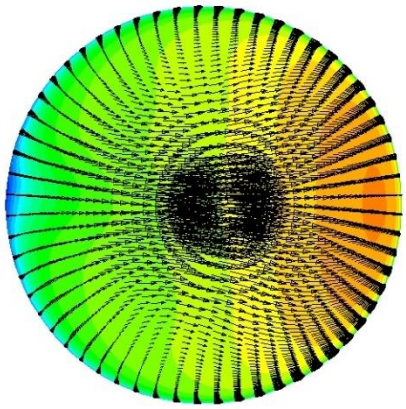

x/D=10

Figure 17. Mean velocity contour at different x/D fluid planes based on ζ-f model

In a nutshell, both ζ-f as well as RSM turbulence models together with steady-state RANS solution exhibited realistic outcomes. Both the models displayed accuracy in handling turbulence flow related structures. The ζ-f model shows superior behavior in terms of computational efficiency. The attributes of the ζ-f model related to efficiency and accuracy have made this model widely used in dealing with wall-bounded turbulent flow issues. Predictions linked to the slow separation region and the reattachment region are studied thoroughly along with the flow mixing regions. Results confirm that the ζ-f model can yield a more accurate result. Flow separation bubble size and the length of reattachment are both estimated quite accurately. Also, the average flow velocity distribution is on the same line in NS and EW directions. The crucial flow mechanism, which plays a central part in guiding downstream flow development, is the vortex shedding in the flow separation region along with the geometries of bending elbow. Turbulent eddy dissipation downstream along with the structures that contribute to flow mixing creates complicated flow mechanisms that exhibit highly non-homogeneous and non-isotropic characteristics. The ζ-f model, which is currently used in the present research study, was not tested for the Z-shaped pipe before this study. Hence, this study can pave the way for further implementation of the ζ-f model.

RSM predictions exhibited improved accuracy but showed some inconsistencies in the results. This is because the RSM model is proficient only at the inner side of the boundary and exhibits higher diffusion in the wall-bound region.

6.2 Turbulence Modeling Results Using the LES Model

In this section, various duct lateral separation distances L/D are found to be correct when the values are L/D=2, 4, 6, 8, 10. The number of fluid sectional planes is changed in accordance with various L/D values in each configuration. As an example, the longest configuration with L/D=10 had five sections and that leads to x/D=1, 3, 5,

7, 9. However, the velocity profile data is not accessible at different section simultaneously and is accessible at a single section only when L/D=2 (smallest configuration). The section before the first 90° elbow turn is termed as "inlet." Similarly, "outlet" is the section after the second 90° elbow turn. In detail analyses of all these sections are presented below with various L/D values. Figure 18 to Figure 20 will discuss results based on $Re=2.4x10^5$ for L/D=8 configuration. Figure 21-Figure 27 will discuss mean velocity results based on higher Reynolds number at $3.5x10^5$ at different L/D configurations. Another study of higher Reynolds number at 4.5 $x10^5$ for L/D= 4 configuration shown in Figure 28 and Figure 29.

6.2.1 $Re=2.4x10^5$

Section x/D=1: After First Elbow:

Figure 18 shows the velocity profile at x/D=inlet for at L/D=4 configuration at $Re=2.4x10^5$. The corresponding inlet velocity is 9 m/s. The predicted LES velocity exhibits fully developed turbulent flow with sharp velocity gradients developed from the wall which represents the boundary layer. Outside the boundary layer, the velocity is uniform in along E-W and N-S directions.

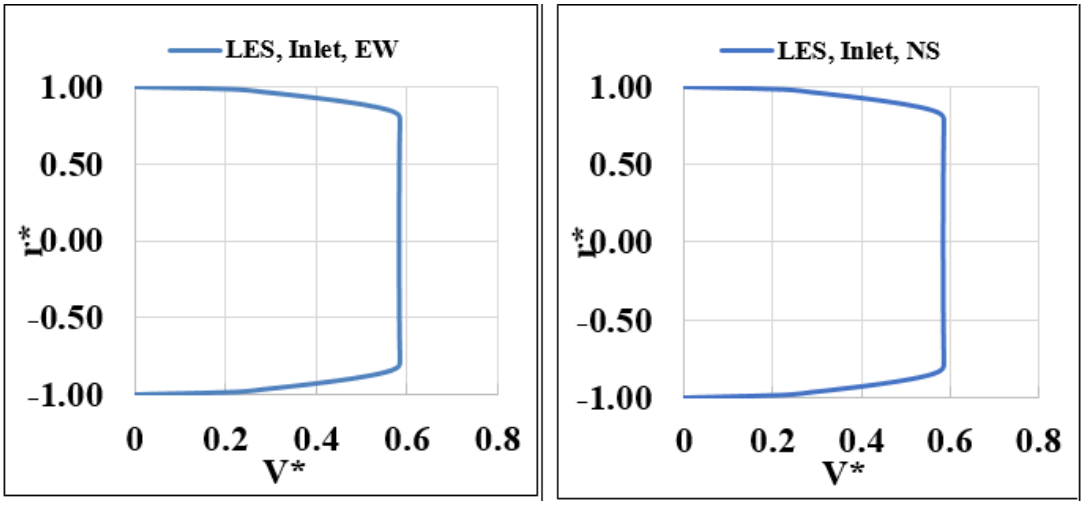

(a) (b)

Figure 18. Velocity profiles (mean flow) at x/D=inlet for L/D=4 configuration at Re=2.4x10^5: (a) E-W (East-West) orientation (b) N-S (North-South) orientation.

$x/D = 1$ *Section: After First Elbow:*

Figure 19 shows the velocity profile at x/D=1 for L/D=4 configuration at Re=2.4e^5. The flow experience large centrifugal force when turning around elbow leads to flow being deflected towards West direction. Therefore, Figure 19 (a) shows asymmetrical pattern indicating Dean vortices formation. Dean vortices is a pair of counter-rotating vortices creates local swirling effect results of momentum deficit near inner radial location. Such phenomena are successfully captured by current LES simulation. Figure 19 (b) shows the N-S direction profile across the symmetrical Dean vortices structures. Therefore, the profile appears to be much more symmetrical than E-W direction.

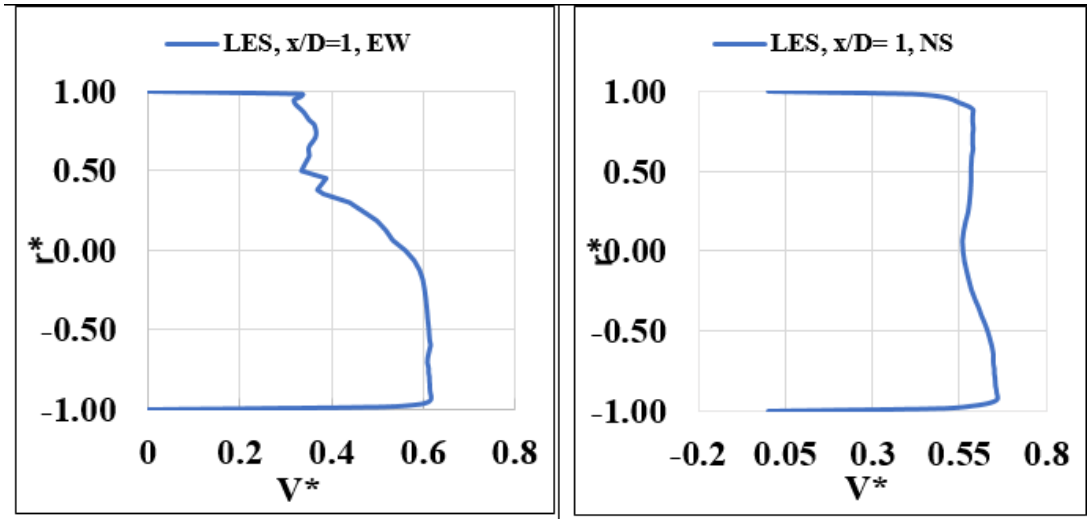

(a) (b)

Figure 19. Velocity profiles (mean flow) at x/D=1 for all L/D configurations at Re=2.4x10^5. (a) E-W (East-West) orientation (b) N-S (North-South) orientation.

$x/D = 3$ *Section: In between Elbows:*

Figure 20 shows the velocity profile at x/D=3 for L/D=4 configuration at Re=2.4e^5. The E-W profile consistently demonstrates similar asymmetrical distribution predicted by LES on both sides of the duct walls. The result indicate Dean vortices remain at x/D=3 location. The flow velocity distribution on N-S direction also shown less symmetrical due to some flow structures re-attachment occurs on the inner radial wall represented by the increased velocity ratio locally.

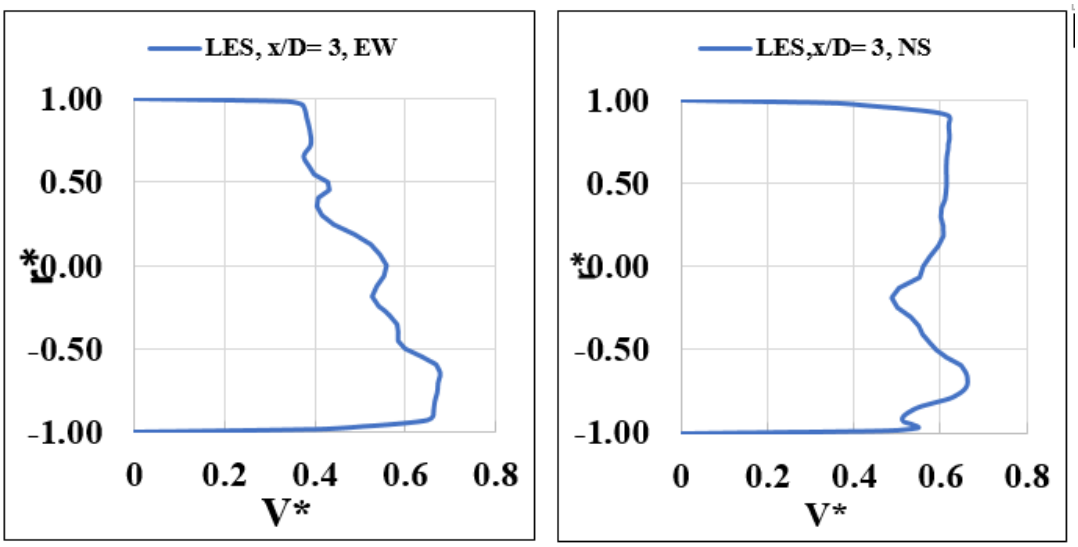

(a) (b)

Figure 20. Velocity profiles (mean flow) at x/D=3 for all L/D configurations at Re=2.4x10^5. (a) E-W (East-West) orientation (b) N-S (North-South) orientation.

6.2.2 Re=3.5x10^5

"inlet" Section:

The first section analyzed inside the duct is the "inlet" section. Such an "inlet" section signifies the plane prior to the first elbow transition. It is expected that the sectional velocity distributions exhibit a completely developed flow profile as in experimental conditions. It is worthwhile to note that all the duct entrance lengths used in the geometries are identical, although they differ in the L/D ratio. In general, both experimental and LES results show fully developed flow profile behavior as shown in Figure 21 below.

The estimated mean LES flow velocity values at "inlet" sections closer to the center of duct are within 2% of the experimental values (remarkable results). Similarly, the estimated values directed towards the near-wall region are within 3% of the experimental values. Hence, it can be said that the current LES method can resolve the

near-center bulk flow structures in an outstanding manner. The only issue is the slight overshoot of the predicted values in a thin region between bulk flow and flow boundary layer. However, these small variations can be due to less precise methods for investigating differently sized eddy structures within the present model.

	EW	NS
L/D=2	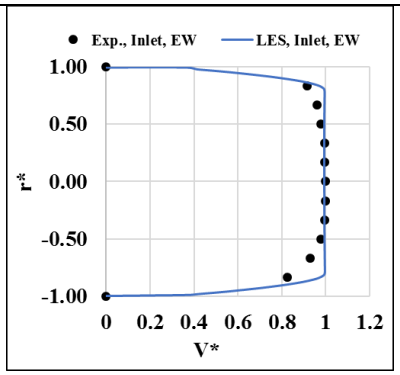	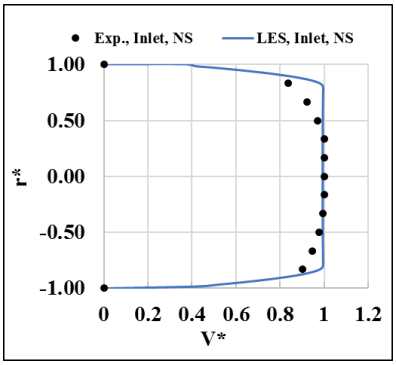
L/D=4	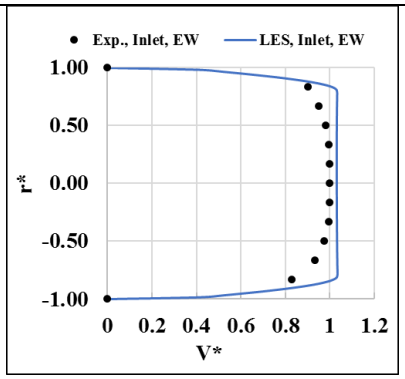	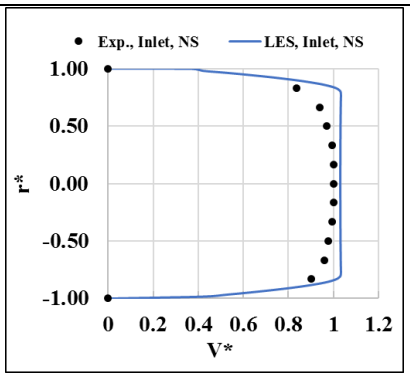
L/D=6	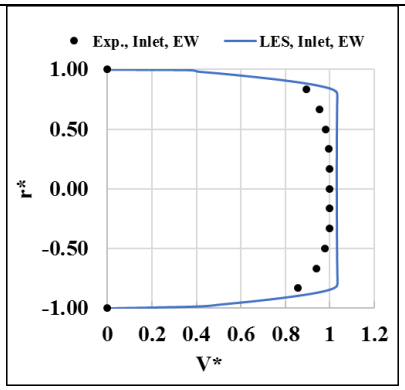	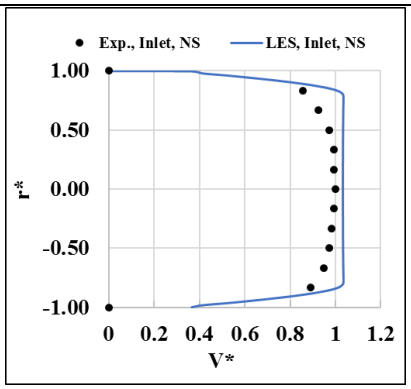

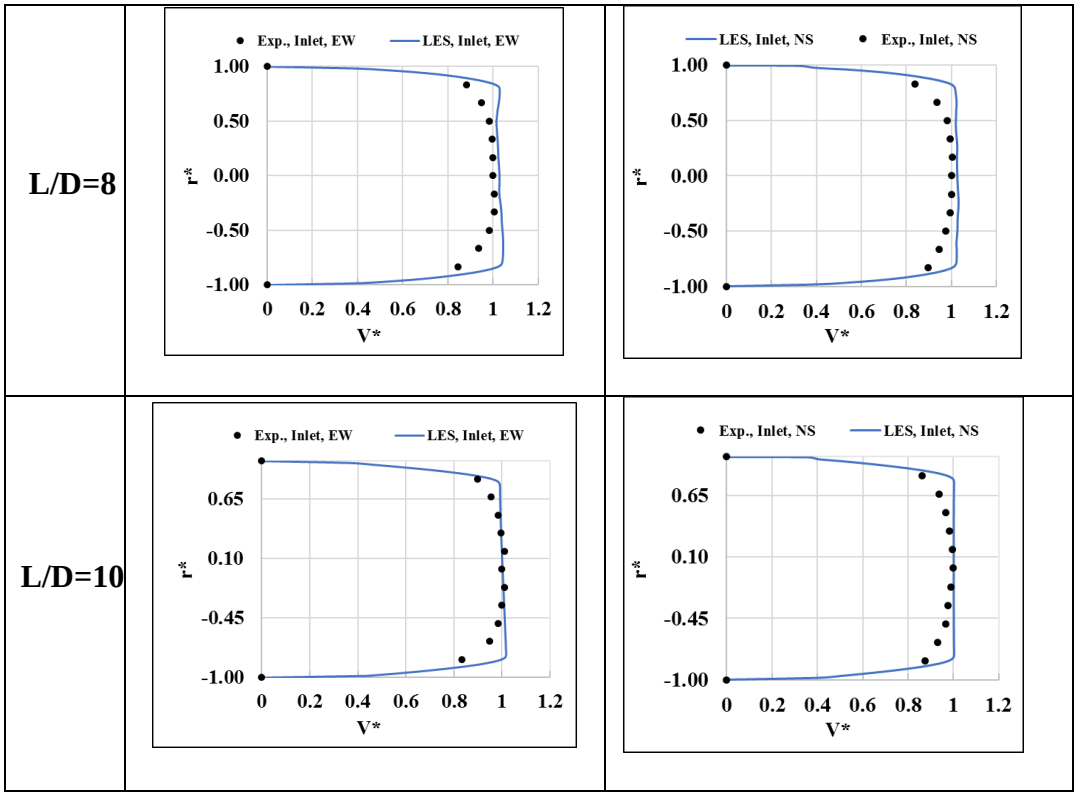

Figure 21. Velocity Profiles (mean flow) at x/D="inlet" for all L/D configurations at Re=3.5x10^5.

$x/D = 1$ *Section: After First Elbow:*

The fluid plane after the first elbow is represented by $x/D = 1$. The presence of reattachment and local flow separation regions when the flow makes the first turn at the elbow is predicted to make the flow velocity distributions highly non-uniform. As indicated in Figure 22 below, the flow pattern in the EW direction is highly asymmetric. Outward (negative) radial locations showed higher velocity in the region whereas inner (positive) radial location showed lower velocities. All L/D configurations exhibited similar patterns. It was also observed that the local reduction in the mean velocity of the flow happened within the separation region. Conversely, the increase of velocity happened inside the flow reattachment region.

Notably, all profiles for L/D configurations exhibited a similar pattern, regardless of the geometries are different L/D dimensions. After the first elbow distribution, the flow structures are supposed to be largely dominated by the turning

radius of the elbow. As the turning radius is similar for all L/D configurations, the velocity distributions are expected to remain unchanged. The overall trend shows that the LES predictions, for all L/D configurations, are quite like the experimental data with slight underpredictions of local separation regions. Moreover, the LES predictions for flow reattachment are found closer to $r^* = 0.2 - 0.99$, whereas for the experimental data, it is near $r^* = 0.18 - 0.9$. Conversely, the flow separation region shown by the lower velocity is near $r^* = -0.3 - 0$. The transition region between flow separation and reattachment is also captured by LES consistently at a location where $r^* = -0.4\ to - 0.8$.

For NS profiles, the flow distribution resembles that of the inlet section. However, near the duct center, the flow velocities are significantly lower. That can be attributed to the loss of flow momentum. The overall trend shows that the LES predictions, for all L/D configurations, are very similar to the experimental results with slight under-prediction near flow separation regions. Decreased velocities are a result of the swirling effect which moves in the circumferential direction.

A significantly finer mesh is required to resolve the smaller eddy structures and that the current mesh employed in the setup is insufficient to fully model all flow scales.

	EW	NS
L/D=2	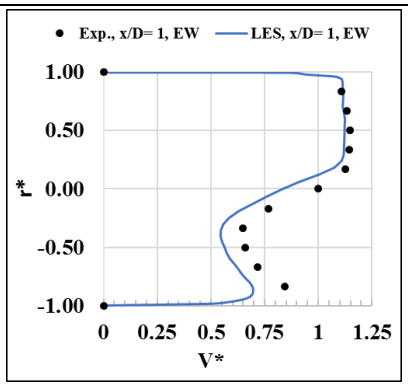	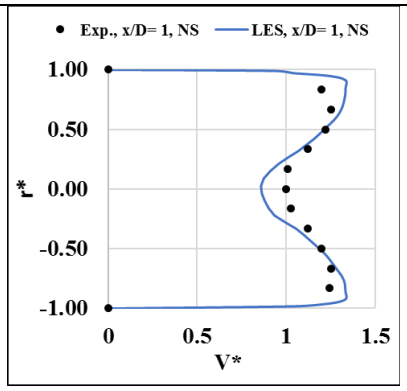
L/D=4	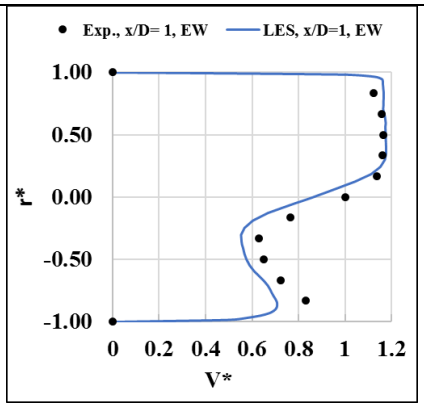	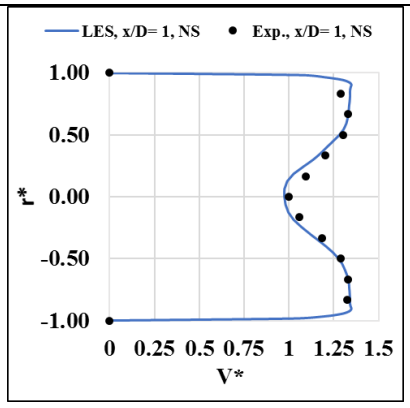
L/D=6	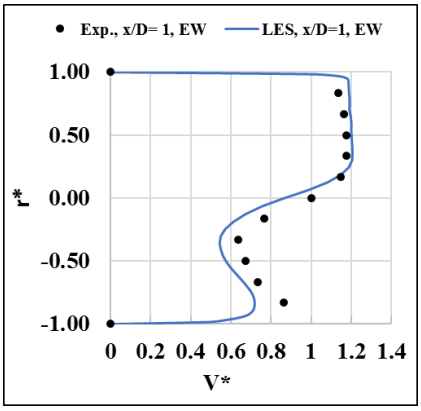	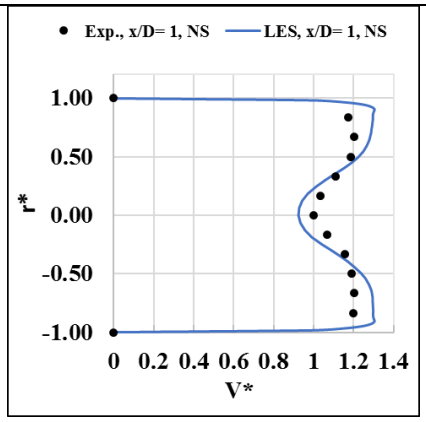
L/D=8	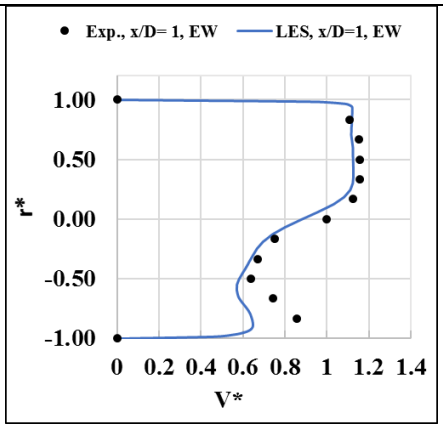	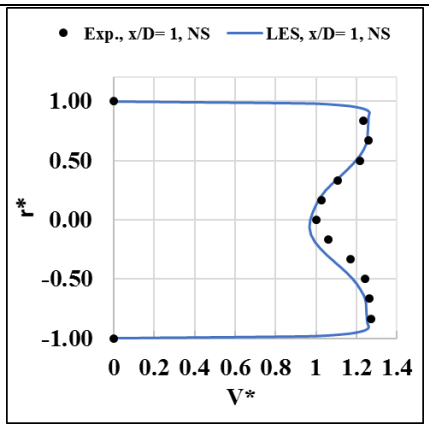

L/D=10	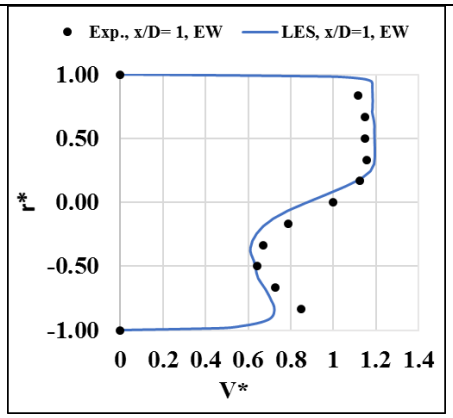	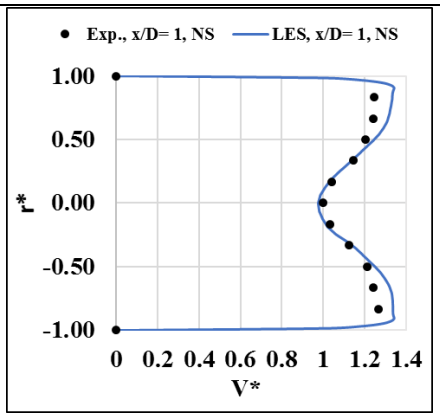

Figure 22. Velocity Profiles (mean flow) at x/D=1 for all L/D configurations at Re=3.5x10^5.

$x/D = 3$ and $x/D = 5$ Sections: Upstream In between Elbows:

When flow is transported along the straight pipe section, it is expected that flow distribution will transition from asymmetrical velocity profiles from upstream that are non-uniform in appearance toward more uniform patterns downstream. The following sections are analyzed at four different locations at $x/D = 3, 5, 7\ and\ 9$ for different L/D configurations.

	EW	**NS**
L/D=4	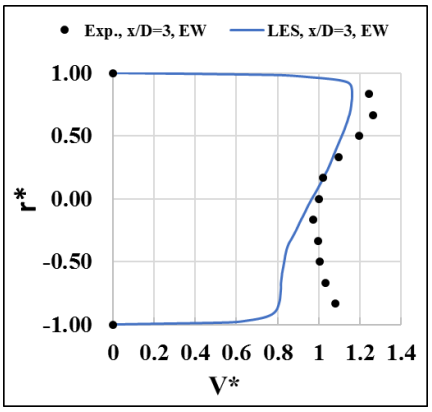	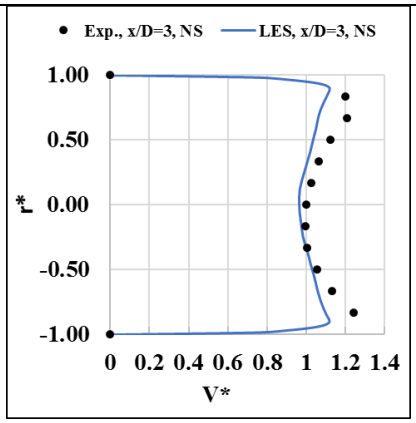

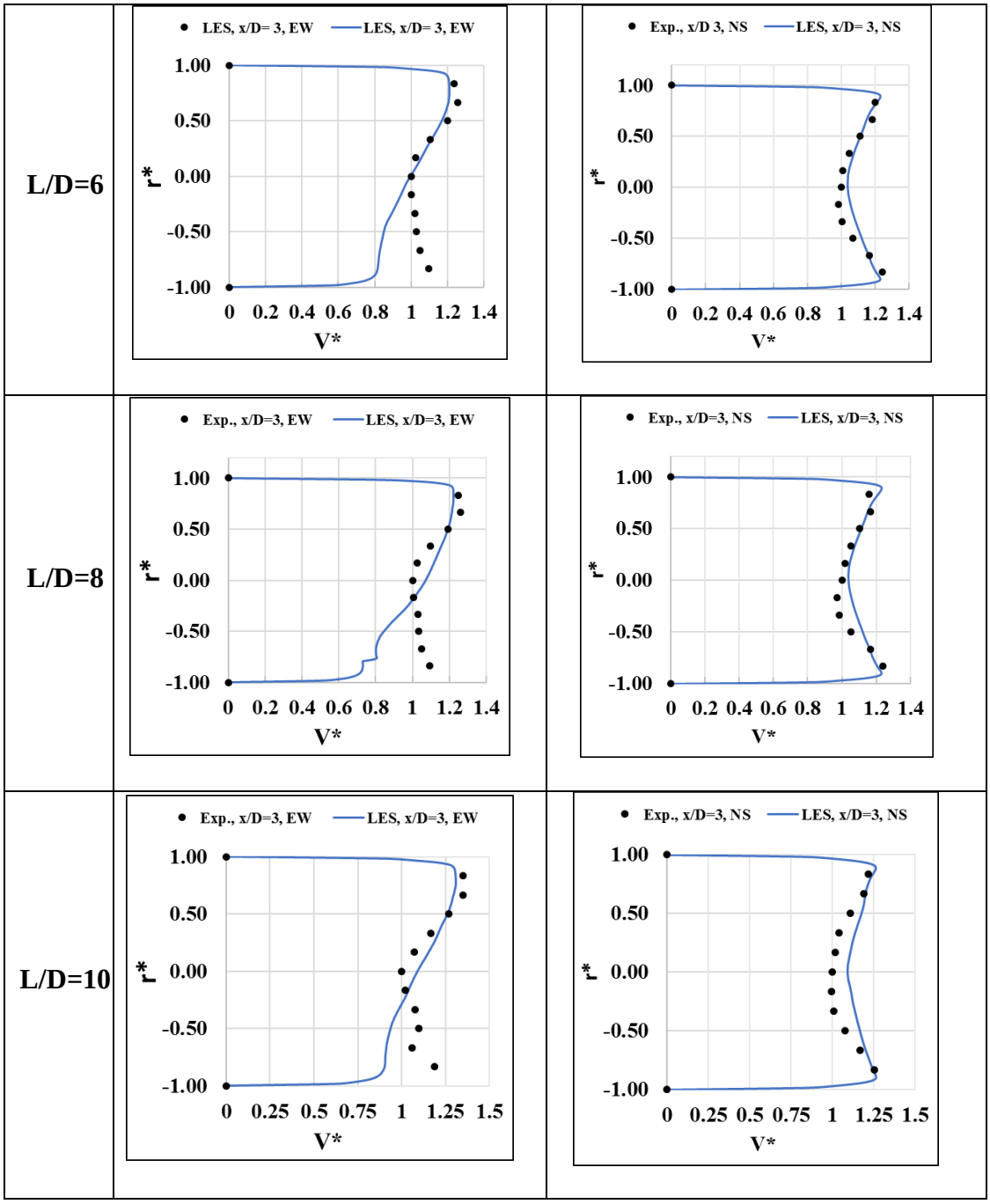

Figure 23. Velocity Profiles (mean flow) at x/D=3 for all L/D configurations at Re=3.5x10^5.

Figure 23 and Figure 24 shows normalized velocity results for $x/D = 3$ and $x/D = 5$, where $L/D > 4$. For all L/D configurations, the mean flow velocity distribution did not completely improve at the upstream flow separation. That fact can also be inferred from the deficit of local flow velocity closer to the value of $r^* = -0.8$

to 0. The experimental flow distributions at $x/D = 5$ are more symmetrical than flow distributions at$x/D = 3$. This is due to flow transition further downstream at$x/D = 5$, from a non-uniform to a uniform trend. As flow moves farther toward downstream of the pipe, the flow structures are anticipated to move closer to the wall again. As mentioned above, the experimental results showed local flow deficit; this deficit is also predicted by the LES in the same region. However, the current LES model underpredicts the results, and fails to accurately capture flow transitions. Similarly, at $x/D = 3$, more errors are found, as errors in upstream flow extend.

For NS profiles, the flow distribution like the ones in $x/D = 1$. From Figure 23 and Figure 24, a peak can be observed between the wall and the pipe center. This peak is ascribed to the swirling effect in the flow. Similar results were found for LES and the experiments, where LES predictions are very close to the experimental distributions.

	EW	NS
L/D=6	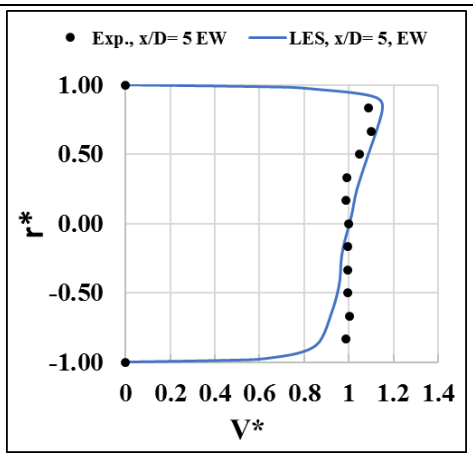	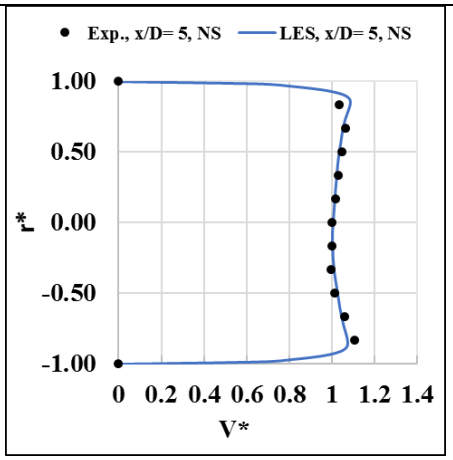

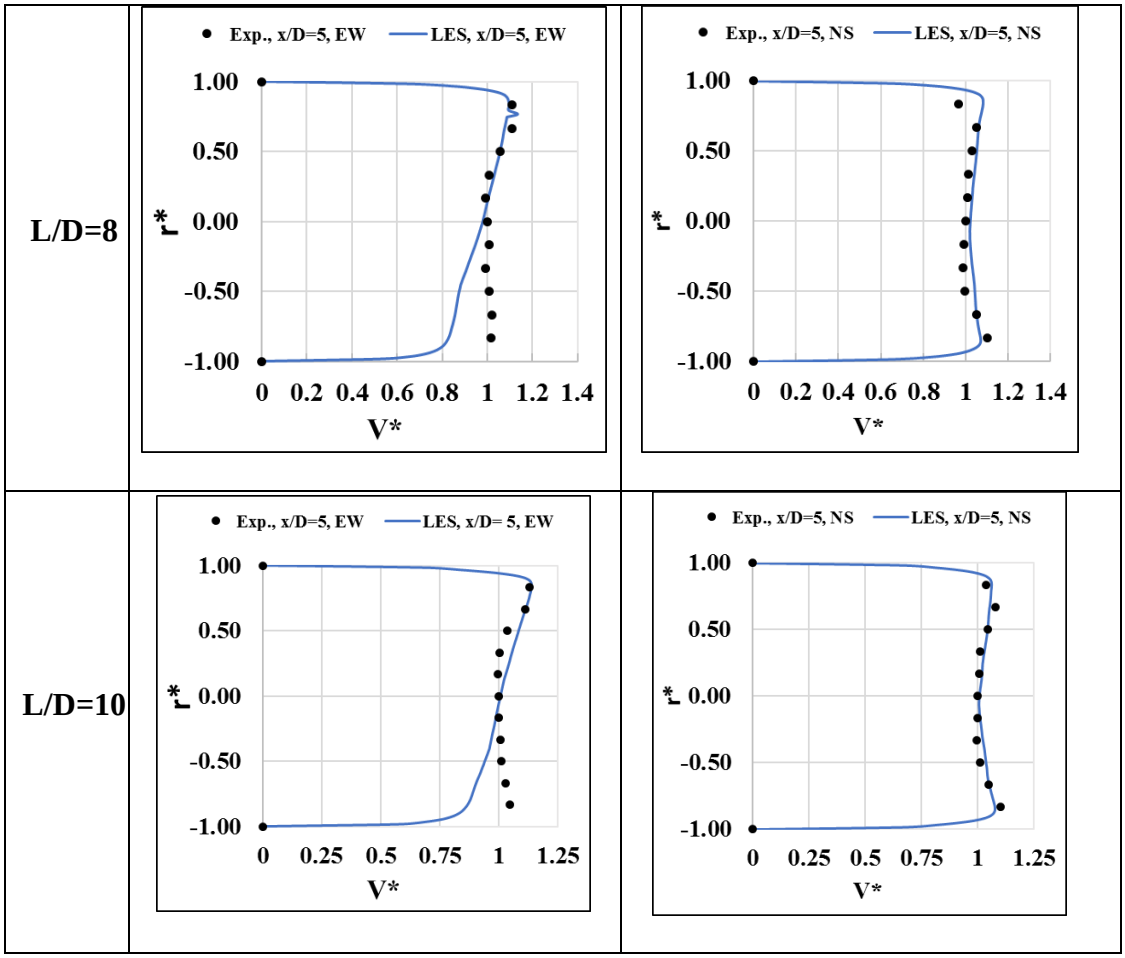

Figure 24. Velocity Profiles (mean flow) at x/D=5 for all L/D configurations at Re=3.5x10^5.

$x/D = 7$ and $x/D = 9$ Sections:

In the straight pipe, sections $x/D = 7$ and $x/D = 9$ are examined further downstream, as shown in Figure 25and

Figure 26. Section $x/D = 9$ is before the second elbow. Furthest downstream, for both sectional planes, the flow velocity is observed to be more uniform. Slightly more upstream, the turbulent flow is expected to be developed completely, which explains the uniformity in results. Similar results were observed regularly for all L/D configurations. The results of both LES estimates and the experiments agree for EW and NS directions. Notably, some inconsistencies and over-predictions were found for

EW profiles, probably due to errors generated further upstream. All things considered, the current comparison study, as indicated by *NS* profile, demonstrates that the LES methodology sufficiently resolves the flow structure on a large scale.

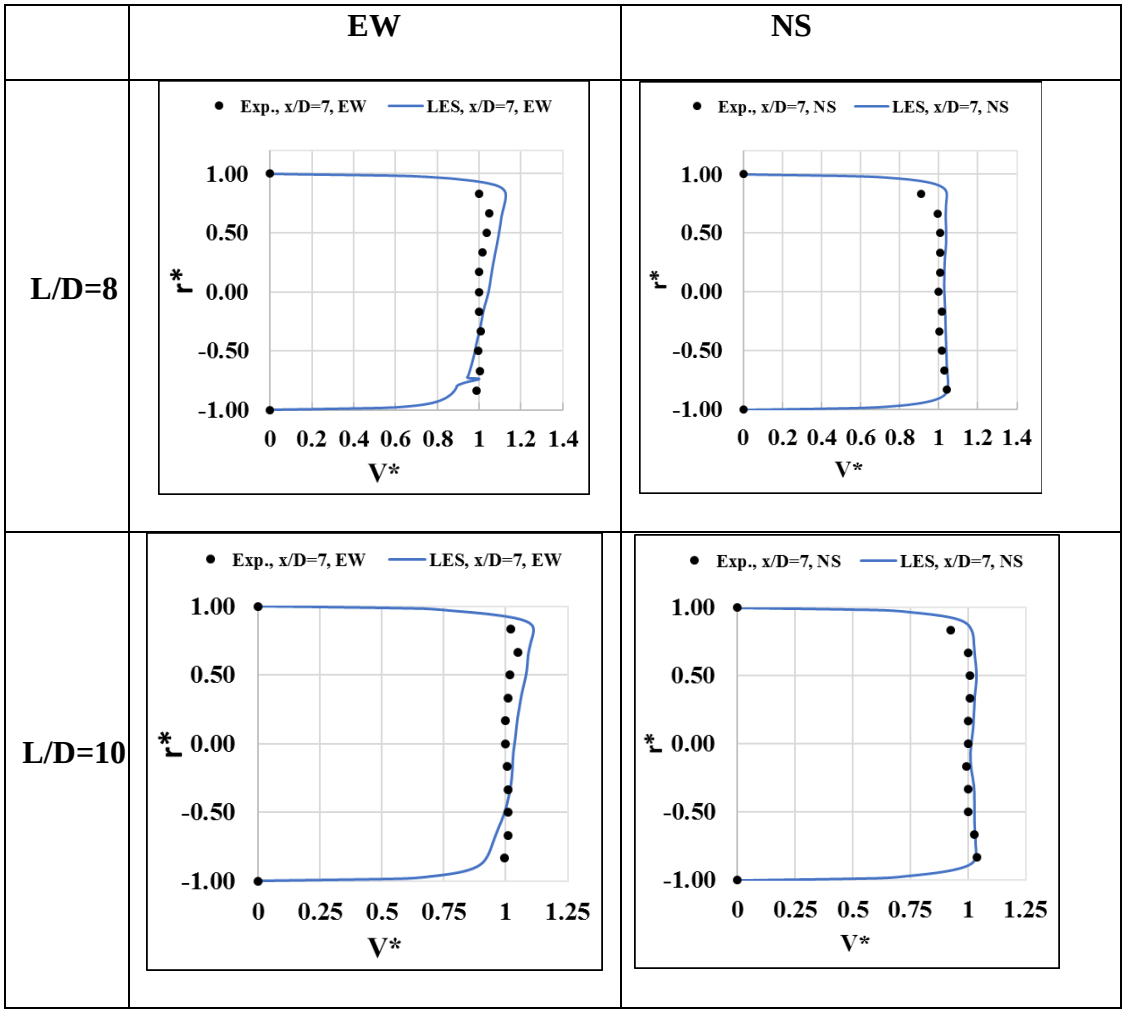

Figure 25. Velocity Profiles (mean flow) at x/D=7 for all L/D configurations at Re=3.5x10^5.

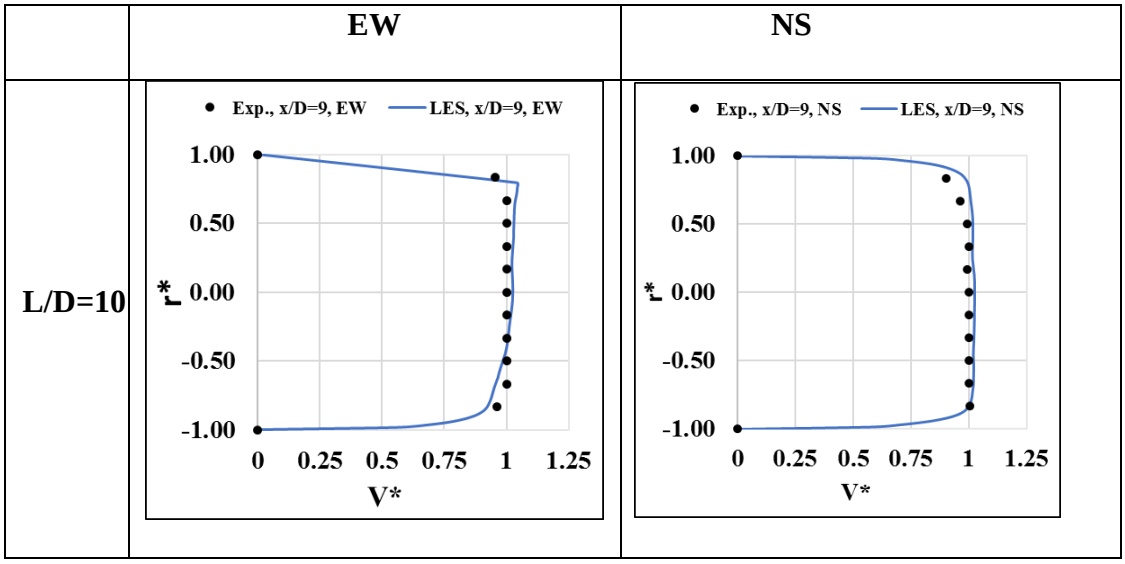

Figure 26. Velocity Profiles (mean flow) at x/D=9 for at L/D=10 configurations at Re=3.5x10^5.

"Outlet" Section:

This sectional plane is located after the 90° elbow location. At this section, the flow velocity distributions show that negative radial locations have higher velocities in this region, whereas positive radial location have lower velocities. Lower velocities are ascribed to the existence a separation region in local flow near r*=0.2-0.9. All L/D configurations exhibited similar patterns. The results of both LES estimates and the experiments agree for EW and NS directions. The results for $L/D = 10$ are found to be most satisfactory, whereas $L/D = 8$ results are the least satisfactory. For both LES estimates and experimental results, the local flow separation is found closer to $r^* = 0.2 - 0.9$. Local flow separation at this point is predictable, as the flow is turning at 90°, as the swirling effect produces a local flow circulation.

Conversely, NS profile is also confirmed in Figure 27 where the results of LES estimates and the experiments agree. It is worthwhile to note that the NS profile at the "outlet" section has also shown a similar distribution as the "inlet" section, indicating

flow is partially recovered to a completely developed flow profile in the direction of the outlet.

	EW	NS
L/D=2	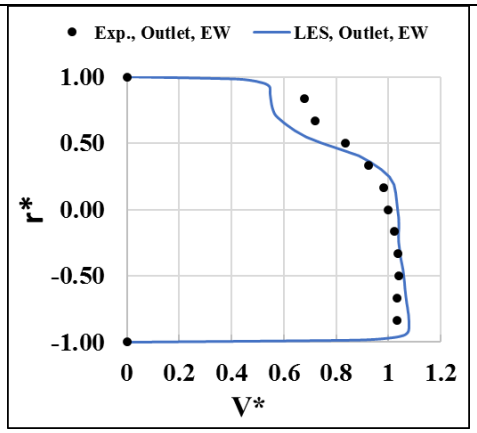	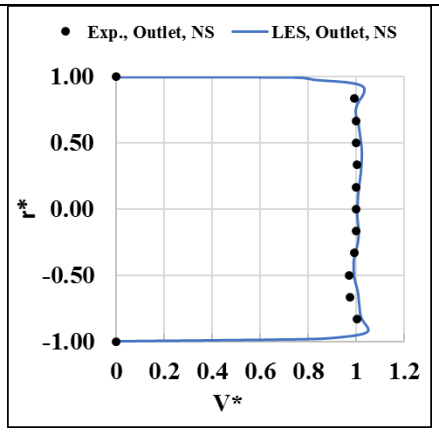
L/D=4	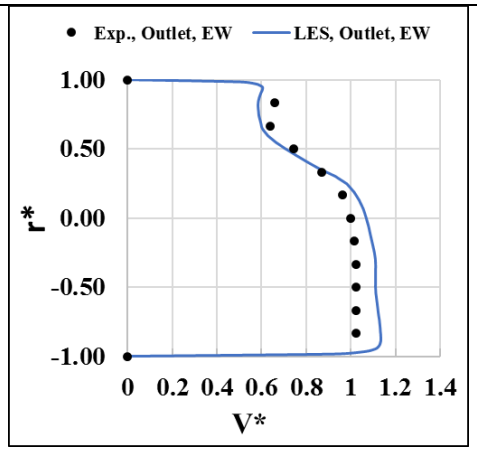	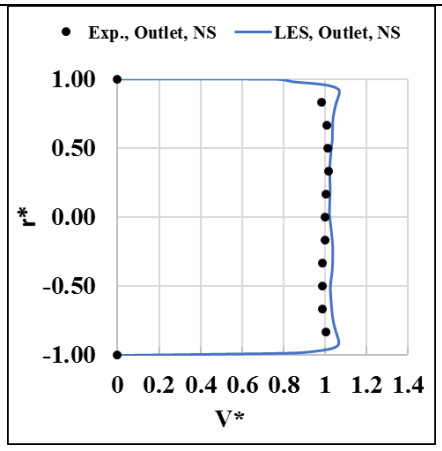
L/D=6	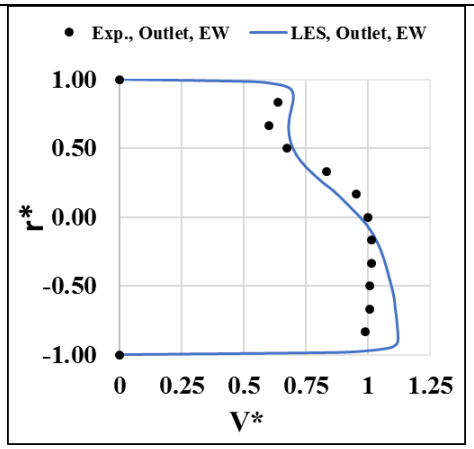	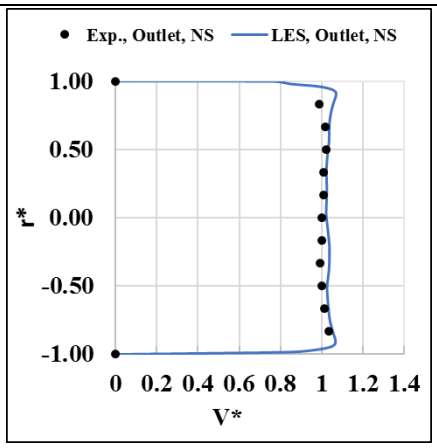

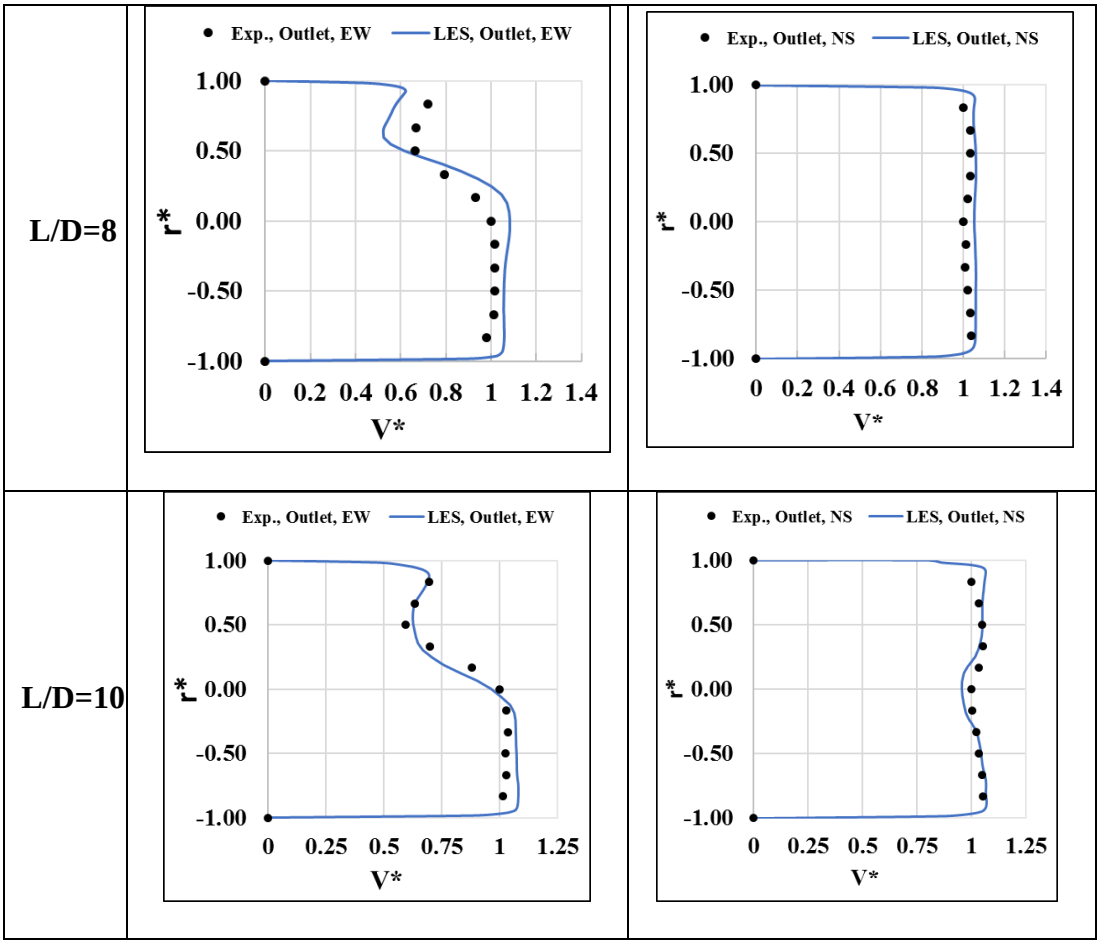

Figure 27. Velocity profiles (mean flow) at x/D=outlet for all L/D configurations at Re=3.5x10^5.

6.2.3 Re=4.5x10^5

$x/D = 1$ *Section: After First Elbow:*

Figure 28 below shows the velocity profiles for L/D= 4 configuration at x/D= 1 location, the velocity inlet is 17 m/s. It can be observed at this location that the velocity is lower closer to the convex wall just after the elbow and is higher on the concave wall. This is preliminary due to the sharp bend with high air flow velocity resulting in flow swirling and separations. This pattern is also observed in the other configurations L/D's. In Figure 28 (b) at N-S direction, the velocity profile is almost symmetrical, and the velocity is observed to be slightly lower near to the duct center.

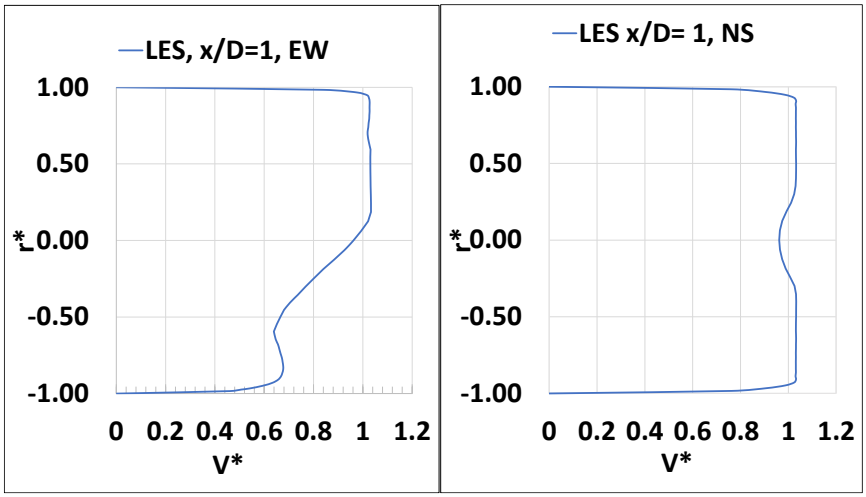

(a) (b)

Figure 28. Velocity profiles (mean flow) at x/D=1 for $L/D = 4$ configuration at Re=4.5x10^5. (a) E-W (East-West) orientation (b) N-S (North-South) orientation.

$x/D = 3$ *Section: In between Elbows:*

Figure 29 shows the velocity profile at x/D=3 for L/D=4 configuration at Re=4.5e^5. The E-W profile consistently demonstrates similar asymmetrical distribution predicted by LES on both sides of the duct walls. The flow velocity distribution on N-S direction shows symmetrical due to flow re-attachment.

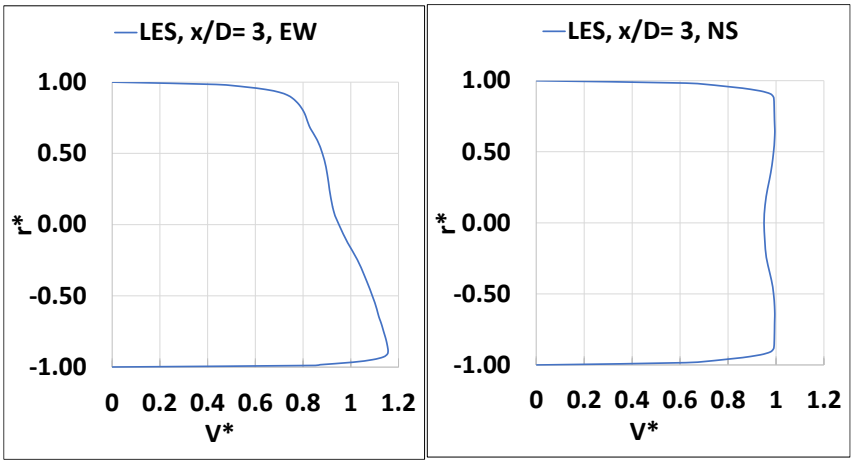

(a) (b)

Figure 29. Velocity profiles (mean flow) at x/D=3 for $L/D = 4$ configuration at Re=4.5x10^5. (a) E-W (East-West) orientation (b) N-S (North-South) orientation.

6.3 Results of Comparison of ζ-f, RSM, LES, and WMLES Models

Section x/D=1: After First Elbow:

The LES model significantly underpredicted the results in the flow reattachment region. Interestingly, results show that WMLES and ζ-f predictions are very close to each other. It should also be noted that LES seems unable to capture either flow separation or flow reattachment regions correctly, which could be due to mesh resolution. The mesh employed in the setup of this study could be insufficient to fully resolve all flow scales.

Results of LES estimates and other experiments for all models are found to be in agreement, except the WMLES results, where LES estimates do not match those of the experiments, especially at around r/D=0.5 where they underpredict both in flow separation and reattachment regions.

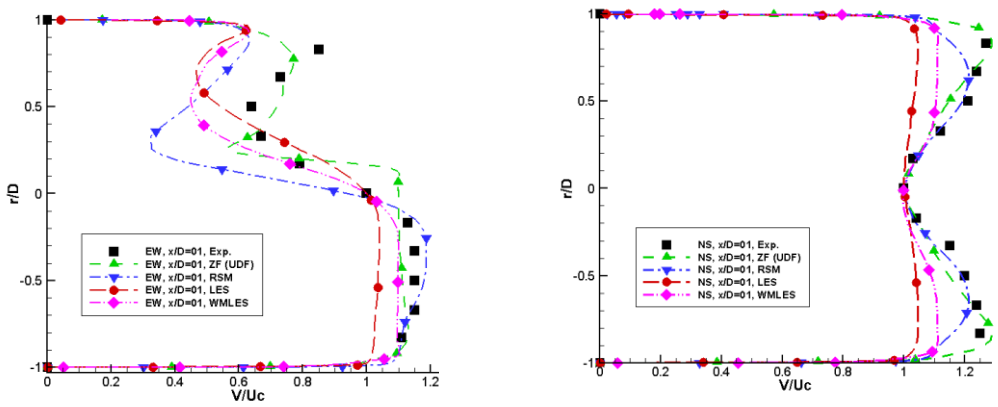

(a) (b)

Figure 30. Velocity profiles (normalized) for Z-F, RSM, LES, and WMLES models at $x/D = 1$: (a) E-W (East-West) Orientation (b) N-S (North-South) Orientation

Section between First and Second Elbows:

Flow distribution near the straight pipe section is in transition from a non-uniform to a uniform pattern. The duct sections discussed are analyzed for different locations (*x/D*=3,5 and 7) on the straight pipe.

x/D=3:

At $x/D = 3$, the normalized velocity profiles for all turbulence models are given in Figure 31. LES estimations for all models disagreed with the experimental results. Therefore, the LES model has consistently shown poor predictions for both reattachment and flow separation regions.

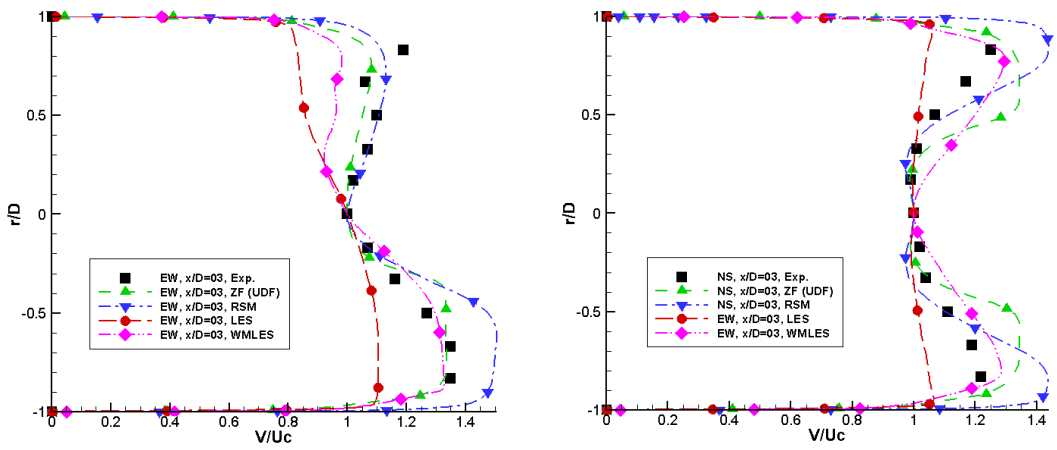

(a) (b)

Figure 31. Velocity profiles (normalized) for Z-F, RSM, LES, and WMLES models at $x/D = 3$: (a) E-W (East-West) Orientation (b) N-S (North-South) Orientation

x/D=5:

At $x/D = 5$, the normalized velocity profiles of ζ-f model and RSM model are consistent with the experiment. On the other hand, WMLES and LES model predictions do not agree so well. Figure 32 shows the velocity profiles for all turbulence model at this section.

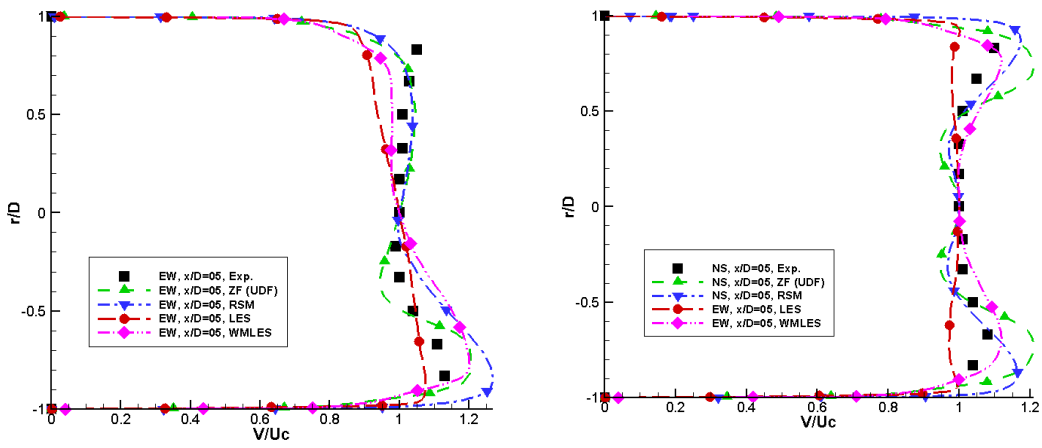

(a) (b)

Figure 32. Velocity profiles (normalized) for Z-F, RSM, LES, and WMLES models at $x/D = 5$: (a) E-W (East-West) Orientation (b) N-S (North-South) Orientation

x/D=7:

In the NS direction, the numerical results obtained by the LES model agree closely with experimental data. Figure 33 demonstrates that both RSM and WMLES models over-predict the mean flow velocity. For the EW direction, the LES estimates disagree with experimental results for all discussed models, resulting in over-predictions of the mean flow velocity.

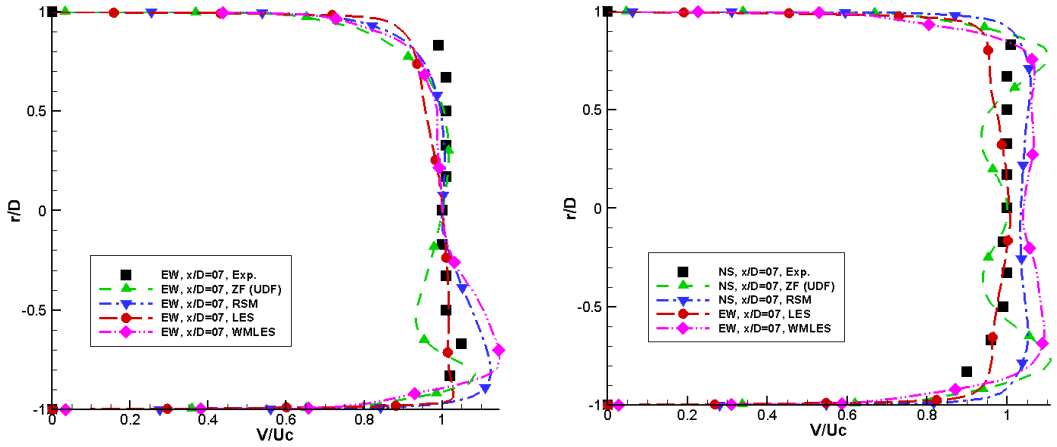

(a) (b)

Figure 33. Velocity profiles (normalized) for Z-F, RSM, LES, and WMLES models at $x/D = 7$: (a) E-W (East-West) Orientation (b) N-S (North-South) Orientation

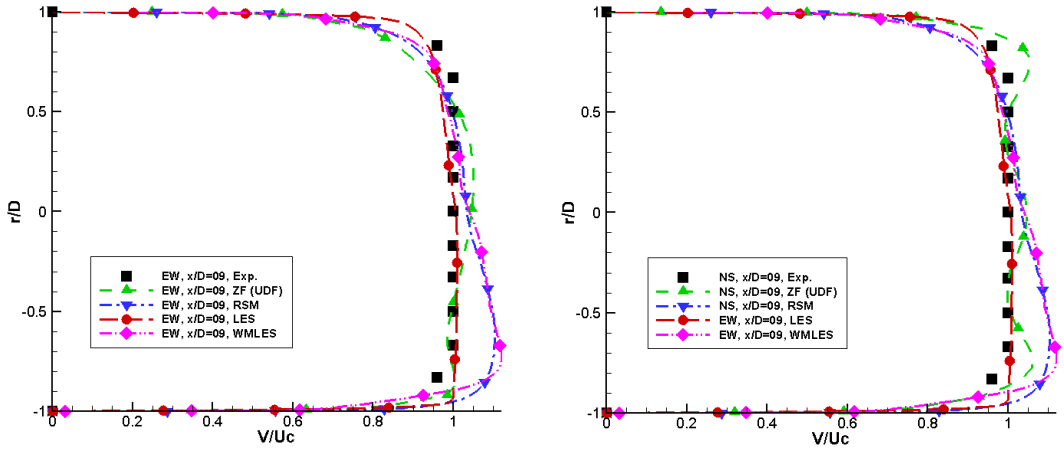

(a) (b)

Figure 34. Velocity profiles (normalized) for Z-F, RSM, LES, and WMLES models at $\frac{x}{D} = 9$: (a) E-W (East-West) Orientation (b) N-S (North-South) Orientation

Section x/D=9: Before Second Elbow:

For section x/D= 9, the outcomes for velocity profiles for normalized mean flow are shown in Figure 34. Here, for outer radial location, the RSM and WMLES

results are consistently over-predicted in both directions, whereas the ζ-f model results are comparatively better. The over-predictions for all turbulent models can be attributed to the mathematical errors that occurred during resolving upstream flow structures.

6.4 Closure Coefficients Determination

The turbulence modelling uses many different assumptions based on physics. Therefore, the diversity of turbulence model approaches makes it difficult to systematically determine closure coefficients. This can be achieved by setting the closure coefficient values to achieve good agreement with experimentally obtained data.

Smagorinsky suggested a constant coefficient to use for isotropic turbulence using the Smagorinsky model [61]. Germano et al. [69] established a dynamic coefficient model to account for the spatial and temporal variations.

All closure coefficients used in the current turbulent modelling research is based on empirical coefficients suggested from relevant research work performed by others. The values of these constants are derived from wide range of turbulent flow by using data fitting. The sensitivity study of these closure coefficients are not included in the scope of the current thesis.

6.5 Adverse Pressure Gradient Flow

Considering pipe flow over the elbow, the influence of pressure on the flow velocity is quite substantial. The fluid viscosity effect may increase shear stress, contributing to flow velocity reduction. This can be overcome with the negative (favourable) pressure gradient. In contrast, positive (adverse) pressure gradient phenomena give rise to flow separation.

6.6 Results Comparison of LES and Experiment Using Enhanced Near-Wall Treatment and Standard Wall Functions Methods

In general, standard wall functions can achieve reasonable accuracy both at high Reynolds number and simple wall-bounded flow conditions. The flow prediction accuracy using standard wall function suffers when the flow exhibits the following phenomena in which function limits are reached:

- Boundary layer separation due to severe pressure gradient
- Strong body force dominant flow such as buoyancy-driven flow
- Massively transpiration flow effect through wall such as suction or blower

6.7 Predicted Reynolds Shear Stress Components

The results of turbulence momentum transport can be represented using Reynold shear stress components. These components are described as momentum flux with the following relationship to the fluctuating velocity components: $\tau_{R_{xz}} = \tau_{R_{zx}} = -\rho\overline{u'w'}$, $\tau_{R_{yz}} = \tau_{R_{zy}} = -\rho\overline{v'w'}$, $\tau_{R_{xy}} = \tau_{R_{yx}} = -\rho\overline{u'v'}$.

6.8 Normal Reynolds Stress Components

Normal Reynolds stresses can be described as $\tau_{R_{xx}} = -\rho\overline{u'u'}$, $\tau_{R_{yy}} = -\rho\overline{vv'}$, $\tau_{R_{zz}} = -\rho\overline{w'w'}$. The imbalance of normal stress is a feature of secondary flow generation in the fluid domain.

6.9 Pressure Loss Coefficient

The total pressure loss across the Z-duct pipe is evaluated. Figure 35 shows the pressure loss coefficient obtained for 12” (305 mm) diameter Z-duct w/ close-coupled elbows configuration. The loss coefficient is plotted as a function of the separation distance L/D. The experiment data from ASHRAE RP-1682 [3] indicates pressure loss coefficient of around 0.21-0.26 with uncertainties around 0.011-0.019. Such measurement was performed with the upstream plane located before the first elbow and the downstream plane located after the second elbow. These LES-based results are compared to experiment as shown in Figure 35. Such CFD fluid planes are chosen at the similar locations to experiment. The LES predicted pressure loss is found to agree well at L/D=4 – 8. However, the predicted results are much lower at L/D=2 and slightly higher at L/D=10. These under and over-predictions behaviors are likely deemed to insufficient resolved flow structures that are contributing to flow energy in the pipe. The over-predicted momentum deficits at L/D=10 could account of the results of slightly higher-pressure loss and vice versa for L/D=2.

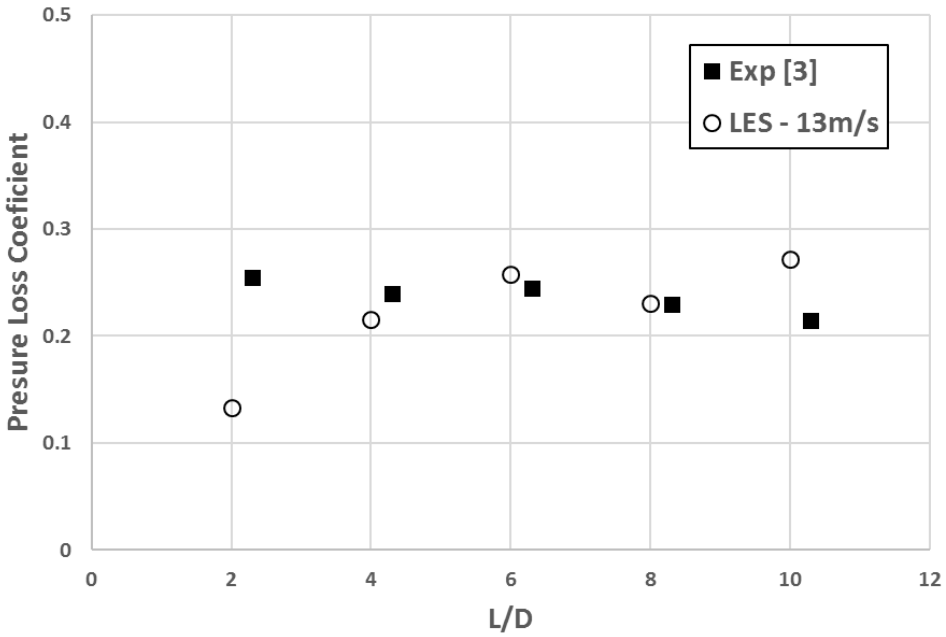

Figure 35. Pressure loss performance for different L/D of 12in Z-duct configuration

6.10 Turbulence Anisotropy

In turbulence flow, the DNS studies reveal that the mean velocity gradient generates a large-scale anisotropic structure as it stretches and aligns with the high energy turbulent eddies. This mean flow distortion explains why most turbulent flows are anisotropic and its directional preference.

6.11 Contours Plots of Mean Flow Velocity

Generally, the information in the LES model consists of numerous flow variables. In this section, 2D contours of mean velocity magnitude with $^{x}/_{D}$ will be inlet followed by 1, 3, 5 and finally the outlet, for diverse L/D configurations are further analyzed. In the absence of experimental data to certify LES contours, the visualization of the footprint for the entire fluid planes becomes essential. In previous profiles, only parts of the planes were confirmed.

Figure 36 presents the contours in mean velocity magnitude. In the case of the

inlet section, a uniform velocity distribution for different L/D configurations can be observed. However, at L/D =5, velocity distribution was greater in the lower region. As shown, the velocity magnitude is only 1–2 m/s apart, which means that the velocity gradient is relatively small. That is to be expected as the entrance lengths for all configurations are identical to the completely developed flow profile.

At the $x/D = 1$ location, the velocity contours are observed to be asymmetrical in pattern and non-uniform. This may be a result of the existence of reattachment and local flow separation closer to the other side of the walls. Higher velocities are usually present within the outboard of the duct in flow reattachment. On the other hand, low velocities are present in the inboard sections of the duct in the flow separation region. For all L/D configurations, almost half of the duct circular is dominated by both flow regions.

At the $x/D = 3$ section, the flow distribution of the straight pipe closer upstream is studied for all L/D configurations. Flow that recovered from the separation is shown in yellow. It is found that although the flow has recovered, it is still not closer to the required inlet velocity. Moreover, the swirling of flow around the straight pipe is observed. Flow structures in the pipe are likely an effect of this swirling effect.

For the $x/D = 5$ section, located before the second elbow, the contour shows the flow distribution furthest downstream. Here, flow velocity is transitioning from the non-uniform upstream pattern to the uniform downstream pattern. In addition, the swirling effect is decreased. This flow distribution is found for all L/D configurations. In all L/D configurations, the contour figures for outlet showed highly non-uniform velocity distributions. In the region of local flow circulation, the flow velocities are found closer to the upper region. This happens because of flow separation at 90° elbow turn.

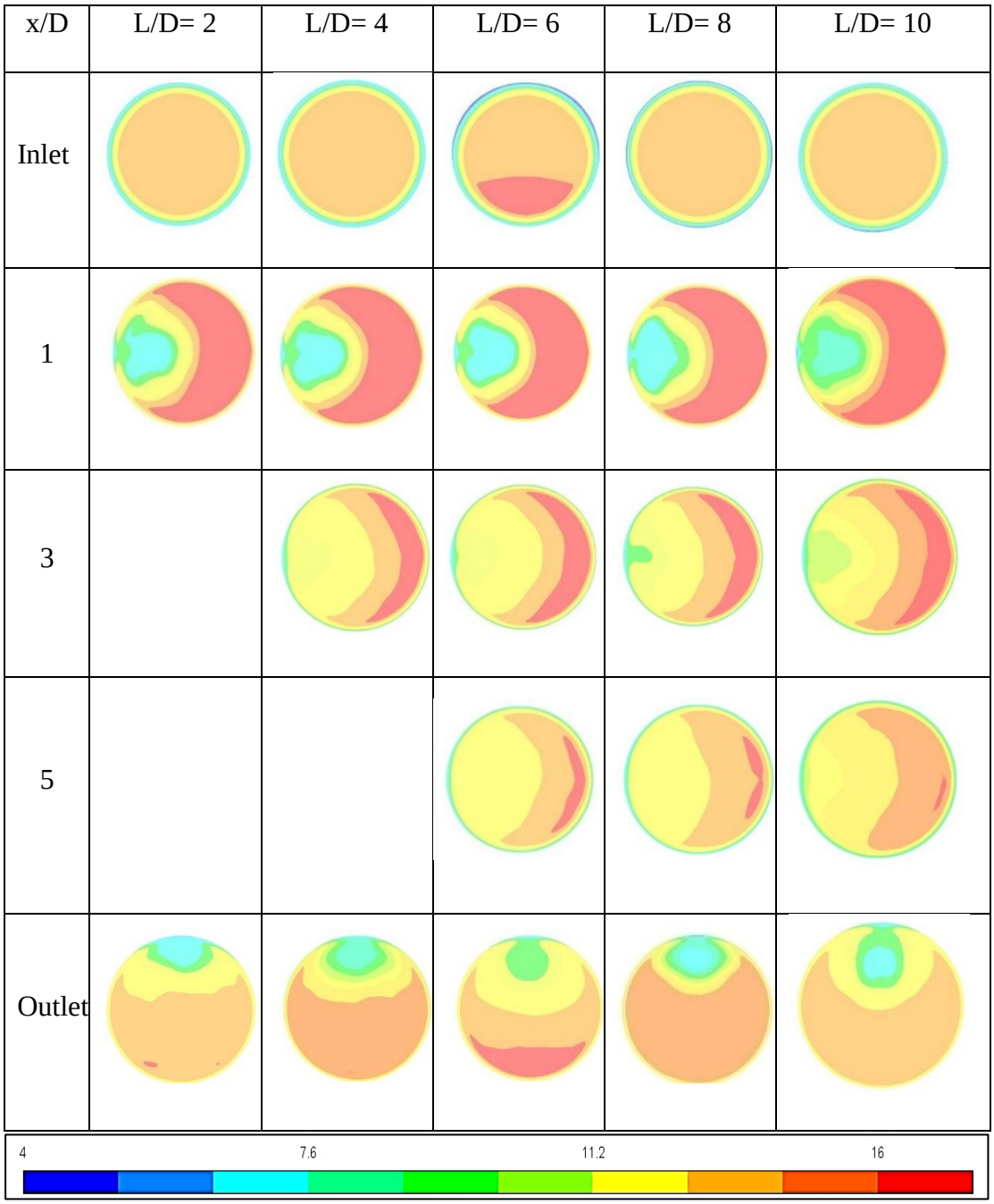

Figure 36. Mean velocity contours in m/s

6.12 Turbulent Kinetic Energy (k) Contours

The components of instantaneous flow velocity u, v and w are decomposed such that: $u = \bar{u} + u'$, $v = \bar{v} + v'$ and $w = \bar{w} + w'$ where mean flow quantities are represented by $\bar{u}$ and $\bar{v}$ and $\bar{w}$ and fluctuating components by u', v' and w'. Equation (43) expresses the resolved turbulent kinetic energy (k) along with fluctuating

components.

$$k = \frac{1}{2}\left(\overline{u'^2} + \overline{v'^2} + \overline{w'^2}\right) \quad (43)$$

For different L/D configurations, the LES estimate of k for cross-sectional planes is given in Figure 37. For all cases, it is evident from the figure that on the verge of the turning radius, the value of k shows consistent tendency to increase. While approaching the second elbow, k decreases gradually, and after near-corner transition, it increases once again. Due to the existence of turbulent mixing enhancement, sheared flow develops. When the value of k is decreasing, viscous forces dissipate the large-scale flow structures at the Kolmogorov scale. The k is higher in region between elbows when L/D = 2. It is mainly due to restricted vertical length in stream wise direction, which helps viscous dissipation.

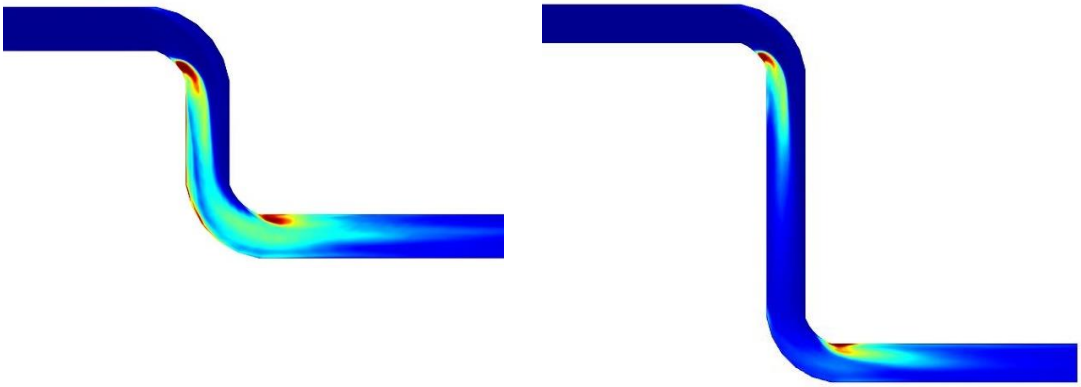

(a) L/D=2 (b) L/D=6

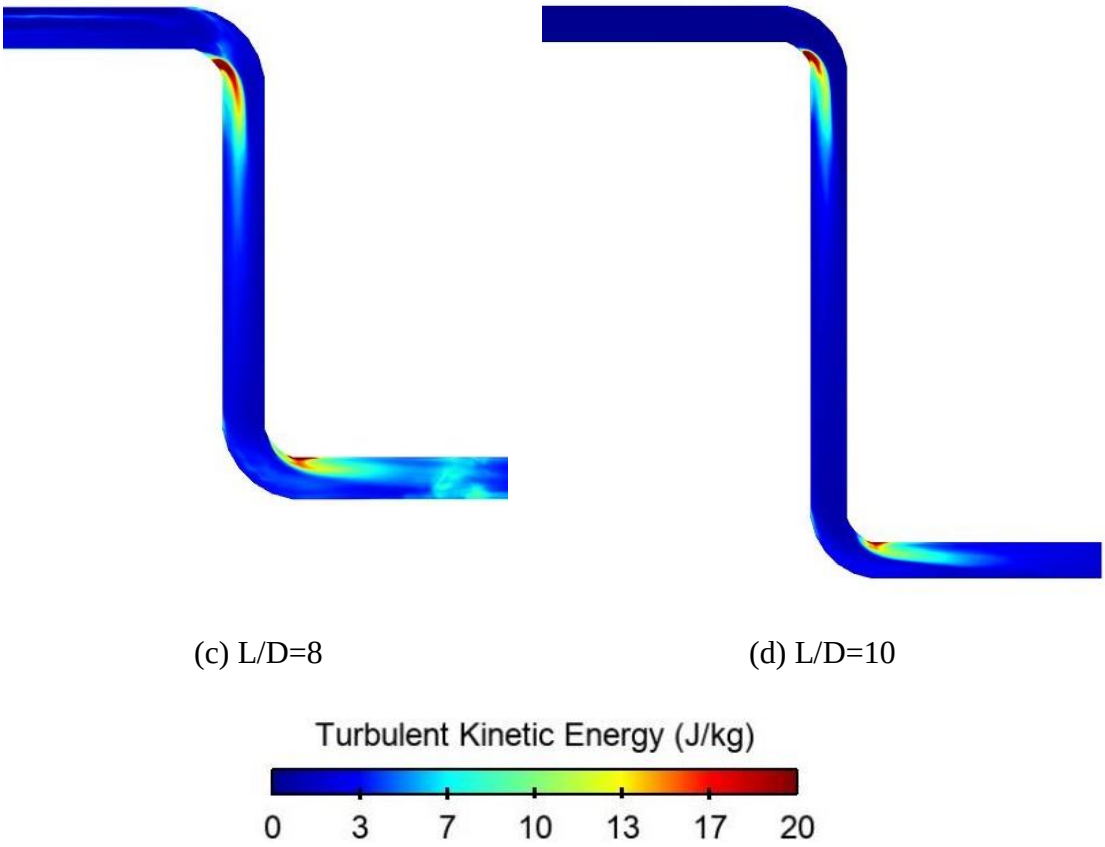

(c) L/D=8 (d) L/D=10

Figure 37. Turbulent kinetic energy (k) per mass for all L/D: (a) L/D=2 (b) L/D=6 (c) L/D=8 (d) L/D=10

Equation (44) characterizes the turbulent kinetic energy and its production, transport, and dissipation terms.

$$\frac{Dk}{Dt} + \nabla \cdot T' = P - \varepsilon \tag{44}$$

where turbulence transport, production, and dissipation of k are represented by $\nabla \cdot T', P$ and ε, respectively.

Turbulent kinetic energy can be used to study each process managing turbulent flow motion. If k increases near the elbow region, P is expected to be greater than ε, which means that there is more turbulence near the local boundary layer. Similarly, if the P is less than ε, the boundary layer is less turbulent.

6.13 λ_2-criterion Iso-Surfaces

To visualize the turbulent flow structures in 3D, a post-processing technique using λ_2-the criterion can be used as shown in Figure 38. λ_2-criterion finds a local minimum for vortex pressure. Moreover, the figure shows that the flow structures are dissipating downstream from the elbow. In that region, the viscous dissipations are very dominant compared to upstream, where turbulent production dominates. For this reason, the smaller eddies are found downstream. In the region upstream, large-size turbulent structures are found. Larger turbulent flow structures govern the swirling effects. Consequently, flow structures with higher velocity near the elbow are dominant closer to the near-wall region.

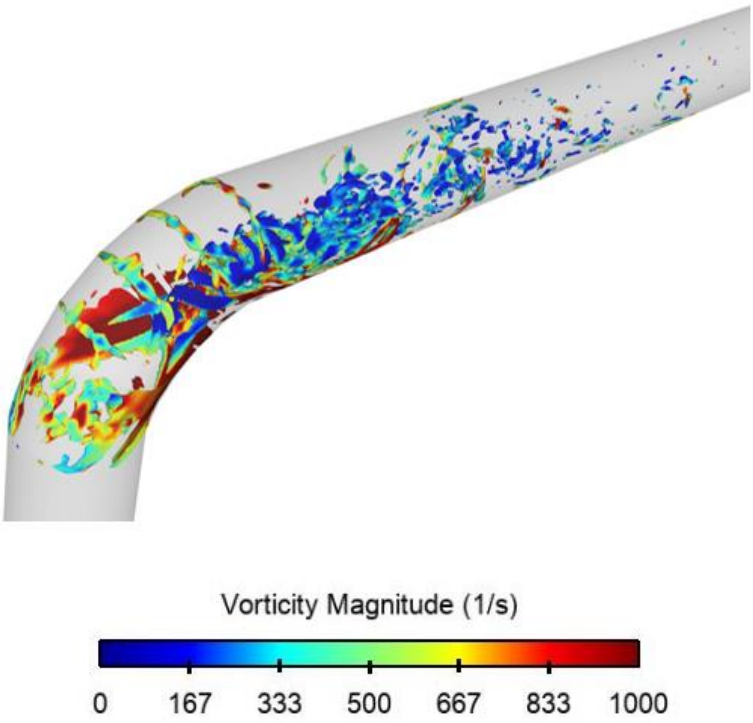

Figure 38. λ_2-criterion iso-surfaces highlighted according to vorticity magnitude for L/D=10

6.14 Turbulence Modeling for Higher and Lower R_e in the ζ-f Model

The flow pattern of fluid inside a Z shape pipe was recorded with ζ-f model for fluid velocities of 8 m/s and 18 m/s. The flow pattern of fluid was observed in EW and NS directions with a mean position at the piper center. The pipe length was divided into 7 sections; inlet, x/D of 1, 3, 5, 7, 9, and outlet. Results obtained from the ζ-f model were presented in the dimensionless form using a graphical representation of a juxtaposition of radius and velocity. Simulation results for the velocities of 8 m/s and 18 m/s show that at inlet the flow pattern of the fluid is the same in both EW and NS directions. Flow patterns in the area nominated as x/D = 1 show a very different profile for EW and NS direction when the fluid velocity at 8 m/s. The flow pattern of fluid does not change much in EW direction showing that this direction has very uniform flow fluid from inlet to the x/D = 1 while the NS direction displays a velocity drop near the mean section of the pipe. This drop of fluid velocity can be due to a drop in the momentum of fluid. Drop-in momentum itself can be due to the presence of a vortex in that region.

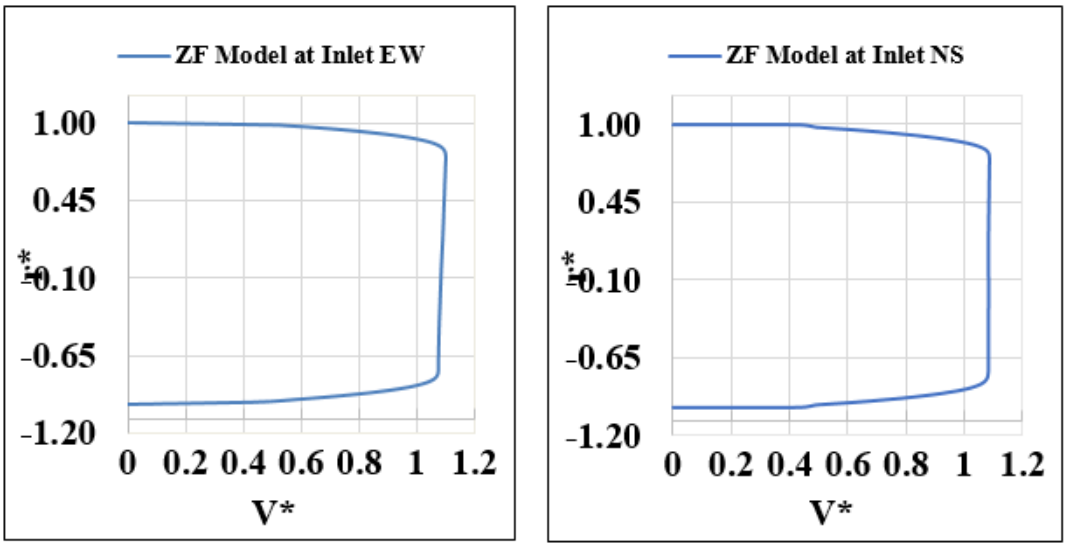

(a) (b)

Figure 39. Velocity profiles (normalized) for ζ-f model at inlet (8 m/s): (a) E-W (East-West) Orientation (b) N-S (North-South) Orientation

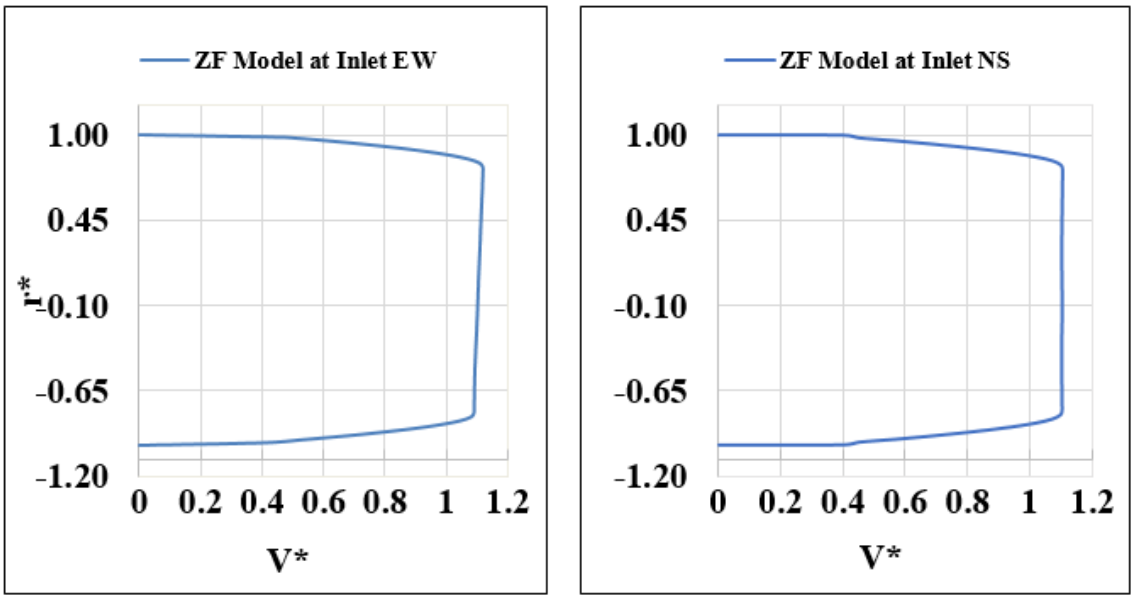

(a) (b)

Figure 40. Velocity profiles (normalized) for ζ-f model at inlet (18 m/s): (a) E-W (East-West) Orientation (b) N-S (North-South) Orientation

The comparison of the profile of flow of 18 m/s with the 8 m/s shows that the velocity of fluid does affect the flow pattern of fluid inside the pipe. As in 18 m/s, the fluid flow profile for x/D = 1 shows that in EW direction the flow is highly non-uniform as the graphical representation of the profile shows an asymmetrical curve. The curve has changed in shape in the positive radial direction while the negative radial direction remains the same. This asymmetrical curve of the fluid flow pattern also explains the presence of the reattachment and local flow separation region. The NS direction, in this case, does not show a changed profile as compared to that of the 8 m/s but the velocity drop near the mean position of the pipe is much larger in this case. This larger drop in fluid velocity shows that the fluid velocity has an impact on the fluid flow patterns

inside the pipe.

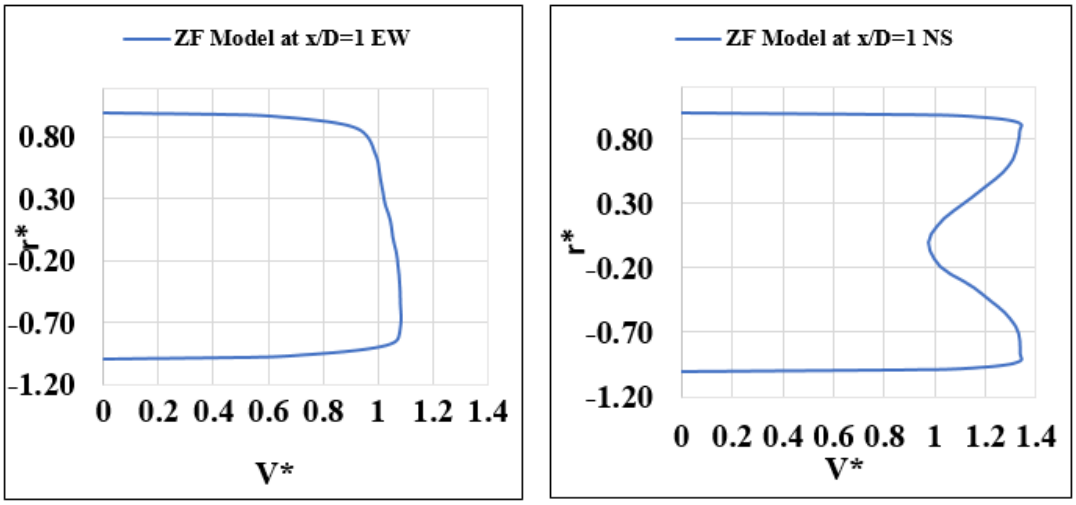

(a) (b)

Figure 41. Velocity profiles (normalized) for ζ-f model at section $x/D = 1$ (8 m/s):

(a) E-W (East-West) Orientation (b) N-S (North-South) Orientation

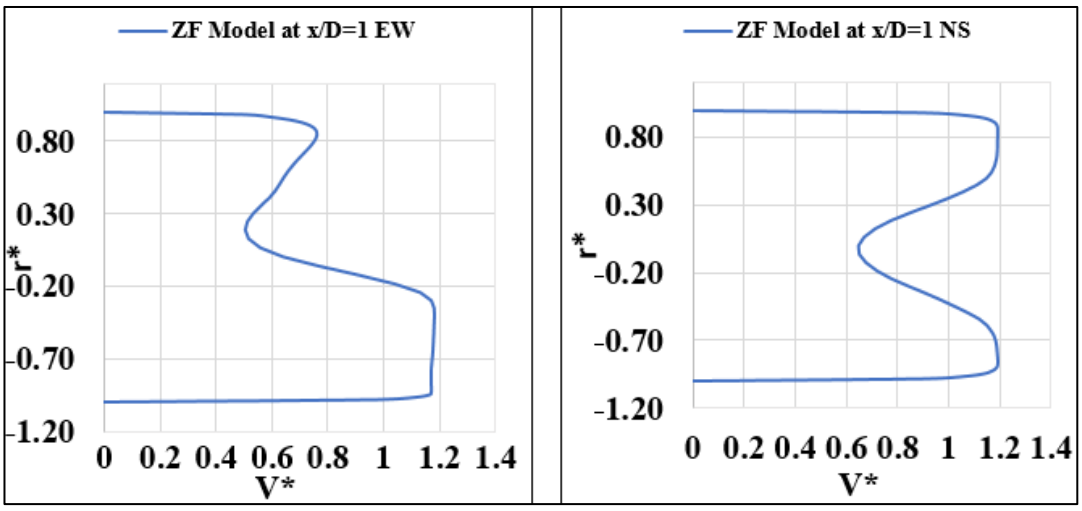

(a) (b)

Figure 42. Velocity profiles (normalized) for ζ-f model at section $x/D = 1$ (18 m/s):

(a) E-W (East-West) Orientation (b) N-S (North-South) Orientation

Comparing the fluid flow profile of x/D = 3 with x/D = 1 for the fluid velocity of 8 m/s show that even at that slow speed the fluid flow profile gets changed at every section of the pipe. As the graphs show the fluid flow profile at the section x/D = 3 changes for EW direction and fluid flow is now slightly non-uniform as the graph shows some asymmetric shape. This asymmetrical curve of the fluid flow pattern also explains the presence of the reattachment and local flow separation region. In the NS direction, the flow of fluid is similar to that of the x/D = 1 as a drop of velocity near the mean position of the pipe but the drop magnitude and the largest recorded velocity are lower than that of the previously recorded. The decrease of fluid flow velocity is due to the drop in the momentum of fluid, where fluid momentum drop can be due to the presence of vortex at the same region.

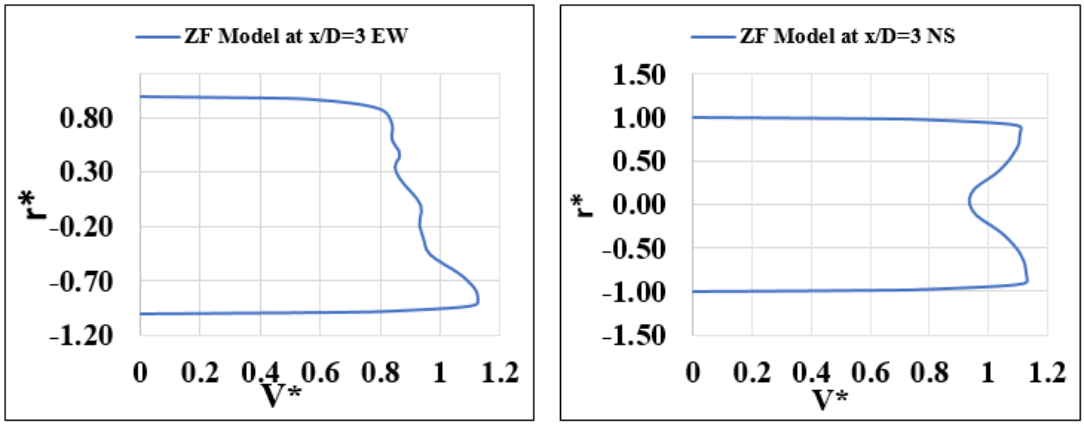

(a) (b)

Figure 43. Velocity profiles (normalized) for ζ-f model at section $x/D = 3$ (8 m/s): (a) E-W (East-West) Orientation (b) N-S (North-South) Orientation

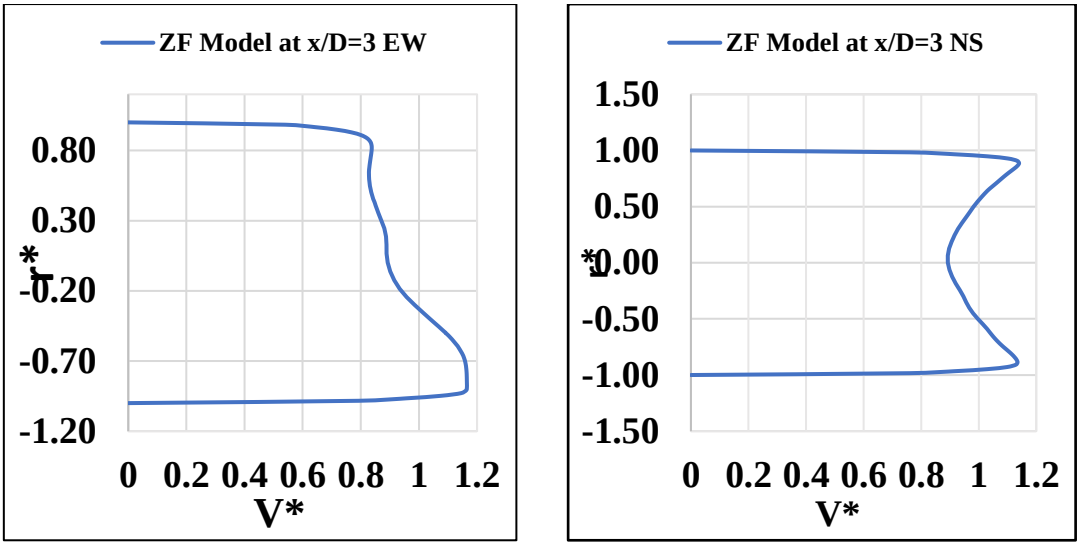

(a) (b)

Figure 44. Velocity profiles (normalized) for ζ-f model at section $x/D = 3$ (18 m/s): E-W (East-West) Orientation (b) N-S (North-South) Orientation

Similarly comparing the fluid flow profile of x/D = 3 with x/D = 1 for the fluid velocity of 18 m/s in Figure 42 and Figure 44 show that at high speed the fluid flow profile get changed at every section of the pipe and flow starts to get uniform in EW direction. Results clearly show that there is an increase in the uniformity of the flow of fluid as fluid moves from x/D = 1 to x/D = 3. The asymmetric shape of the graphic especially in the positive region of radius starts to get symmetric in the EW direction. In the NS direction, the two major changes were observed in this region. As the fluid moves further from x/D = 1 the decrease in the flow of fluid spread from the center to almost the entire radius in NS direction. As can be observed in graphs that the decrease in velocity of fluid start from the very beginning of the positive outer side of the radius and continues to increase till the center from where it starts to increase till it reaches its maximum value. The second change was observed in maximum value fluid flow velocity which was reduced from about 1.25 to less than 1.15. Comparing the fluid flow

profile for both 8 m/s and 18 m/s shows that in 8 m/s the further movement of the fluid makes it a little non-uniform in EW direction while in 18 m/s the further movement of the fluid makes it slightly more uniform in EW direction.

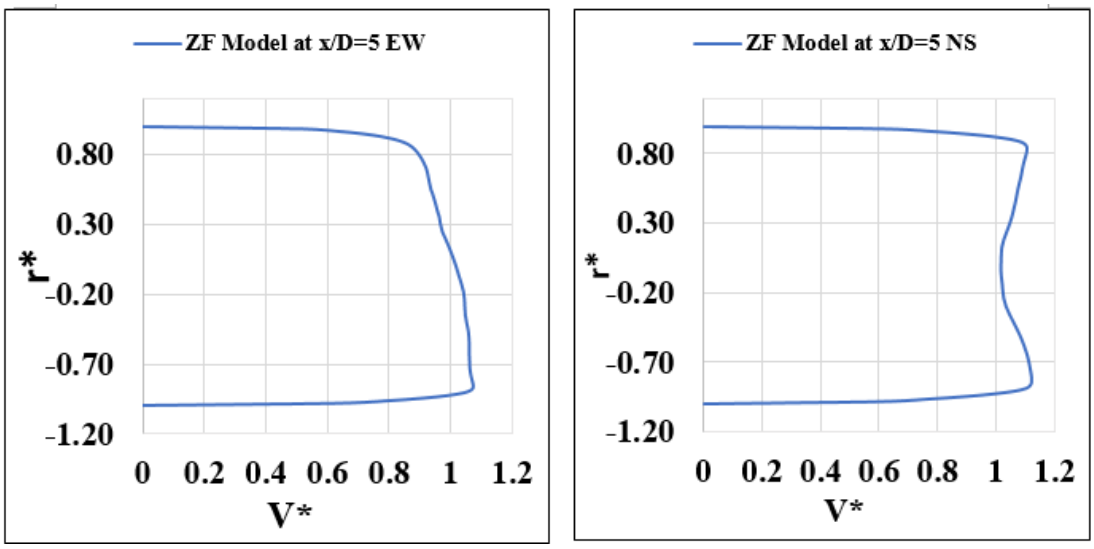

(a) (b)

Figure 45. Velocity profiles (normalized) for ζ-f model at section $x/D = 5$ (8 m/s): (a) E-W (East-West) Orientation (b) N-S (North-South) Orientation

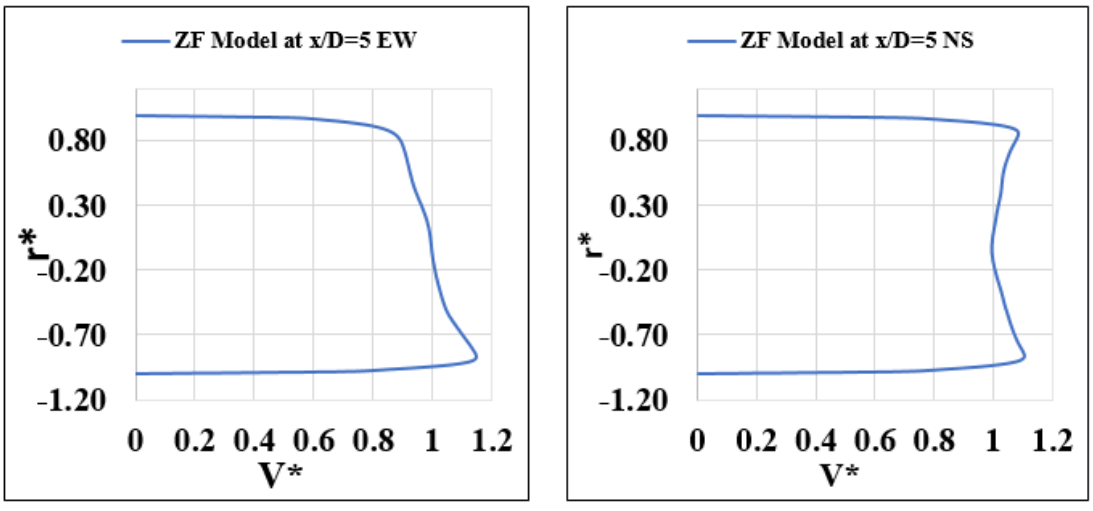

(a) (b)

Figure 46. Velocity profiles (normalized) for ζ-f model at section $x/D = 5$ (18 m/s): (a) E-W (East-West) Orientation (b) N-S (North-South) Orientation

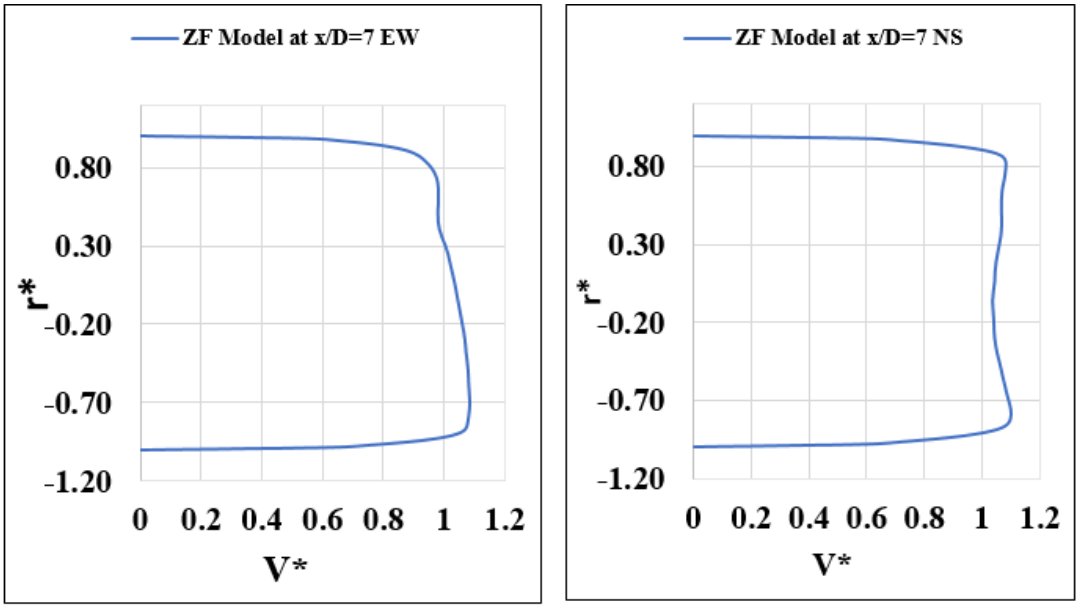

(a) (b)

Figure 47. Velocity profiles (normalized) for ζ-f model at section $x/D = 7$ (8 m/s): (a) E-W (East-West) Orientation (b) N-S (North-South) Orientation

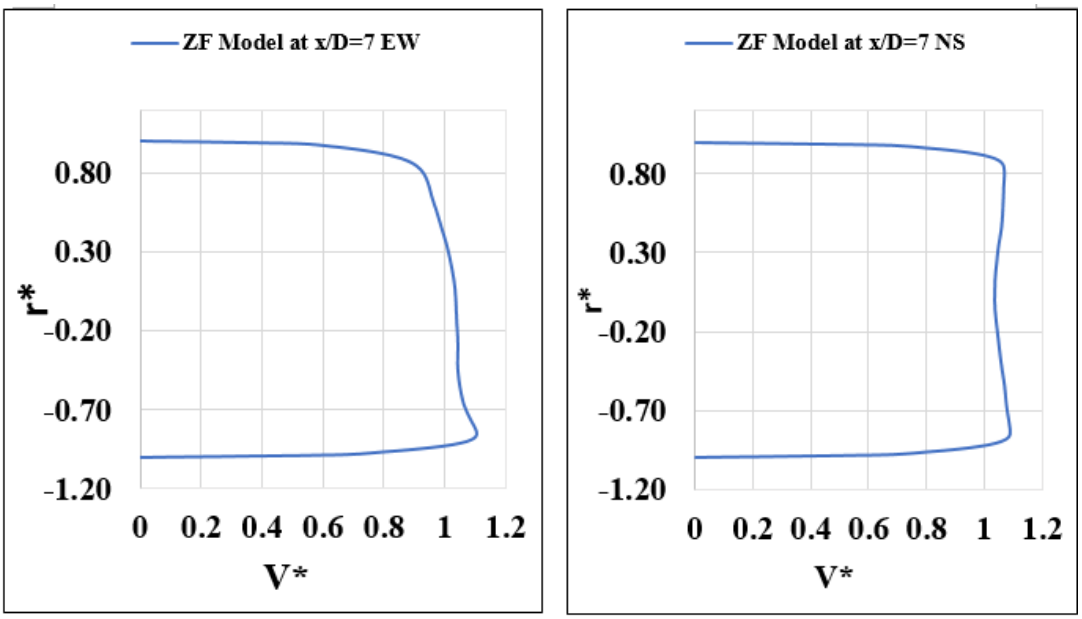

(a) (b)

Figure 48. Velocity profiles (normalized) for ζ-f model at section $x/D = 7$ (18 m/s): (a) E-W (East-West) Orientation (b) N-S (North-South) Orientation

Comparing the x/D = 5 of 8 m/s with x/D = 3 in Figure 43 and Figure 45 shows that the disturbance in the EW flow direction starts to decrease as the fluid passes from section 3 to section 5 of the pipe. As shown in the graphical representation of the EW direction the asymmetric line of radius against the velocity starts to decrease as compared to the previous one. This means that flow of fluid in EW direction becoming more uniform as the fluid moves further into the pipe. Comparing this graph with that of the 18 m/s velocity shows that at a higher velocity of the fluid same trend of increase in the uniformity of flow of fluid as it moves further into the pipe was observed. For the flow in NS direction, a new profile of fluid flow was observed which shows that the length of decreased fluid velocity was increasing. A graphical representation of the fluid flow inside the pipe shows that the reduced velocity area has increased and the magnitude of the peak value of the decreased velocity has increased. This new shape at x/D = 5 means that the vortex created in the previous section is expanding its area in further section but has less intensity and thus produce lesser decrease in velocity at the affected area. The graphical representation of radius against the velocity also shows that the maximum velocity of the fluid is this direction is also decreased as the maximum velocity of the fluid recorded in this section was reduced to below 1.12 slightly less than the maximum velocity recorded in the last section of the pipe. Comparing the graph with that of the 18 m/s velocity shows that at a higher velocity of the fluid, the same trend of decrease in maximum velocity of the fluid with an increase in the magnitude of the peak a decreased velocity was observed .

At a fluid flow velocity of 8 m/s, the flow pattern in EW direction and at section x/D = 7, and x/D = 9 of pipe shows that the more the fluid moves further into the pipe the flow pattern is becoming more uniform. As evident from the graphical representation in Figure 47 and Figure 49, the graph line is becoming more symmetric

as fluid moves further in the pipe from section x/D = 7 to x/D = 9, the same was also observed when fluid moves from x/D= 5 to x/D= 7. The reason behind this smooth and uniform flow along EW direction is that the initial disturbance created at the inlet starts to lose its impact as fluid move further along the length of the pipe. The disturbance created due to the reattachment and local flow separation at the initial section start to disappear in further sections of the pipe and thus making the flow of fluid more uniform and smoother in lateral sections of the pipe. As shown in Figure 48 and Figure 50, at fluid flow velocity of 18 m/s, the flow pattern in EW direction and at section x/D = 7, and x/D = 9 of pipe shows that the more the fluid move further into the pipe more uniform the flow pattern it will have but this conversion is much more effective and fast as compared to that of the 8 m/s. As can be seen in the graphical representation of the said section, the graph line is becoming more asymmetric when compared to the initial pipe section of x/D = 1 and x/D = 3. As fluid moves further in pipe from section x/D = 5 to x/D = 7 and then from x/D = 7 to x/D = 9 fluid flow pattern became smoother and uniform. The reason behind this smooth and uniform flow along EW direction is that the initial disturbance created at the inlet starts to lose its impact as fluid move further along the length of the pipe. The disturbance created due to the reattachment and local flow separation at the initial section start to disappear in further sections of the pipe and thus making the flow of fluid more uniform and smoother in lateral sections of the pipe.

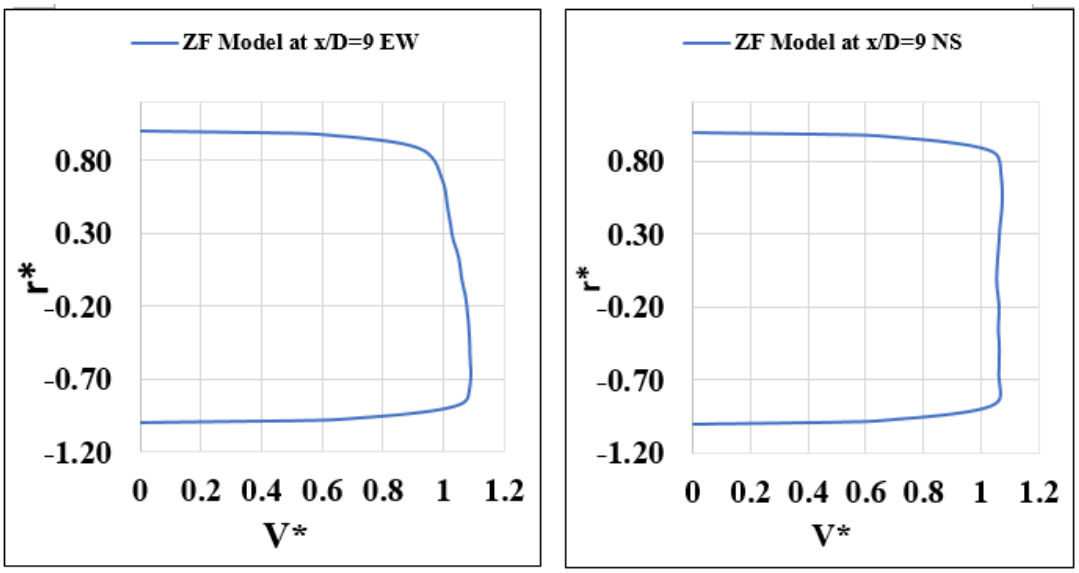

(a) (b)

Figure 49. Velocity profiles (normalized) for ζ-f model at section $x/D = 9$ (8 m/s): (a) E-W (East-West) Orientation (b) N-S (North-South) Orientation

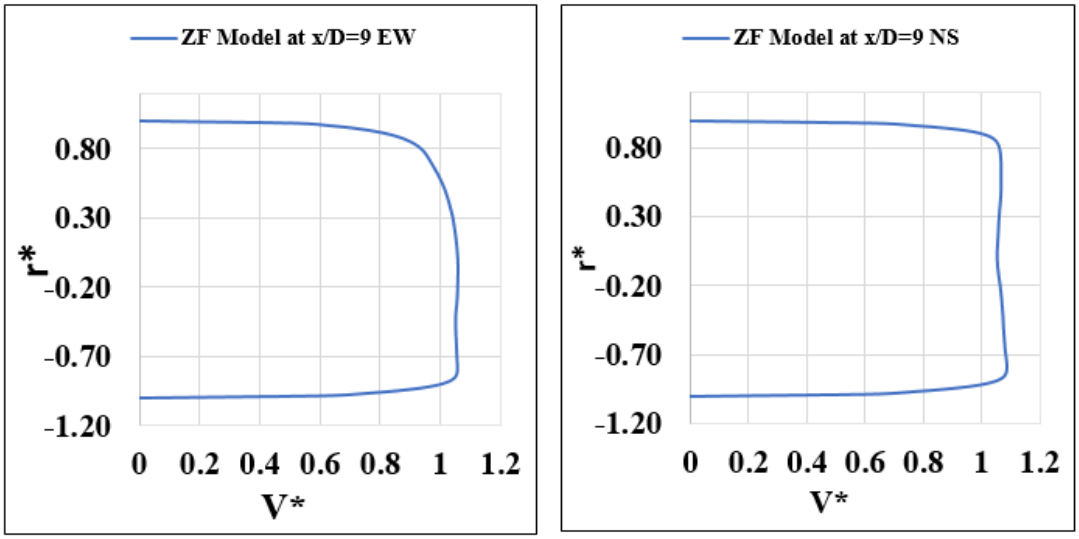

(a) (b)

Figure 50. Velocity profiles (normalized) for ζ-f model at section $x/D = 9$ (18 m/s): (a) E-W (East-West) Orientation (b) N-S (North-South) Orientation

Fluid flow patterns in NS direction for the fluid velocity of 8 m/s at different sections of pipe that is at x/D = 5, x/D = 7, and x/D = 9 were also analyzed. The result

show that the vortex that was created initially at the start of the pipe section x/D = 1 and was having a significant effect till x/D = 3 starts to fade away at the start of the section x/D = 5 and flow continues to become more uniform till the last section of pipe that is x/D = 9. The process of transformation of fluid flow inside the pipe from a highly non-uniform and unsteady flow to a steady and uniform flow starts from x/D = 5 as shown in the graph. Initially, the decreased fluid velocity in the center region starts to recover and try to match with the maximum velocity of the fluid. This process continued for section x/D = 7 were very small differences remain between center region velocity and maximum velocity of the fluid present inside the fluid. When fluid moves further to the next section of x/D = 9 the decrease in velocity of the center region became equal to the maximum fluid velocity means there is no slower velocity present at this stage of the flow. Similarly, at a fluid velocity of 18 m/s, the flow pattern in NS direction and at section x/D = 7, together with x/D = 9 of pipe shows that the more the fluid moves further into the pipe more uniform the flow pattern it will have. The result show that the asymmetric graph due to unsteady and non-uniform flow that was created initially at the start of the pipe section x/D = 1 and was having a significant effect till x/D = 3, starts to get symmetric, steady, and uniform at the start of the section x/D = 5 and continue to become more uniform till the last section of pipe that is x/D = 9. At section x/D = 9 there are no local flow separation regions and no evidence of reattachment that were introduced initially in the flow at section x/D = 1.

CHAPTER 7: Conclusions

7.1 Results for ζ-f and RSM models

Results related to the ζ-f and RSM are presented in this section. Both above-mentioned models are developed from steady-state RANS solutions. The results associated with the reattachment and flow separation regions are kept in focus. For the RSM model, simulated results disagree with experimental results. Moreover, RSM model is found lack of robustness in predicting mean flow velocity for different L/D configurations. Within the flow separation region where swirling is dominant, RSM model under-predicts the flow velocity. In the flow re-attachment region, RSM exhibit higher inaccuracy behavior than ζ-f. In addition to these results, the mean flow velocity results are also calculated, and the results show that the predictions of the RSM model disagree with experimental results.

In the next part of the study, the ζ-f model is studied for the Z-shaped duct. It should be noted that literature on the model in that conditions is limited. For the ζ-f model, a new UDF script was established. The reproduction of the process of production of turbulent kinetic energy in the ζ-f model is less difficult, and the accuracy of this reproduced energy proved to be excellent. The ζ-f model outperformed the RSM model, as its results were more in line with available experimental data. Moreover, the ζ-f model requires less computational data than the RSM model. In particular, the ζ-f model's numerical results were much better suited for predicting wall-bound flow.

The flow inside a Z shape pipe was analyzed for the two different velocities of 8 and 18 m/s using the ζ-f model and the result concluded that the initial flow pattern of fluid is highly dependent on the fluid flow velocity. At both velocities, the fluid flow shows asymmetric flow in the EW direction and a drop of velocity in the central flow region in the NS direction. Both fluid flow patterns have different magnitude with 8

m/s having a flow pattern of lower magnitude. For both velocities when the asymmetric flow in EW direction and reduced velocity of the fluid in NS direction starts to convert to a symmetric flow and uniform velocity respectively as the fluid moves further into the pipe along the length of the pipe. The process of this conversion of flow from highly asymmetric and non-uniform to an asymmetric and uniform flow starts from section x/D = 5 and it ends at the last section of the pipe that is x/D = 9.

7.2 Results for the LES Model

Like with other models, the LES model results are juxtaposed with available experimental data, for Reynolds number (Re) = 3.5×10^4. Moreover, turbulent behavior over a varied range of L/D is also analyzed. The following are the results at $L/D = 2$, which represents the coupling of two elbows.

- For mean flow velocity profiles, the LES predictions and experimental data show results in agreement for the considered range. of L/D, and it is ascribed to well-resolved flow structures that are large-scale. However, small over and underestimates at specific distances are observed while comparing the absolute values due to the restricted modeling approach for predicting eddies structures.
- This study identifies significant flow turbulence characteristics at inlet section. These main features are categorized as reattachment and separation regions.
- For L/D at x/D= 3 and 5 within the region of flow transition, inconsistencies were found to be more severe. Some inconsistencies or discrepancies were assumed to be originated from the numerical errors previously quantified based on velocity profile against experimental data. Both upstream x/D=1 and downstream x/D=3 have demonstrated under-predicted velocity profile issues and x/D=3 is found to be worse than x/D=1. Such numerical errors are deemed lack of proper modeling approach at the

upstream flow region. It is suggested that such problem can be solved by using a resolution with a finer mesh or by using spatial discretization of a higher order. This effort will help in attempt to properly resolve the local velocity gradients of structures. Moreover, by resolving upstream inconsistencies, the downstream duct flow precision can also be enhanced.

The LES simulation results applied to the Z-shaped duct have shown some issues with robustness in accurately predicting the flow separation and reattachment regions. Grid resolution is likely not fine enough to allow better filtering grids for smaller-scale eddies. If a finer mesh is applied, the filtering function should allow more scales to be resolved and is therefore expected to achieve higher accuracy.

CHAPTER 8: Recommendations and Future Work

The following are suggestions for future work to help improve numerical prediction accuracy related to completely developed Z-shaped duct flow at high Re conditions:

To successfully deploy the LES model, a significant factor is suitable spatial resolution. The large-scale extremely anisotropic turbulent flow characteristics present in bulk flow must be fully resolved, while the sub-grid model is needed to resolve the near-wall region. With complex flow such as Z-shaped duct flow, small vortices present in near-wall regions contain highly turbulent energy and are hard to separate from a bulk flow based on length scale. It is therefore considered poorly suited for LES predictions if the grid solution is not applied in near wall-regions satisfactorily.

The fine-scale structures in near wall region are found relatively isotropic, and such a sub-grid modeling approach remains open to be improved. The conventional eddy-viscosity model, such as the Smagorinsky model, which can represent such strain rate relationship is found to be overly dissipative. In addition, the constant obtained from the Smagorinsky model, originally endorsed based on a simple flow of decaying turbulence, is found not well suited for complex flow. In near-wall regions, the eddy viscosity does not disappear. To satisfy this condition, a damping function is currently employed. It is essential to study different types of damping function approaches such as two-point closures, dynamic models, structure function models, scale-similar and mixed models, deconvolution techniques, and truncated treatment. The new technique of ILES (implicit large-eddy simulation) relies on special numerical arrangement to provide dissipation of turbulent energy in the region where fine scale structures are not resolved.

REFERENCES

[1] M. Salehi, A. K. Sleiti, and S. Idem, “Study to identify computational fluid dynamics models for use in determining HVAC duct fitting loss coefficients,” *Sci. Technol. Built Environ.*, vol. 23, no. 1, pp. 181–191, Jan. 2017, doi: 10.1080/23744731.2016.1204889.

[2] A. Sleiti, M. Salehi, and S. Idem, “Detailed velocity profiles in close-coupled elbows—Measurements and computational fluid dynamics predictions (RP-1682),” *Sci. Technol. Built Environ.*, vol. 23, no. 8, pp. 1212–1223, Nov. 2017, doi: 10.1080/23744731.2017.1285176.

[3] M. Salehi, S. Idem, and A. Sleiti, “Experimental determination and computational fluid dynamics predictions of pressure loss in close-coupled elbows (RP-1682),” *Sci. Technol. Built Environ.*, vol. 23, no. 7, pp. 1132–1141, Oct. 2017, doi: 10.1080/23744731.2016.1268904.

[4] P. J. Brooks, “Laboratory study to determine flow resistance of HVAC duct fitting final report for 551-RP,” 1990.

[5] RP-690, “Laboratory Study to Determine Flow Resistance of Oval Ducts and Fittings Final Report,” 1994.

[6] RP-1488, “Laboratory Testing of Flat Oval Fittings to Determine Loss Coefficients. Final Report,” 2011.

[7] Y. Sun, S. E. Ford, and Y. Zhang, “Laboratory testing of flat oval transitions to determine loss coefficients (RP-1606),” *Sci. Technol. Built Environ.*, vol. 21, no. 4, pp. 386–395, May 2015, doi: 10.1080/23744731.2014.998939.

[8] ASHRAE, “Duct Fitting Database Version 6.00.04,” Atlanta, 2015.

[9] C. F. D. S. Contest, “CFD Shootout Contest Prediction of Duct Fitting Losses,”

no. 1, pp. 1–6, 2011.

[10] A. K. Sleiti, J. Zhai, and S. Idem, “Computational fluid dynamics to predict duct fitting losses: Challenges and opportunities,” *HVAC R Res.*, vol. 19, no. 1, pp. 2–9, 2013, doi: 10.1080/10789669.2012.716341.

[11] M. Liu, L. Tan, and S. Cao, “Cavitation-vortex-turbulence interaction and one-dimensional model prediction of pressure for hydrofoil ALE15 by large eddy simulation,” *J. Fluids Eng. Trans. ASME*, vol. 141, no. 2, Feb. 2018, doi: 10.1115/1.4040502.

[12] A. Manning, J. Wilson, N. Hanlon, and T. Mikjaniec, “Prediction of duct fitting losses using computational fluid dynamics,” *HVAC R Res.*, vol. 19, no. 4, pp. 400–411, 2013, doi: 10.1080/10789669.2013.786603.

[13] M. Gutović, H. Lulić, and E. Sirbubalo, “CFD Analysis of pressure losses in flat-oval duct fittings,” in *ASHRAE Transactions*, 2013, vol. 119, no. PART 2, pp. 330–340.

[14] F. Rütten, W. Schröder, and M. Meinke, “Large-eddy simulation of low frequency oscillations of the Dean vortices in turbulent pipe bend flows,” *Phys. Fluids*, vol. 17, no. 3, p. 035107, Mar. 2005, doi: 10.1063/1.1852573.

[15] B. Djebedjian, M. S. Mohamed, and A. Elsayed, “Numerical Studies of Curvature Effect on Turbulent Flows in 180 Curved Ducts,” *Proc. IEC*, pp. 347–370, 2008, [Online]. Available: https://www.researchgate.net/profile/Berge_Djebedjian/publication/236961217_NUMERICAL_STUDIES_OF_CURVATURE_EFFECT_ON_TURBULENT_FLOWS_IN_180_CURVED_DUCTS/links/00b4951a72972cff76000000/NUMERICAL-STUDIES-OF-CURVATURE-EFFECT-ON-TURBULENT-FLOWS-IN-180-CURVED-.

[16] J. Zhang and A. Li, “CFD simulation of particle deposition in a horizontal turbulent duct flow,” *Chem. Eng. Res. Des.*, vol. 86, no. 1 A, pp. 95–106, 2008, doi: 10.1016/j.cherd.2007.10.014.

[17] M. Kumar Gopaliya and D. R. Kaushal, “Modeling of sand-water slurry flow through horizontal pipe using CFD,” *J. Hydrol. Hydromechanics*, vol. 64, no. 3, pp. 261–272, 2016, doi: 10.1515/johh-2016-0027.

[18] A. Soleimani, S. Schneiderbauer, and S. Pirker, “CFD study of the gas-particle flow in a horizontal duct: The impact of the solids wall boundary conditions,” in *Procedia Engineering*, 2015, vol. 102, pp. 1026–1037, doi: 10.1016/j.proeng.2015.01.225.

[19] S. Brehm, T. Kächele, and R. Niehuis, “CFD Investigations on the Influence of varying Inflow Conditions on the Aerodynamics in an S-Shaped Inlet Duct,” Jul. 2014, doi: 10.2514/6.2014-3595.

[20] T. Ghisu, G. T. Parks, J. P. Jarrett, and P. J. Clarkson, “An integrated system for the aerodynamic design of compression systems-part I: Development,” *J. Turbomach.*, vol. 133, no. 1, Jan. 2011, doi: 10.1115/1.4000534.

[21] E. M. Siggeirsson, N. Andersson, and M. Olander Burak, “Off design simulations of an S-shaped intermediate compressor duct: Experimental validation of DDES and RANS using G3D::Flow,” in *AIAA Scitech 2020 Forum*, Jan. 2020, vol. 1 PartF, doi: 10.2514/6.2020-1761.

[22] K. M. Britchford, A. P. Manners, J. J. McGuirk, and S. J. Stevens, “Measurement and prediction of low in annular S-shaped ducts,” *Exp. Therm. Fluid Sci.*, vol. 9, no. 2, pp. 197–205, 1994, doi: 10.1016/0894-1777(94)90112-0.

[23] D. W. Bailey, K. M. Britchford, J. F. Carrotte, and S. J. Stevens, “Performance Assessment of an Annular S-Shaped Duct,” in *Volume 1: Turbomachinery*, Jun.

1995, vol. 1, doi: 10.1115/95-GT-242.

[24] H. Lu, X. Zheng, and Q. Li, “A combinatorial optimization design method applied to S-shaped compressor transition duct design,” *Proc. Inst. Mech. Eng. Part G J. Aerosp. Eng.*, vol. 228, no. 10, pp. 1749–1758, 2014, doi: 10.1177/0954410014531922.

[25] J. Selvanayagam, C. Aliaga, and J. Stokes, “CFD simulation of S-duct test case using ANSYS FLUENT,” 2019, doi: 10.2514/6.2019-3847.

[26] P. K.Sinha, A. K. Biswas, A. N. Mullick, and B. Majumdar, “Flow Development through a Duct and a Diffuser Using CFD,” *Int. J. Eng. Res. Appl.*, vol. 7, no. 01, pp. 46–54, 2017, doi: 10.9790/9622-0701044654.

[27] X. Zhang, X. Sun, R. N. Christensen, M. Anderson, and M. Carlson, “Optimization of S-Shaped Fin Channels in a Printed Circuit Heat Exchanger for Supercritical CO2 Test Loop,” *5th Int. Symp. - Supercrit. CO2 Power Cycles*, pp. 1–15, 2016, [Online]. Available: http://sco2symposium.com/papers2016/HeatExchanger/018paper.pdf.

[28] H. GÖKÇE, U. C. KÜÇÜK, and İ. ŞAHİN, “Effects of Curvature and Area Distribution on S-Shaped Subsonic Diffuser Performance,” *Mechanics*, vol. 24, no. 6, pp. 770–776, Jan. 2019, doi: 10.5755/j01.mech.24.6.22460.

[29] A. Gupta, H. Singh, and A. K. Raghav, “Effect of Change in the Curvature of Flow and Performance Characteristics of Straight and S-shaped Diffuser,” *J. Inst. Eng. Ser. C*, vol. 101, no. 6, pp. 977–989, 2020, doi: 10.1007/s40032-020-00601-7.

[30] E. Immonen, “Shape optimization of annular S-ducts by CFD and high-order polynomial response surfaces,” *Eng. Comput. (Swansea, Wales)*, vol. 35, no. 2, pp. 932–954, 2018, doi: 10.1108/EC-08-2017-0327.

[31] A. D'ambros, T. Kipouros, P. Zachos, M. Savill, and E. Benini, "Computational design optimization for S-Ducts," *Designs*, vol. 2, no. 4, pp. 1–21, 2018, doi: 10.3390/designs2040036.

[32] M. Karbon and A. K. Sleiti, "Turbulence Modeling Using Z-F, RSM, LES and WMLES for Flow Analysis in Z-Shape Ducts," in *Volume 3: Computational Fluid Dynamics; Micro and Nano Fluid Dynamics*, Jul. 2020, pp. FEDSM2020-20001, doi: 10.1115/FEDSM2020-20001.

[33] M. Karbon and A. K. Sleiti, "Turbulence Modeling Using Z-F Model and RSM for Flow Analysis in Z-SHAPE Ducts," *J. Eng.*, vol. 2020, no. 2314–4904, pp. 1–10, Mar. 2020, doi: 10.1155/2020/4854837.

[34] F. R. Menter, "Zonal two equation κ-ω turbulence models for aerodynamic flows," 1993, doi: 10.2514/6.1993-2906.

[35] F. R. Menter, "Two-equation eddy-viscosity turbulence models for engineering applications," *AIAA J.*, vol. 32, no. 8, pp. 1598–1605, Aug. 1994, doi: 10.2514/3.12149.

[36] J. R. Weske, *Experimental Investigation of Velocity Distributions Downstream of single Duct Bends.*, vol. TN No.1471. 1948.

[37] W. N. Al-Rafai, Y. D. Tridimas, and N. H. Woolley, "A Study of Turbulent Flows in Pipe Bends," *Proc. Inst. Mech. Eng. Part C Mech. Eng. Sci.*, vol. 204, no. 6, pp. 399–408, Nov. 1990, doi: 10.1243/PIME_PROC_1990_204_120_02.

[38] A. M. K. P. Taylor, J. H. Whitelaw, and M. Yianneskis, "Curved ducts with strong secondary motion: Velocity measurements of developing laminar and turbulent flow," *J. Fluids Eng. Trans. ASME*, vol. 104, no. 3, pp. 350–359, Sep. 1982, doi: 10.1115/1.3241850.

[39] K. Sudo, M. Sumida, and H. Hibara, "Experimental investigation on turbulent

flow in a circular-sectioned 90-degree bend," *Exp. Fluids*, vol. 25, no. 1, pp. 42–49, Jun. 1998, doi: 10.1007/s003480050206.

[40] K. Sudo, M. Sumida, and H. Hibara, "Experimental investigation on turbulent flow in a square-sectioned 90-degree bend," *Exp. Fluids*, vol. 30, no. 3, pp. 246–252, Mar. 2001, doi: 10.1007/s003480000157.

[41] K. Sudo, M. Sumida, and H. Hibara, "Experimental investigation on turbulent flow through a circular-sectioned 180° bend," *Exp. Fluids*, vol. 28, no. 1, pp. 51–57, Jan. 2001, doi: 10.1007/s003480050007.

[42] A. Ono, N. Kimura, H. Kamide, and A. Tobita, "Influence of elbow curvature on flow structure at elbow outlet under high Reynolds number condition," in *Nuclear Engineering and Design*, Nov. 2011, vol. 241, no. 11, pp. 4409–4419, doi: 10.1016/j.nucengdes.2010.09.026.

[43] L. Tan, B. Zhu, Y. Wang, S. Cao, and K. Liang, "Turbulent flow simulation using large eddy simulation combined with characteristic-based split scheme," *Comput. Fluids*, vol. 94, pp. 161–172, May 2014, doi: 10.1016/j.compfluid.2014.01.037.

[44] M. J. Tunstall and J. K. Harvey, "On the effect of a sharp bend in a fully developed turbulent pipe-flow," *J. Fluid Mech.*, vol. 34, no. 3, pp. 595–608, Dec. 1968, doi: 10.1017/S0022112068002107.

[45] L. H. O. Hellström, M. B. Zlatinov, G. Cao, and A. J. Smits, "Turbulent pipe flow downstream of a bend," *J. Fluid Mech.*, vol. 735, no. R7, p. R7, Nov. 2013, doi: 10.1017/jfm.2013.534.

[46] L. H. O. Hellström, M. B. Zlatinov, A. J. Smits, and G. Cao, "Turbulent pipe flow through a 90° bend," in *7th International Symposium on Turbulence and Shear Flow Phenomena, TSFP 2011*, 2011, vol. 2011-July.

[47] M. TANAKA and H. OHSHIMA, “Numerical Investigation on Large Scale Eddy Structure in Unsteady Pipe Elbow Flow at High Reynolds Number Conditions with Large Eddy Simulation Approach,” *J. Power Energy Syst.*, vol. 6, no. 2, pp. 210–228, 2012, doi: 10.1299/jpes.6.210.

[48] J. Kim, M. Yadav, and S. Kim, “Characteristics of Secondary Flow Induced by 90-Degree Elbow in Turbulent Pipe Flow,” *Eng. Appl. Comput. Fluid Mech.*, vol. 8, no. 2, pp. 229–239, Jan. 2014, doi: 10.1080/19942060.2014.11015509.

[49] R. Röhrig, S. Jakirlić, and C. Tropea, “Comparative computational study of turbulent flow in a 90° pipe elbow,” *Int. J. Heat Fluid Flow*, vol. 55, pp. 120–131, Oct. 2015, doi: 10.1016/j.ijheatfluidflow.2015.07.011.

[50] C. Carlsson, E. Alenius, and L. Fuchs, “Swirl switching in turbulent flow through 90° pipe bends,” *Phys. Fluids*, vol. 27, no. 8, p. 085112, Aug. 2015, doi: 10.1063/1.4928971.

[51] S. Wang, C. Ren, Y. Sun, X. Yang, and J. Tu, “A Study on the Instantaneous Turbulent Flow Field in a 90-Degree Elbow Pipe with Circular Section,” *Sci. Technol. Nucl. Install.*, vol. 2016, no. 5265748, pp. 1–8, 2016, doi: 10.1155/2016/5265748.

[52] P. Dutta, S. K. Saha, N. Nandi, and N. Pal, “Numerical study on flow separation in 90° pipe bend under high Reynolds number by k-ε modelling,” *Eng. Sci. Technol. an Int. J.*, vol. 19, no. 2, pp. 904–910, Jun. 2016, doi: 10.1016/j.jestch.2015.12.005.

[53] A. Baramili, L. Chatellier, L. David, and L. Ancian, “Prediction of Elbow Flow Dynamics Using Correlated Wall Pressure Data,” in *Volume 4: Fluid-Structure Interaction*, Jul. 2018, vol. 4, doi: 10.1115/PVP2018-84712.

[54] Z. Wang, R. Örlü, P. Schlatter, and Y. M. Chung, “Direct numerical simulation

of a turbulent 90° bend pipe flow," *Int. J. Heat Fluid Flow*, vol. 73, no. 73, pp. 199–208, Oct. 2018, doi: 10.1016/j.ijheatfluidflow.2018.08.003.

[55] M. A. Tanaka, H. Ohshima, and H. Monji, "Numerical investigation of flow structure in pipe elbow with large Eddy simulation approach," in *American Society of Mechanical Engineers, Pressure Vessels and Piping Division (Publication) PVP*, Jan. 2010, vol. 3, pp. 449–458, doi: 10.1115/PVP2009-77598.

[56] Y. Liu and L. Tan, "Spatial–Temporal Evolution of Tip Leakage Vortex in a Mixed-Flow Pump With Tip Clearance," *J. Fluids Eng.*, vol. 141, no. 8, Aug. 2019, doi: 10.1115/1.4042756.

[57] N. Saito, "Large-Eddy Simulations of Fully Developed Turbulent Channel and Pipe Flows with Smooth and Rough Walls," California Institute of Technology, 2014.

[58] "IV. On the dynamical theory of incompressible viscous fluids and the determination of the criterion," *Philos. Trans. R. Soc. London.*, vol. 186, no. A, pp. 123–164, Dec. 1895, doi: 10.1098/rsta.1895.0004.

[59] J. Boussinesq, "Théorie de l'écoulement tourbillant," 1877.

[60] L. Prandtl, "7. Bericht über Untersuchungen zur ausgebildeten Turbulenz," *ZAMM - J. Appl. Math. Mech. / Zeitschrift für Angew. Math. und Mech.*, vol. 5, no. 2, pp. 136–139, 1925, doi: 10.1002/zamm.19250050212.

[61] J. SMAGORINSKY, "GENERAL CIRCULATION EXPERIMENTS WITH THE PRIMITIVE EQUATIONS," *Mon. Weather Rev.*, vol. 91, no. 3, pp. 99–164, Mar. 1963, doi: 10.1175/1520-0493(1963)091<0099:gcewtp>2.3.co;2.

[62] K. Hanjalić, M. Popovac, and M. Hadžiabdić, "A robust near-wall elliptic-relaxation eddy-viscosity turbulence model for CFD," *Int. J. Heat Fluid Flow*,

vol. 25, no. 6, pp. 1047–1051, Dec. 2004, doi: 10.1016/j.ijheatfluidflow.2004.07.005.

[63] M. Popovac and K. Hanjalic, “Compound wall treatment for RANS computation of complex turbulent flows and heat transfer,” *Flow, Turbul. Combust.*, vol. 78, no. 2, pp. 177–202, Feb. 2007, doi: 10.1007/s10494-006-9067-x.

[64] P. A. Durbin, “Separated flow computations with the k-ε-v2 model,” *AIAA J.*, vol. 33, no. 4, pp. 659–664, Apr. 1995, doi: 10.2514/3.12628.

[65] M. Karbon and A. K. Sleiti, “Large Eddy Simulation for Prediction of Flow in Close-Coupled Elbows,” *ICTEA Int. Conf. Therm. Eng.*, vol. 2018, no. 2018, 2018.

[66] J. W. Deardorff, “A numerical study of three-dimensional turbulent channel flow at large Reynolds numbers,” *J. Fluid Mech.*, vol. 41, no. 2, pp. 453–480, Apr. 1970, doi: 10.1017/S0022112070000691.

[67] P. Moin and J. Kim, “Numerical investigation of turbulent channel flow,” *J. Fluid Mech.*, vol. 118, no. 1, p. 341, May 1982, doi: 10.1017/S0022112082001116.

[68] W. P. Jones and M. Wille, “Large-eddy simulation of a plane jet in a cross-flow,” *Int. J. Heat Fluid Flow*, vol. 17, no. 3, pp. 296–306, Jun. 1996, doi: 10.1016/0142-727X(96)00045-8.

[69] M. Germano, U. Piomelli, P. Moin, and W. H. Cabot, “A dynamic subgrid-scale eddy viscosity model,” *Phys. Fluids A Fluid Dyn.*, vol. 3, no. 7, pp. 1760–1765, Jul. 1991, doi: 10.1063/1.857955.

[70] D. K. Lilly, “A proposed modification of the Germano subgrid-scale closure method,” *Phys. Fluids A*, vol. 4, no. 3, pp. 633–635, 1992, doi: 10.1063/1.858280.

[71] F. Nicoud and F. Ducros, “Subgrid-scale stress modelling based on the square of the velocity gradient tensor,” *Flow, Turbul. Combust.*, vol. 62, no. 3, pp. 183–200, 1999, doi: 10.1023/A:1009995426001.

[72] J. SMAGORINSKY, “GENERAL CIRCULATION EXPERIMENTS WITH THE PRIMITIVE EQUATIONS,” *Mon. Weather Rev.*, vol. 91, no. 3, pp. 99–164, Mar. 1963, doi: 10.1175/1520-0493(1963)091<0099:gcewtp>2.3.co;2.

[73] S. B. Pope, “Direct numerical simulation,” in *Turbulent Flows*, Cambridge University Press, 2012, pp. 344–357.

[74] P. Y. Chou, “On velocity correlations and the solutions of the equations of turbulent fluctuation,” *Q. Appl. Math.*, vol. 3, no. 1, pp. 38–54, Apr. 1945, doi: 10.1090/qam/11999.

[75] C. Münch and O. Métais, “Large eddy simulations in curved square ducts: variation of the curvature radius,” *J. Turbul.*, vol. 8, no. 1–18, p. N28, Jan. 2007, doi: 10.1080/14685240601142859.

[76] P. Rudolf and M. Desová, “Flow characteristics of curved ducts,” *Appl. Comput. Mech.*, vol. 1, no. 265, pp. 255–265, 2007.

[77] A. K. SLEITI and J. S. KAPAT, “Comparison between EVM and RSM turbulence models in predicting flow and heat transfer in rib-roughened channels,” *J. Turbul.*, vol. 7, no. 1–21, p. N29, Jan. 2006, doi: 10.1080/14685240500499343.

[78] A. K. Sleiti and J. S. Kapat, “Heat Transfer in Channels in Parallel-Mode Rotation at High Rotation Numbers,” *J. Thermophys. Heat Transf.*, vol. 20, no. 4, pp. 748–753, Oct. 2006, doi: 10.2514/1.16634.

[79] A. K. Sleiti and J. S. Kapat, “Fluid flow and heat transfer in rotating curved duct at high rotation and density ratios,” *J. Turbomach.*, vol. 127, no. 4, pp. 659–667,

2005, doi: 10.1115/1.2019276.

[80] A. K. Sleiti and J. S. Kapat, “Effect of Coriolis and centrifugal forces on turbulence and transport at high rotation and density ratios in a rib-roughened channel,” *Int. J. Therm. Sci.*, vol. 47, no. 5, pp. 609–619, May 2008, doi: 10.1016/j.ijthermalsci.2007.06.008.

[81] A. K. Sleiti and J. S. Kapat, “Effect of Coriolis and Centrifugal Forces at High Rotation and Density Ratios,” *J. Thermophys. Heat Transf.*, vol. 20, no. 1, pp. 67–79, Jan. 2006, doi: 10.2514/1.14847.

[82] I. B. Kazatchkov and S. G. Hatzikiriakos, “Relaxation effects of slip in shear flow of linear molten polymers,” *Rheol. Acta*, vol. 49, no. 3, pp. 267–274, Mar. 2010, doi: 10.1007/s00397-009-0416-2.

[83] H. J. Bae, A. Lozano-Durán, S. T. Bose, and P. Moin, “Turbulence intensities in large-eddy simulation of wall-bounded flows,” *Phys. Rev. Fluids*, vol. 3, no. 1, p. 014610, Jan. 2018, doi: 10.1103/PhysRevFluids.3.014610.

[84] A. K. Sleiti, “Effect Of Coriolis And Centrifugal Forces On Turbulence And Transport At High Rotation And Buoyancy Numbers Transport At High Rotation And Buoyancy Numbers,” University of Central Florida, 2004.

[85] T. Cebeci and P. Bradshaw, “Momentum transfer in boundary layers.,” p. 407, 1977.

[86] ANSYS CFX-Solver Theory Guide, “ANSYS Fluent Theory Guide.” [Online]. Available: file:///C:/Users/q123_/AppData/Local/Temp/113AnsysCFXSolverTheoryGuide.pdf.

[87] T. T. Chandratilleke and Nursubyakto, “Numerical prediction of secondary flow and convective heat transfer in externally heated curved rectangular ducts,” *Int.*

J. Therm. Sci., vol. 42, no. 2, pp. 187–198, Feb. 2003, doi: 10.1016/S1290-0729(02)00018-2.

[88] "Verhandlungen des 2. Internationalen Kongresses für Technische Mechanik, Zürich 12. bis 17. September 1926. Im Auftrag des Organisationskomitees herausgegeben von Dr. Ernst Meissner, Professor an der Eidgenössischen Technischen Hochschule in Zürich. Verla," *ZAMM - Zeitschrift für Angew. Math. und Mech.*, vol. 8, no. 6, pp. 493–494, 1928, doi: 10.1002/zamm.19280080608.

[89] M. Karbon and A. K. Sleiti, "Large-eddy simulation of the flow in Z-Shape duct," *Cogent Eng.*, vol. 7, no. 1, Jan. 2020, doi: 10.1080/23311916.2020.1778349.

[90] J. Pallares and L. Davidson, "Large-eddy simulations of turbulent heat transfer in stationary and rotating square ducts," *Phys. Fluids*, vol. 14, no. 8, pp. 2804–2816, Aug. 2002, doi: 10.1063/1.1489684.

[91] A. K. Sleiti and J. S. Kapat, "Fluid Flow and Heat Transfer in Rotating Curved Duct at High Rotation and Density Ratios," in *Volume 3: Turbo Expo 2004*, Jan. 2004, vol. 127, no. 4, pp. 33–43, doi: 10.1115/GT2004-53028.

[92] Y. D. Lee, G. H., Choi, "Study on the analysis of turbulent flow in a rotating square sectioned 90° curved duct," *Trans. Korean Soc. Mech. Eng.*, vol. 19, no. 9, 1995.

[93] J. Luo and B. Lakshminarayana, "Prediction of strongly curved turbulent duct flows with Reynolds stress model," *AIAA J.*, vol. 35, pp. 91–98, Jan. 1997, doi: 10.2514/3.13468.

[94] Y. Hu and C. Li, "Numerical Simulation on the Gas-Phase Flow Field in 90° Curved Duct with Different Inclination Angle," in *2009 International*

Conference on Computational Intelligence and Software Engineering, Dec. 2009, pp. 1–5, doi: 10.1109/CISE.2009.5362616.

[95] M. Breuer and W. Rodi, "Large Eddy Simulation for Complex Turbulent Flows of Practical Interest," 1996, pp. 258–274.

[96] K. Ramadani, M. E. Kelterer, R. Pecnik, and W. Sanz, "Application of the zeta-F-turbulence model to steady transitional flow," 2009.

[97] C. Carton de Wiart, J. Larsson, and S. M. Murman, "Validation of WMLES on a periodic channel flow featuring adverse/favorable pressure gradients," 2018.

[98] ANSYS, "ANSYS Fluent Theory Guide," *ANSYS Inc., USA*. p. 814, 2013, [Online]. Available: http://www.afs.enea.it/project/neptunius/docs/fluent/html/th/main_pre.htm.

[99] P. A. Durbin, "Near-wall turbulence closure modeling without 'damping functions,'" *Theor. Comput. Fluid Dyn.*, vol. 3, no. 1, pp. 1–13, 1991, doi: 10.1007/BF00271513.

[100] Ansys Inc, "ANSYS Fluent UDF Manual," *Knowl. Creat. Diffus. Util.*, 2013.

[101] CFD Online, "Favre averaged Navier-Stokes equations -- CFD-Wiki, the free CFD reference," *www.cfd-online.com*, 2005. .

APPENDIX A: LIST OF PUBLICATIONS

A.1 Journals

1. M. Karbon and A. K. Sleiti, “Turbulence Modeling Using Z-F Model and RSM for Flow Analysis in Z-SHAPE Ducts,” *J. Eng. Hindawi (United Kingdom)*, Mar, 2020. vol. 2020, 2020, doi: 10.1155/2020/4854837.

2. Mohammed Karbon & Ahmad K. Sleiti | Duc Pham (Reviewing editor) (2020) Large-eddy simulation of the flow in Z-Shape duct, Cogent Engineering, 7:1, DOI: 10.1080/23311916.2020.1778349

A.2 Conferences

1. M. Karbon and A. K. Sleiti, “Turbulence modeling using Z-F, RSM, LES and WMLES for flow analysis in Z-Shape ducts,” July, 2020, Volume 3: Computational Fluid Dynamics; Micro and Nano Fluid Dynamics, ASME Fluids Engineering Division Summer Meeting, doi: 10.1115/FEDSM2020-20001.

2. M. Karbon, A. K. Sleiti, "Large Eddy Simulation for Prediction of Flow in Close-Coupled Elbows," 11th International Conference on Thermal Engineering: Theory and Applications, Vol 2018 (2018): ICTEA 2018, Mar 2018.
https://journals.library.ryerson.ca/index.php/ictea/article/view/246/138

APPENDIX B: USER DEFINED FUNCTION CODE

```
#include "udf.h"
#include "math.h"

/* Turbulence model constants */
 // the constants of the zeta-f model and its respective values are declared
const real C_MU=0.22;
const real C_T=6.0;
const real C_ETA=85.0;
const real C_L=0.36;
const real SIG_K=1.0;
const real SIG_E=1.3;
const real SIG_ZETA=1.2;
const real CE_2=1.9;
const real C_1=1.4;
const real C_2=0.65;
const real N_zeta=2.0;
const real y_star_limit=30.0;
const real C_MU_ke=0.09;

/* C_R(C,t)=rho*/
// It is not required to declare a value (rho) to the predefined macro C_R(c,t), because it already returns the fluid density value. But it is possible to do the opposite (e.g declare real rho(c,t) = C_R(c,t)). It is possible to use in the code the terminology "rho(c,t)"
```

instead of "C_R(c,t)".

/* User-defined scalars */

enum

// enum is used to replace the index i of the C_UDSI(c,t,i) macro (which in this UDF defines the turbulence scalars K, E, ZETA and F), in which i = (0,1,2,3,...). By using enum, the scalars numbers are replaced by the listed letters. Using it, the listed letters are used instead of numbers, making the code cleaner and easier to understand it. Also, it does not change anything on the ANSYS Fluent graphical interface.

{

K,

E,

ZETA,

F,

N_REQUIRED_UDS

};

DEFINE_SOURCE(k_source, c, t, dS, eqn)

// DEFINE_SOURCE is a predefined macro to create a source term. In this case is the K equation source term, but we need to correctly select it to K in the graphical user interface.

{

real source;

// declaration of the variable "source" as a real. It is not necessary since the

DEFINE_SOURCE macro already returns a real value.

```
        //dS[eqn]=-2*
pow(C_R(c,t),2)*C_UDSI(c,t,K)*C_MU*C_UDSI(c,t,ZETA)/C_UDMI(c,t,0);
        //source=C_UDMI(c,t,3)                                    -
pow(C_R(c,t),2)*pow(C_UDSI(c,t,K),2)*C_MU*C_UDSI(c,t,ZETA)/C_UDMI(c,t,0)
;
 //
        dS[eqn]= -C_R(c,t)/C_UDMI(c,t,1);
```

// In this part we can set the source term derivative in respect to K (dS/dK). The production term depends on the turbulent viscosity which in turn depends on K. Thus, the derivative dS/dK does not consider the appearance of K in the production term, as it is set to 0. Also, the appearance of K will vary from point to point in the flow, once the Time scale T, defined as "C_UDMI(c,t,3)", has a MIN and MAX definition, making it sometimes independent and dependent on K. So, in such cases it is preferred to leave it a 0 value in the derivative and ANSYS Fluent handle it explicit.

```
        source=C_UDMI(c,t,3) - C_R(c,t)*C_UDSI(c,t,K)/C_UDMI(c,t,1);
```

// The source term of the K equation is defined by the variable source.

```
        return source;
```

// The "source" variable is returned as the value of the DEFINED_SOURCE macro. Now ANSYS Fluent will understand it as the source term of the K equation.

```
}
```

```
DEFINE_SOURCE(e_source, c, t, dS, eqn)
// The above approach is repeated
{
        real source;
 // The source variable is again declared as a real value. It can have the "source" name again because it is declared locally (inside the macro).
        real CE_1;

  // The model "constant" CE_1 is declared inside the macro as a real value. Means it can only be called inside the macro. If it is used in another macro, Fluent will return an error. On the other hand, the constants values declared in lines 4-20 are declared globally and can be used by any macro presented in the code.

        CE_1=1.4 * ( 1.0+0.012/C_UDSI(c,t,ZETA) );

// The CE_1 value is evaluated.

        dS[eqn]= -CE_2*C_R(c,t)/C_UDMI(c,t,1);
        source=  (  CE_1*C_UDMI(c,t,3) - CE_2*C_R(c,t)*C_UDSI(c,t,E) )/C_UDMI(c,t,1);

 // The source variable is defined
        return source;

  // The source variable value is returned as the value of the DEFINE_SOURCE macro.
```

```
}

DEFINE_SOURCE(zeta_source, c, t, dS, eqn)

  // Same above procedures apply here.

{
        real source;
        //real f;
        //kf=C_UDSI(c,t,K)*C_UDSI(c,t,F);

        dS[eqn]=-(              C_UDMI(c,t,3)-(1-N_zeta)*C_R(c,t)*C_UDSI(c,t,E)
)/C_UDSI(c,t,K);
        source=C_R(c,t)*C_UDSI(c,t,F)  -  C_UDSI(c,t,ZETA)/C_UDSI(c,t,K)  *  (
C_UDMI(c,t,3)-(1-N_zeta)*C_R(c,t)*C_UDSI(c,t,E) );
        return source;
}

DEFINE_SOURCE(f_source, c, t, dS, eqn)
      // // Same above procedures apply here.
{
        real source, f_h;

        f_h=(       (   C_1-1.0+C_2*C_UDMI(c,t,3)/(C_R(c,t)*C_UDSI(c,t,E))   )*(
C_UDSI(c,t,ZETA)-2.0/3.0 ) + C_UDSI(c,t,ZETA)*(N_zeta-1.0)  )/C_UDMI(c,t,1);
```

```
        dS[eqn]=-1.0/SQR(C_UDMI(c,t,2));
        source=-( C_UDSI(c,t,F) + f_h )/SQR( C_UDMI(c,t,2) );
        return source;
}

DEFINE_DIFFUSIVITY(ke_zeta_f_diffusivity, c, t, eqn)

 // The predefined macro used to compute the diffusive term of the four turbulence
equations. it only needs to return the diffusion coefficient, cause the Laplacian operator
of each equation is implicit defined by the ANSYS Fluent solver.
{
        real diff;

  // The declaration of the diff variable as a real value. Each diffusion coefficient will
be stored in diff, and then it will be returned as the macro value.

        switch (eqn)
 // The switch statement is used to define all diffusion coefficient of all turbulence
equations inside just one DEFINE_DIFFUSIVITY macro. Otherwise we will need to
create four define diffusivity macros, as was done for the source terms. However, this
approach cannot be applied to source terms.
        {
                case K:

        // In case you select the equation in which we will define the value of "diff" using
```

the declared values in "enum".

```
diff=C_UDMI(c,t,0)/SIG_K+C_MU_L(c,t);
```

// The diff returns the diffusion coefficient of the K equation (Equation 5)

```
break;
```

// A break is used to call another case, for the other 3 equations.

```
case E:
diff=C_UDMI(c,t,0)/SIG_E+C_MU_L(c,t);
break;

case ZETA:
diff=C_UDMI(c,t,0)/SIG_ZETA+C_MU_L(c,t);
break;

case F:
diff=1.0;
```

// In equation 8 the diffusion coefficient is the squared length scale (L^2), but in the UDF we divided the entire equation by (L^2), and it becomes 1.

```
break;
default:
diff=0.0;
```

// The default statement is not necessary. But it if the problem has more transport

equations (which it does not), its diffusion coefficient will be set to 0.

```
        }
        return diff;
  // Here the value of each diffusion coefficient is returned.
}

DEFINE_UDS_FLUX(user_flux, f, t, eqn)
  // The convective term predefined macro (DEFINE_UDS_FLUX) is used to compute the convective term. This macro only returns the flux term, which is the mass flux (density*velocity though the cell faces).
{
         switch (eqn)
    // The switch statement is also used
        {
                case K:
                return F_FLUX(f,t);

  // The F_FLUX(f,t) macro automatically returns the mass flux.
                break;

                case E:
                return F_FLUX(f,t);
                break;
                case ZETA:
```

```
                return F_FLUX(f,t);
                break;

                case F:
                return 0.0;

  // The F equation do not have a convective term, so the flux must be set to be zero to cancel the term out.
                break;

                default:
                return 0.0;
        //
          }
}

DEFINE_ADJUST(ke_adjust,domain)
  // The adjust function is called by the solver at the beginning of each iteration (or time step) and it is used here to store flow variables values in the solver memory (which can be accessed in the post processing) and to relate flow variables.
{
        Thread *t;

  // The thread is a mesh terminology used here to allow access to domain boundaries and to cell zones. It is declared inside the macro because it was not passed as an
```

argument, as it was for all above DEFINE macros.

cell_t c;

// cell_t is used to access the cell centroids. It is also declared here just because it was not passed as an argument in the DEFINE_ADJUST macro.

real y_star, L, T, L01, T01, L_KOL, T_KOL, SR, L_relz, T_relz;

// Flow variables which will be used here are declared as real values.

real mu_t;

/* Set the turbulent viscosity */

thread_loop_c(t,domain)

// Macro to loop the following operations in each domain cells

if (FLUID_THREAD_P(t))

// Statement is used to guarantee the following loop will be only in fluid zones, excluding solid zones, if they exist.

{

begin_c_loop(c,t)

// The loop will be done over cell centroids. All following operations will take place in all domain cells.

{

L_KOL=C_ETA*pow(pow(C_MU_L(c,t)/C_R(c,t),3.0)/C_UDSI(c,t,E) , 0.25);

// The values of the predeclared flow variables are evaluated

```
                                T_KOL=C_T*sqrt(
C_MU_L(c,t)/(C_R(c,t)*C_UDSI(c,t,E)));

                                L_relz=sqrt(C_UDSI(c,t,K))/(
sqrt(6.0)*C_MU*SR*C_UDSI(c,t,ZETA) );
                                T_relz=0.60/( sqrt(6.0)*C_MU*SR*C_UDSI(c,t,ZETA)
);

                                //L01=MIN(  pow(C_UDSI(c,t,K),1.50)/C_UDSI(c,t,E) ,
L_relz );
                                //T01=MIN(  C_UDSI(c,t,K)/C_UDSI(c,t,E) , T_relz );
                            L01=pow(C_UDSI(c,t,K),1.50)/C_UDSI(c,t,E);
                                T01=C_UDSI(c,t,K)/C_UDSI(c,t,E);

                                L=C_L*MAX(L01 , L_KOL);

  // The previous evaluated values are used to compute Length and Time scales
(Equations 14 and 15) in all domain cells.
                                T=MAX(T01 , T_KOL);


mu_t=C_R(c,t)*C_MU*C_UDSI(c,t,ZETA)*C_UDSI(c,t,K)*T;
   // The turbulent viscosity is computed (Equation 13)
                                SR=Strainrate_Mag(c,t);
```

// The ANSYS Fluent macro to compute the strain rate magnitude (Strainrate_Mag(c,t)) is allocated in SR. Now SR returns the flow strain rate mag.

C_K(c,t)=C_UDSI(c,t,K);

// C_K(c,t) and C_D(c,t) are predefined macros which return the value of the turbulent kinetic energy and dissipation rate, respectively. By the UDF implementation in the graphical interface, these values are not used since we are deactivating the turbulence equations. Only relating the user defined values of K and E with the Fluent defined values. This procedure will only affect the post-processing and it is not necessary.

C_D(c,t)=C_UDSI(c,t,E);

C_UDMI(c,t,0)=mu_t;

// The previously defined turbulent viscosity is stored in the memory. C_UDMI is a predefined macro used to store flow variables and made them available at the post-processing. The stored variables can also be used in the code.

C_UDMI(c,t,1)=T;

// The time scale (Equation 14) is also stored.

C_UDMI(c,t,2)=L;

// Equation 15 too.

C_UDMI(c,t,3)=mu_t*SQR(SR);

// Lastly the turbulence production. These 4 stored flow variables can be found in the Fluent post processing under the User Defined memory tab.

```
                }
                end_c_loop(c,t)
        }
}

DEFINE_TURBULENT_VISCOSITY(user_mu_t,c,t)
// In this line the turbulent viscosity value, calculated and stored inside the ADJUST
macro is returned in the DEFINE_TURBULENT_VISCOSITY macro. In the solver, it
will be summed to the molecular viscosity in the momentum equations, defining its
diffusion coefficient.
{
        return C_UDMI(c,t,0);
}

DEFINE_ON_DEMAND(rename_UDvars)
    // The DEFINE_ON_DEMAND macro is used to change the scalars and memory
names in the Fluent graphical interface. It does not affect the solution. According to
the following command lines, at the interface, instead of seeing, for example, 'User
Scalar 0' or 'User Memory 2', now we can see 'k' and 'Turbulent length scale',
respectively.
{
        Set_User_Scalar_Name(0,"UDS0: k");
        Set_User_Scalar_Name(1,"UDS1: e");
        Set_User_Scalar_Name(2,"UDS2: ZETA");
```

```
        Set_User_Scalar_Name(3,"UDS3: f");
        Set_User_Memory_Name(0,"UDM0: Turbulent viscosity");
        Set_User_Memory_Name(1,"UDM1: Turbulent time scale");
        Set_User_Memory_Name(2,"UDM2: Turbulent length scale");
        Set_User_Memory_Name(3,"UDM3: mu_t*StrainRate");
}

DEFINE_PROFILE(e_bc, t, position)
    // This is the most complex part of the UDF, in which a DEFINE_PROFILE macro is used to specify a Neumann boundary condition as a function of the square distance from the wall (If the boundary condition is independent from flow variables, it can be defined via the graphical interface, as it is done for K and ZETA).
{
        real dy;
  // dy is declared as real. dy is the distance from the wall to the first cell centroid next to it. It will be calculated inside the loop for every cell next to a wall.

        face_t f;
  // face_t is used, as it is necessary to access face values and was not passed as an argument.
        cell_t c0;
  // cell_t too.
        Thread *t0=t->t0;

        real xw[ND_ND], xc[ND_ND], dx[ND_ND];
```

// The variables xw, xc and dx are declared as matrix by the macro [ND_ND]. They represent the wall coordinates; the cell coordinates next to the wall and the distance between them (dy = |(xw - xc)|).

```
begin_f_loop(f,t)
```

// A face loop is used to do operations in every face of the wall boundary.

```
{
        c0=F_C0(f,t);
```

// The cells that are next to wall are identified using the F_C0 macro and stored in c0. Basically, F_C0 macro identifies all cell centroids next to the select wall boundary. The wall boundary in which the DEFINE_PROFILE will be used is selected in the Fluent graphical interface.

```
        F_CENTROID(xw,f,t);
```

// The F_CENTROID macro stores the faces centroid coordinates (at the walls) in the xw matrix.

```
        C_CENTROID(xc,c0,t0);
```

// The C_CENTROID macro stores the cell centroids coordinates of the cells next to the wall in matrix xc.

```
        NV_VV(dx, =, xc, -, xw);
```

// The distance between the centroids of the cells next to the wall and the face centroids at the wall is calculated using the NV_VV macro and in the dx matrix. NV_VV macro do the operation dy = xw - xc.

```
dy=ND_MAG(dx[0], dx[1], dx[2]);
```

// The magnitude of dx, which is a matrix, is evaluated and stored in the dy variable. The values [0], [1] and [2] represent the directions x, y and z in the computational domain, respectively.

```
F_PROFILE(f,t,position)=2.*C_MU_L(c0,t0)/C_R(c0,t0)*C_UDSI(c0,t0,K)/SQR(dy
);
```

// Now the dy variable (which is the magnitude of the distance from the wall to the first cell next to it) can be used to evaluate the dissipation rate wall boundary condition (Equation 17).

```
        }
        end_f_loop(f,t)
}
DEFINE_PROFILE(f_bc, t, position)
```

// Same approach used in the dissipation rate boundary condition is used here for the f boundary condition (Equation 17).

```
{
        real dy;
```

```
        face_t f;
        cell_t c0;
        Thread *t0=t->t0;
        real xw[ND_ND], xc[ND_ND], dx[ND_ND];

        begin_f_loop(f,t)
        {
                c0=F_C0(f,t);
                F_CENTROID(xw,f,t);
                C_CENTROID(xc,c0,t0);
                NV_VV(dx, =, xc, -, xw);
                dy=ND_MAG(dx[0], dx[1], dx[2]);

        F_PROFILE(f,t,position)=-
2.*C_MU_L(c0,t0)/C_R(c0,t0)*C_UDSI(c0,t0,ZETA)/SQR(dy);
        }
        end_f_loop(f,t)
} [100], [101]
```

APPENDIX C: SUPPLEMENTAL MATERIAL - PRESSURE LOSS AS A FUNCTION OF SEPARATION DISTANCE

Table 11. Pressure Loss as a Function of Separation Distance

L/D	Mean SP at inlet	Mean SP at outlet	Mean DP at inlet	Mean DP at outlet	Mean TP at inlet	Mean TP at outlet	DP ST	DP TP
2	20.79	0.14	103.48	104.60	124.26	104.74	20.65	19.53
6	72.88	0.01	103.48	104.38	176.36	104.38	72.88	71.98
10	98.18	0.01	103.48	104.51	201.66	104.52	98.17	97.13

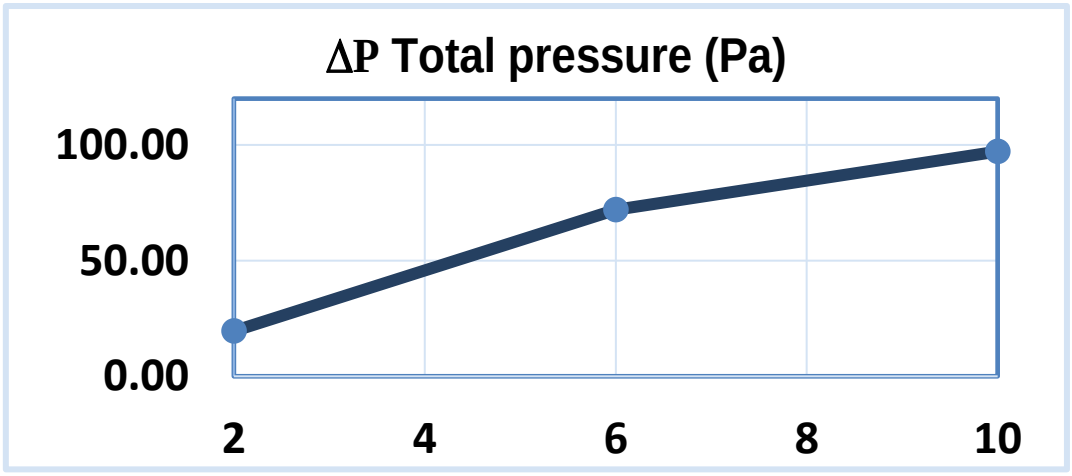

Figure 51. Differential mean total pressure (Pa)

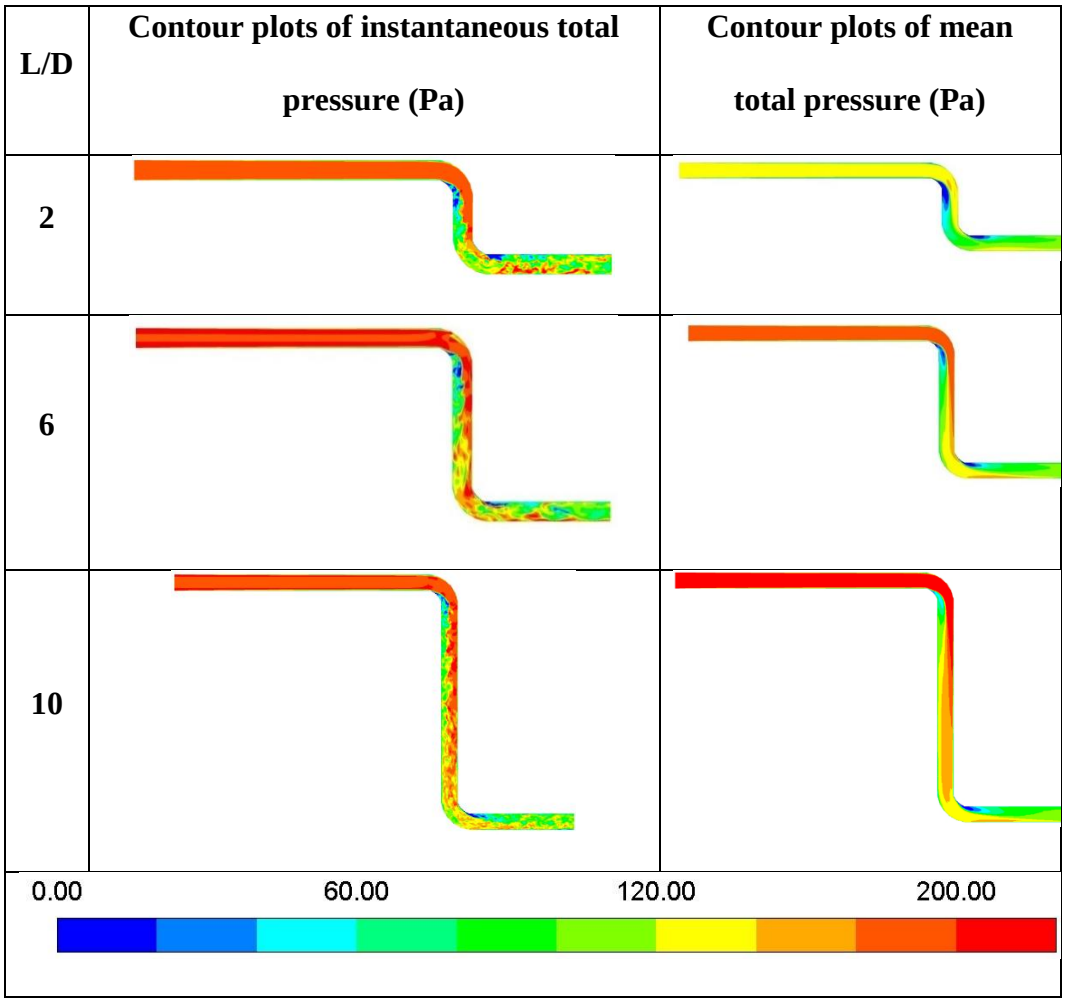

Figure 52. Contour plots of instantaneous total pressure and mean total pressure (Pa)